3.2 Preparation of copper nanowires using ion track membranes

H. Koshikawa, Y. Maekawa, M. Asano and M. Yoshida.
Department of Material Development, JAERI.

Introduction

When polymeric membranes are irradiated by heavy ion beams, each single heavy ion particle induces nanoscopic damage along the ion-path through the materials. The damaged region is susceptible to a proper etchant, resulting in the formation of through-holes with nanoscopic diameters, which are called "ion track membrane". The ion track membranes of high performance (thermally and mechanically stable) polymers can be applied to nanoscopic electronic device such as conductive films, field emitters, and magnetic field sensors through hybridization with conducting metals and semiconducting alloys by electroplating. In this paper, we report the fabrication of conductive and insulating hybrid membranes which consisted of copper wires with diameters ranging from 0.26 to 2.2 μm in polyethyleneterephthalate (PET) film. The geometry of copper nanowires was confirmed with scanning electron microscope (SEM).

Experiment

Commercial PET (thickness 10, 38 μm) was irradiated by $^{129}Xe^{23+}$ (450 MeV) ion with a fluence of $3x10^{5-8}$ ions/cm^2. The PET ion track membranes with cylindrical pores were prepared by etching at 60 °C in 0.2 or 1.0 M NaOH aqueous solution (Fig. 1-a). The ion track membranes were coated with gold (50 nm) using a Giko IB-3 ion coater, followed by electroplating of coppor layer (20 μm) as an electrode[1,2]. Copper nanowires were prepared on the copper layer through the pores of ion track membranes by electrodeposition with periodic potential modulation (-0.2V; 6sec, 0.2V; 1sec) for 2 hours in pH1 solution of 1.3 M $CuSO_4$ (Fig. 1-b). The PET of the obtained hybrid menbranes were dissolved in 10 M-KOH/ethanol (3:7 w/w) mixed solution at 70 °C for 30 min (Fig. 1-c); then, the geometry of copper nanowires were estimated with SEM (JSM-5600, JEOL).

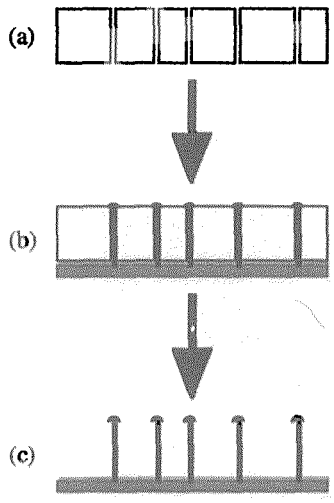

Fig. 1 The fabrication of conductive and insulating hybrid membranes consisted of copper wires in PET ion track membranes.

Results and discussion

Fig. 2-a shows the SEM image of the surface of the PET ion track membrane (thickness: 36 μm) which was obtained by etching at 60 °C in 1.0 M NaOH; then, the pore diameter is estimated to be 2.2 μm by SEM image. Copper wires were deposited into the pores of the PET membranes by

electroplating at 24 °C in 1.3 M $CuSO_4$ solution for 3 hours. Only the PET film was finally removed in a KOH / ethanol mixed solution. In Fig. 2-b, we can observe copper nanowires with 2.2 μm in diameter and 36 μm in hight, confirming that copper wires grew upon the copper electrode through the pores of the PET membrane as a template. Judging from the cross-sectional image of the ion track membrane, the surface roughness on the cylindrical copper wires should result from the roughness of the side wall of the pores of the membranes.

Next, the PET ion track membrane with much narrow pores was used for making copper nanowires by electroplating. As shown in Fig. 3-a, the PET membrane with 260 nm in diameter and 10 mm in thickness was prepared by etching in 0.2 M NaOH. Using this membrane, copper nanowires of 260 nm in diameter and 6.3 mm in hight were prepared by electroplating in 1.3 M $CuSO_4$ for 1 hour. After removing the PET film from copper electrode in the KOH/ethanol solution, the geometry of the copper nanowires was found to be 260 nm in diameter and 6.3 mm in hight by SEM, as shown in Fig. 3-b. Currently, we are studying conductive characteristics of PET/copper hybrid menbranes.

References

1 T. Molares, V. Buschmann, D. Dobrev, R. Neumann, R. Scholz, I. U. Schuchert, J. Vetter, Adv. Matter., 13(2001) 62.

2 D. Dobrev, J. Vetter, N. Angert, Nuclear Instruments and Methods in Physics Research B 149 (1999) 207-212.

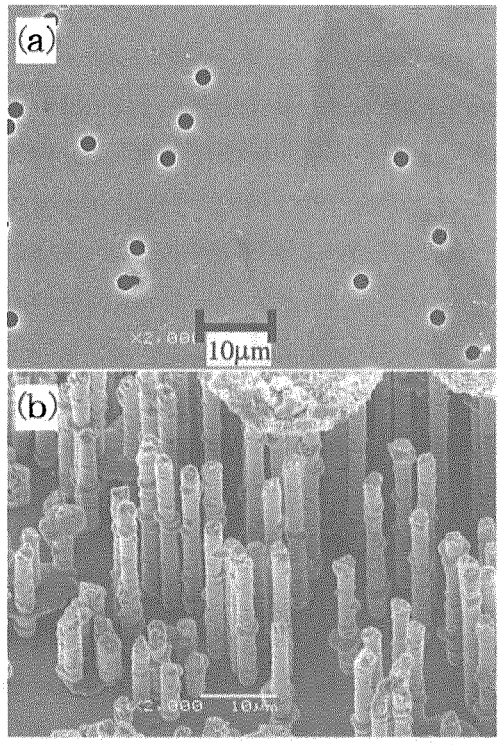

Fig. 2 (a) The PET ion track membrane; 2.2 mm in diameter. (b) The copper nanowires; 2.2 mm in diameter, 36 mm in height .

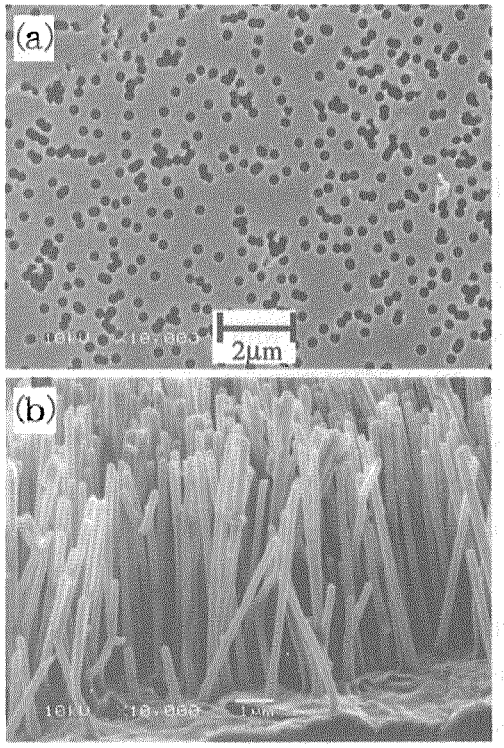

Fig. 3 (a) The PET ion track membrane; 2.2 mm in diameter. (b) The copper nanowires; 260 nm in diameter, 6.3 mm in height.

3.3 Nano-wire Formation and Selective Adhesion on Substrates by Single Track Gelation of Polysilanes

Shu Seki*, Satoshi Tsukuda*, Yoichi Yoshida*, Seiichi Tagawa*, Masaki Sugimoto**, Norio Morishita**, and Shigeru Tanaka**

The Institute of Scientific and Industrial Research, Osaka University, Department of Material Development, JAERI***

Abstract

High density energy deposition by ion beams causes non-homogeneous crosslinking reaction of polysilane derivatives within a nano-sized cylindrical area along an ion trajectory, and gives β-SiC based nano-wires of which sizes (length, thickness) and number densities are completely under control by changing the parameters of incident ion beams and molecular sizes of target polymers. Recently the techniques of position-selective single ion hitting have been developed for MeV order ion beams, however it is not sufficient to control precisely the positions of the nano-wires on the substrates. In the present study, we report the selective adhesion of nano-wires on Si substrates by the surface treatments before polymer coating, which enables the patterning of planted nano-wires on substrates and/or electrodes as candidates for nano-sized field emissive cathodes or electro-luminescent devices.

Introduction

1-D nano-sized materials such as carbon nanotubes have attracted much attention as ideal quantum wires for future manufacturing techniques of nano-scaled opto-electronic devices[1-3]. However it is still difficult to control the sizes, spatial distributions, or positions of nanotubes by conventional synthetic techniques to date.

The MeV order heavy ion beams cause ultra-high density energy deposition which can not be realized by any other techniques (lasers, ΔH, etc.), and penetrate the polymer target straightforward as long as 1~100 μm depth[4,5]. The energy deposited area produces non-homogeneous field of chemical reactions, so-called a chemical core of an ion track. The dimension of the field can be controlled by changing the energy deposition rate of incident ions (LET: linear energy transfer, eV/nm).

We found that cross-linking reaction of polysilane derivatives was predominantly caused and gave "nano-gel" in the chemical core, unlike main chain scission occurring at the outside of the area[5,6]. Based on the concept of the "single track gelation", the present study demonstrates the formation of cross-linked polysilane nano-wires with the fairly controlled sizes. The selective adhesion of the nano-wires would play a significant role in the spatial positioning, hence the future applications of them.

Experimental

The target polymer, Poly(methylphenylsilane) (PMPS) was synthesized by Kipping method from methyphenydiclorosilane as a monomer, with the molecular weights as Mn = 4.6 ~ 2.2 x 10^5 **(PS1)**, 1.5 ~ 1.1 x 10^5 **(PS2)**, 5.0 ~ 4.0 x 10^3 **(PS3)** which were controlled by changing reaction conditions or fractional precipitation. The polymers were spin-coated on Si substrates after washing by NaOH solution **(Si-hydrophillic)** or immersion in dialkyl-$SiCl_2$-ethanol-water solution **(Si-hydrophobic)**. The irradiation was carried out by using Ar, Kr, and Xe ions from cyclotron accelerator at JAERI-Takasaki, followed by adequate development by ether, tetrahydrofuran, and benzene.

The observation of the nano-wires was carried out by using SII SPI-3800 atomic force microscope (AFM) and JEOL JSM-6335F scanning electron microscope systems.

Results and Discussion

AFM images of the nano-wires formed on **Si-hydrophillic** are displayed in Fig. 1. As the 3-D image indicating, the cross section of each nano-wire has the radius at 6.0 nm, and the length of nano-wires is 170 nm with high uniformity (± 5%), which completely reflects the initial thickness of the target polymer films. The radii of the nano-wires are changed from 4.3 nm (175 MeV Ar irradiation to a **PS3** film) to 13.4 nm (450 MeV Xe irradiation to **PS1** films), controlled individually by the value of LET of incident ions and molecular weight of the polymers. In spite of wet development procedure after irradiation (washing the uncross-linked part out by solvents), the number density of the nano-wires is proportional to the number of incident ions. This strongly suggests that the one end of each nano-wire tightly connected to a **Si-hydrophillic** surface.

Fig. 2 shows SEM images of the nano-wires formed on **Si-hydrophobic** after the same procedures and conditions of wet development as those for Fig. 1. It is clear that the nano-wire is no longer isolated in this case, and entangled each other. The aggregated nano-wires are rarely and randomly distributed on the substrate, and the majority is washed out together with uncross-linked parts of the film. It is due to separation during the development and/or intrinsic anti-bonding feature between the surface and the ends of nano-wires. This also suggests that the position of the nano-wires can be controlled by making a pattern of surface treated area on a substrate, unless using the techniques of position-selective ion hitting.

Conclusion

The selective adhesion by the surface treatment is useful for the positioning of the nano-wires on a substrate. We believe that the 2-D patterning will be a breakthrough for future applications of the well-defined size-controlled nano-wires formed by the present technique.

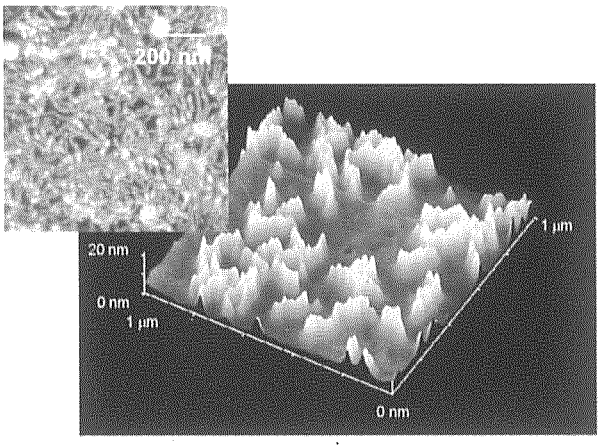

FIG. 1 3-D AFM images of nano-wires adhered on a Si substrate observed on Si-hydrophillic. The nano-wires were formed by the 450 MeV $^{128}Xe^{23+}$ irradiation to a **PS3** thin film (170 nm thick) at 7.5 x 10^{9} ions/cm^{2}. Superimposed top-view picture was taken for a specimen irradiated at4.0 x 10^{10} ions/cm^{2}.

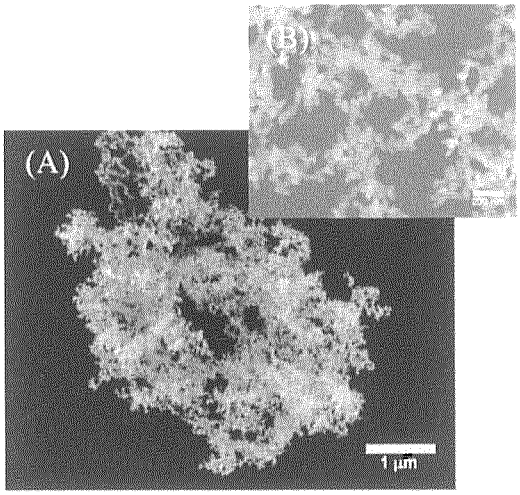

FIG. 2 A SEM image of condensed nano-wires on a Si substrate. The nano-wires were formed by the 450 MeV $^{128}Xe^{23+}$ irradiation to a **PS1** thin film (0.45 μm thick) at 1.0 x 10^{11} ions/cm^{2}. A superimposed figure indicates the enlarged view of the nanowire entanglements.

References

1) Iijima. S *Nature* **354**. 56-58 (1991). 2) Tans. S. J., et al. *Nature* **386**. 474-477 (1997). 3) Bockrath. M., et al. *Science*. **275**. 1922-1925 (1997). 4) Magee. J. L. & Chattarjee, A. Kinetics of Nonhomogenious Processes, G. R. Freeman Ed., Chapter 4, p.171-214 (1987). 5) Seki, S., et al. *J. Phys. Chem.* **B103**, 3043-3048 (1999). 6) Seki, S., et al. *Adv. Mater.* **13**, 1663 (2001).

3.4 Oxidation product yields of phenol along heavy ion trajectory in aqueous solution : Differential G-value.

Mitsumasa Taguchi, Nguyen Minh Thu, Takuji Kojima
Department of Radiation Research for Environment and Resources, JAERI

1.Introduction

It is well known that the yields of transient species and final products change along the heavy ion trajectories in water[1,2]. Reactive transient species, *e.g.*, OH radical and hydrated electron, are produced in water by heavy ion irradiation. The initial distributions of the transient species corresponding to the initial dose distribution are non-homogeneous around the ion trajectory. Heavy ions form spurs densely around their trajectories, while low LET radiations form spurs sparsely. The transient species produced in the track are so near as to interact easily with each other. Therefore, the changing the yield along the trajectory of the ion will be due to the magnitude of interactions between transient species in the track. It is necessary to have a detailed knowledge about dependence of the differential *G*-value (the yield at a particular energy or LET of an ion in the sample solution) of products by OH radical upon kind and LET of the ions. In the present report, we investigated the differential *G*-value of oxidized products from aqueous phenol solutions irradiated with several hundred MeV C, Ne, and Ar ions.

2.Experimental

Water containing phenol of 10-mM concentration was saturated with helium gas for 30 minutes to purge dissolved oxygen. The solution was put into an aluminum cell with a magnetic stirrer chip. The cell has an aluminum window of 15-μm thickness and 40-mm diameter for the irradiation. The volume of the sample solution was 5.4 mL and its depth was about 4 mm.

Irradiations were performed with 220-MeV $^{12}C^{5+}$, 350-MeV $^{20}Ne^{8+}$, and 460-MeV $^{40}Ar^{13+}$ ions using 'Irradiation Apparatus for Seed'[2] in TIARA facility. The ion beams were scanned in the X and Y directions at 1 and 50 Hz, respectively, to provide uniform intensity (fluence rate) at the surface of the sample cell. The scanning area was over 50-mm square at the sample surface. The different energy ions were provided by the attenuation of the incident energy using a set of aluminum foils with difference thickness of 10- to 500-μm installed on the sample cell. The incident energies, the energies of the ion at the surface of the sample solution after penetrating the aluminum foils and the windows, were calculated using the TRIM code[3]. Penetration depth of the ion was less than 1.1 mm in water. Therefore, the sample solution was stirred during the irradiation by a magnetically coupled stirrer chip to keep the solution homogeneous. Changing the irradiation time up to 200 seconds controlled dose. For comparison, the sample solution was also irradiated with ^{60}Co γ-rays as a low LET radiation.

The irradiated sample solutions were analyzed by High Performance Liquid Chromatography (HPLC) with a reversed phase column (Shodex, Rspak DE-613) at 40 ℃. Acetonitrile mixed with 70-% aqueous H_3PO_4 solution (0.01 M) was used at a flow rate of 1.0 mL/minute as an eluent.

3.Results and discussion

Hydrouinone and catechol were identified as products after the Ar ion irradiations from the HPLC chromatogram, as shown in Figure 1. Concentrations of these oxidized products were estimated from the integration of the spectral area around the relevant specific peaks on chromatograms. Yields of the oxidized products increased linearly with an increase of dose.

The number of molecules (*N*) produced by a

single ion is estimated from the concentration (C) of the oxidized product and fluence (F) of the incident ion:

$$N = C \times 0.0054 / F \times N_A \quad (1)$$

where N_A is the Avogadro's number. All the incident ions stop completely in the sample solution so that N is the number of molecules of the oxidized products integrated over the trajectory. As can be seen from Figure 2, N increased steeply with increasing incident energy ($E0$). The increment tendency was different among the used ions. N corresponds to the value of the differential G-value (G'), the G-value at a particular energy of the ion in the particular position of the sample solution, integrated over the trajectory:

$$N = \int_0^{E0} G' \, dE \times 100. \quad (2)$$

The G'-values were estimated from the first derivative of the fitted curve of N as a function of E. The G'-values estimated for each E value were plotted against LET as shown in Figure 3. The G'-values of hydroquinone and catechol for the each ion decrease with increasing LET value of the same ion. In other word, the G'-values are different among the different kind of the ions even at the same LET value. Such a LET dependence of the G'-value suggest a need of introduction of a new interpretation based on the characteristic energy distributions of heavy ions.

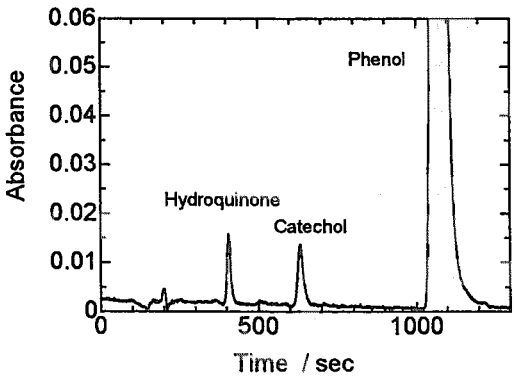

Figure 1 HPLC chromatograph of aqueous phenol solution after Ar ion irradiation.

References

1) A. Appleby, *et al.*, *Radiat. Res.*, 104, 263 (1985).

2) M. Taguchi, *et al.*, *Radiat. Phys. Chem.*, 60, 263 (2001).

3) J.F. Ziegler, *et al.*, The Stopping Power and Range of Ions In Solid, vol. 1, Pergamon Press, New York, 1985.

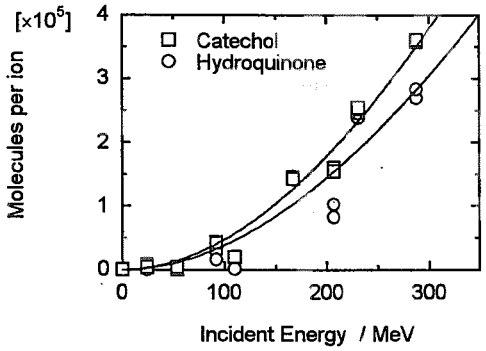

Figure 2 Number of molecules produced from phenol in water by single Ar ion irradiation.

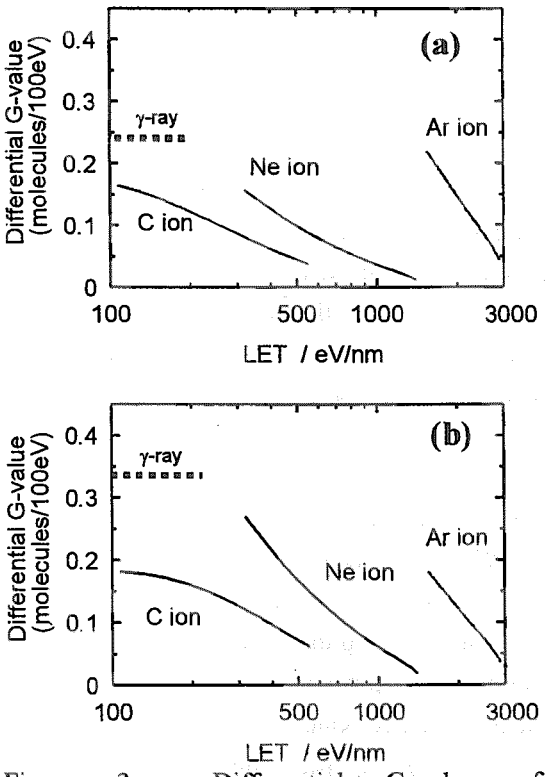

Figure 3 Differential G-value of hydroquinone (a) and catechol (b) in aqueous phenol solution irradiated with C, Ne, and Ar ions. Broken lines show G-values of interested products for ^{60}Co γ-rays.

3.5 Crosslinking of Polymers in Heavy Ion Tracks

H. Koizumi*, M. Taguchi**, Y. Kobayashi**, and T. Ichikawa*
Division of Molecular Chemistry, Graduate School of Engineering, Hokkaido University*, Department of Radiation Research for Environment and Resources, JAERI**

1. Introduction

Local dose in heavy ion tracks is very high. The local dose is higher than several polymers that crosslink by ionizing radiation [1,2]. Gelation hence occurs in each ion track. A "gel string" is generated[3-6]. In the previous report, we have studied the formation of gel string in polydimethylsiloxanes by 256 MeV Ar ion irradiation. Dependence of weight of a gel was examined.

In this study, we have examined the dependence on ion beams to get further insight on crosslinking in a heavy ion track.

2. Experimental

Polydimethylsiloxane (KF96, Mn 60,000) supplied by Shin-Etsu Chemical Co., Ltd. was degassed under vacuum. They were put in metal cells with aluminum window of 25 μm thickness. 460 MeV $^{40}Ar^{13+}$, 350 MeV $^{20}Ne^{8+}$ and $^{12}C^{5+}$ ions from the AVF cyclotron of TIARA were irradiated at HY1 port. The ion passes through a titanium window of 30 μm thickness, distance of 80 mm in 1-atom helium gas, and the aluminum window of the cells. The initial energy of the Ar, Ne, C ions at the surface of polydimethylsiloxane is 256 MeV, 306 MeV, and 204 MeV, respectively. Thickness of liquid polydimethylsiloxanes was sufficiently larger than the ranges of the ion beams.

The irradiated samples were dissolved in hexane. The insoluble residue was separated with membrane filters (Millipore, LSWP04700, pore size 10μm). The weight of the insoluble residue was measured.

3. Results and Discussion

Figure 1 shows the weight of the insoluble residue as a function of ion fluence. The weight is proportional to the ion fluence. Gelation occurs in each ion track indicating that the gel fraction is hence proportional to the number of irradiated ions. Gel fraction of crosslinking polymers irradiated with γ-rays or electron beams is zero at lower doses than a gelation dose. It abruptly increases at doses higher than the gelation dose, and approaches unity. The yield of insoluble residue per ion is 2.0×10^{-14} g ion^{-1} for the Ar ion irradiation, 4.8×10^{-14} g ion^{-1} for the Ne ion irradiation, and 1.1×10^{-14} g ion^{-1} for the C ion irradiation. The range of the ions is 0.13 mm, 0.63 mm, and 1.2 mm, respectively. If we assume that gel strings are cylindrical, the average radius of the strings is 6.0 nm for Ar ion, 4.8 nm for Ne ion, and 1.1 nm for C ion. This difference

ascribed to radial dose distribution in the ion tracks. The radial dose distribution decreases with increasing distance (r) from the center in proportion to $1/r^2$. The radius of the gel strings will be determined by area of dose higher than gelation dose. Figure 2 shows the radius at which dose in the ion tracks becomes the dose of 90% gel fraction. This well explains the experimental radii.

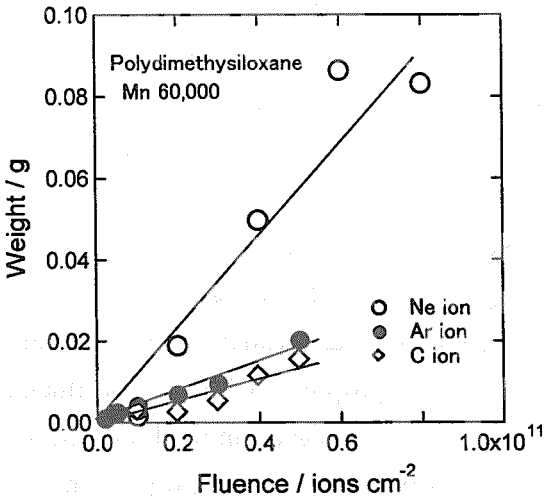

Figure 1. Weight of insoluble residue obtained from polydimethylsiloxane (Mn 60,000) irradiated with 256 MeV Ar(●), 306 MeV (○) Ne, 204 MeV C (◇) ions as a function of ion fluence. The irradiated area is 19.6 cm^2.

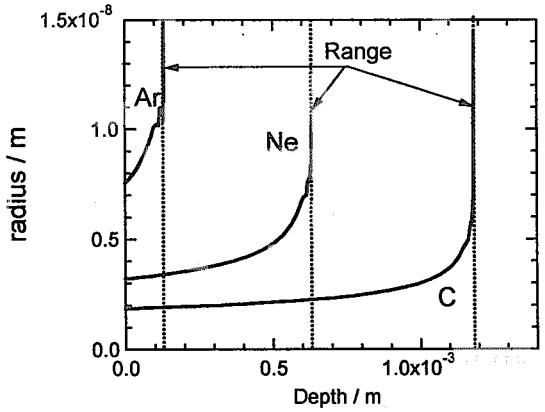

Figure 2. Radius at which dose in the ion tracks becomes the dose of 90% gel fraction plotted as a function of depth from the surface of the polymer.

References

1) H. Koizumi, T. Ichikawa, H. Yoshida, H. Namba, M.Taguchi, T. Kojima: Nucl. Instrum. Meth. B 117 (1996) 431.
2) H. Koizumi, M. Taguchi, H. Namba, T. Ichikawa, H. Yoshida: Nucl. Instrum. Meth. B 132 (1997) 633.
3) H. Koizumi, M. Taguchi, T. Ichikawa, TIARA Annual Report 1998, JAERI-Review 99-025 (1999) 93.
4) H. Koizumi, M. Taguchi, Y. Kobayashi, T. Ichikawa. TIARA Annual Report 1999, JAERI-Review 2000-024 (2000) 91
5) H. Koizumi, M. Taguchi, Y. Kobayashi, T. Ichikawa: Nucl. Instrum. Meth. B 179 (2001) 530.
6) H. Koizumi, M. Taguchi, Y. Kobayashi, T. Ichikawa, TIARA Annual Report 2000, JAERI-Review 2001-039 (2001) 122.

3.6 Primary Process of Radiation Chemistry Studied by Ion Pulse Radiolysis

Y.Yoshida*, S. Seki*, A. Saeki*, S. Tagawa*, M. Taguchi**, T. Kojima**, H. Namba***
ISIR, Osaka University*
Department of Radiation Research for Environment and Resources, JAERI**
Department of Material Development, JAERI***

1. Introduction

Radiation effect of high energy high LET ion beams on the material is very interesting and was investigated by many researchers, because the highlly-densed irradiation makes the different effect from that by low-LET radiation, such as γ rays. We have studied the primary process of the ion beam-induced radiation chemistry by using the technique of ion beam pulse Radiolysis for emission spectroscopy[1-3].

The LET effect on the time-dependent emission could be discovered by using the ion beam pulse radiolysis of the polystyrene. However, the whole mechanism of LET effect can not be elucidated, because the information on the other important short–lived species, such as electron and cation radical, can not be obtained by the mission spectroscopy.

The behavior of other short-lived species can be detected by using absorption spectroscopy. However, there are many difficulties to the absorption spectroscopy, such as the ion beam intensity, the penetration of the ion beam into material, the light source, and so on. A new idea of the absorption spectroscopy system is proposed to overcome the difficulties.

2. Results and Discussion

The lifetime of excimer in solid polystyrene was a constant (20ns), which did not depend on the values of LET. However, the lifetimes of polystyrene excimer were changed in the liquid phase. Figure 1 shows the time-dependent behavior of the emission from polystyrene excimer obtained in 520 MeV Kr^{+20} ion pulse radiolysis of 3, 10, and 100 mM polystyrene solutions in cyclohexane monitored at 330 nm. The emission intensities at various concentrations were normalized at the ion pulse end. In 100 mM solution, the lifetime of polystyrene excimer was 20 ns, which was in agreement with the lifetime of solid polystyrene excimer[1]. In 10 and 3 mM, the fast and the slow decay components were observed. The lifetimes of the slow components corresponded to 20 ns. The ratio of emission intensity of the fast component to that of the slow component increased with decreasing of the concentration of polystyrene.

If the fast and slow components are given by polystyrene excimer, the difference can be explained by a reaction of polystyrene excimer with other short-lived intermediates. To confirm

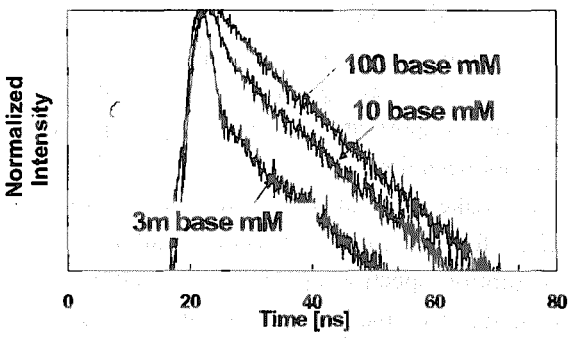

Fig. 1 Time-dependent behavior of polystyrene excimer obtained in 520 MeV Kr^{+20} pulse radiolysis of polystyrene solution in cyclohexane monitored at 330 nm

the reaction, ion beam-induced emission spectra in polystyrene-cyclohexane system were observed by using a streak camera with a monochorometor. The spectra showed the polystyrene excimer as well as solid polystyrene. Therefore, polystyrene excimer in cyclohexane reacts with other short-lived intermediates in the short time region.

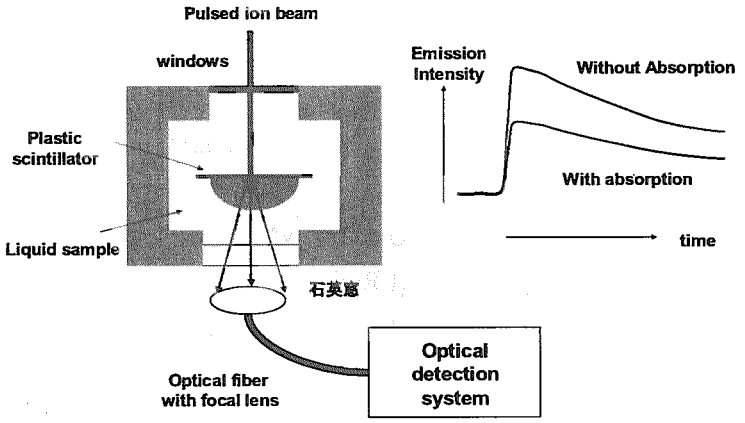

Fig.2 Absorption spectroscopy system for ion beam pulse radiolysis

To discuss the whole process of the LET effect on ion beam-induced reaction, the behavior of electron and cation radical are very important which are first intermediates produced by ion beam, because the higly-densed excitation effect is decreased with the passage of the time by the diffusion motion.

The geminate ion recombination in a spur has been studied by using subpicosecond and picosecond pulse radiolysis. The kinetics of the recombination can be analyzed by the Smoluchowski equation based on the diffusion theory. However, the theory can not be applied to the truck model. The new theory will be necessary to elucidate the problem. Recently, the simulation method for the multi-ion pair model has been developed to analyze the pulse radiolysis date. The LET effect can be analyzed by using the simulation technique. Although the LET effects on the geminate ion recombination are very important phenomena, the experiment has not been done.

To make clear of the highly-densed effect, a plan for an ion beam pulse radiolysis for absorption spectroscopy has been started. It is difficult for the absorption spectroscopy to handle the analyzing light, because optical path length is so short due to small range of the ion beam. A new idea fot the analyzing light will solve the difficulty. Fig. 2 shows the concept of experimental setup. A thin plastic scintillator float on the liquid sample in the sample cell. Pulsed ion beams produce the emission through the plastic scintillator, before the sample is irradiated. The emission is used as the analyzing light. The analyzing light is detected by single photon counting technique. If there is the optical absorption, the observed analyzing light has decreased. The time-dependent behavior of the absorption can be obtained by the analysis of the analyzing light.

In the preliminary experiment, the changing of the analyzing light was detected. The first data will obtain soon by using the new experiment, which makes clear of primary processes of ion beam irradiation near future.

References

1) H. Shibata et al., Nucl. Instrum. Meth., A327, 53, 1993
2) Y. Yoshida et al., Nucl. Instrum. Meth, A327, 41, 1993
3) H. Shibata et al., Nucl. Instrum. Meth., B105, 42, 199

3.7 Dosimetry for 3-45 MeV/u ion beams using thin film dosimeters

T.KOJIMA, H.SUNAGA, H.TAKIZAWA, H.HANAYA, H.TACHIBANA
Advanced Radiation Technology Center, JAERI

1. Introduction

Various advanced material science and biological studies have been performed using ion beams obtained from the TIARA AVF cyclotron (e.g. $^{1}H^{+}$: max. 90 MeV). Practical evaluation of absorbed dose and dose distribution is crucial for interpretation of radiation effects of ion beams on materials or biological substances considering different radiation qualities and inhomogeneity of energy deposition in an interested volume. Dosimetry required for these research works should cover the doses ranging from 0.005 to 200 kGy with high precision within ±5% and the spatial resolution of about 1μm for lateral and depth directions.

Thin film dosimeters of about 10-200 μm in thickness, which are well -characterized for ^{60}Co γ -rays or 2-MeV electrons in the above dose range, have been applied to dosimetry for ion beams, by means of the linear energy transfer (LET) characteristics study of films involving development of precise fluence measurement and dose mapping technique with high spatial resolution[1, 2]. The outline of the development is summarized in this paper.

2.Experimental

The thin film dosimeters: alanine-PE (DL-alanine 60wt%, low density polyethylene 40wt%: 8×30×0.223 mm), Cellulose-triacetate(CTA 85wt%, triphnyl -phosphate 15wt%: 8×50×0.125(or 0.03) mm), Radiochromic (FWT-60: 10×10×0.05 mm) and Gafchromic (MD-1260: 10×10×0.007 mm) were used as candidates applicable also to ion beams. These film dosimeters are enough thin for most of ion beams to completely penetrate. The averaged LET calculated using ELOSS code[3] based on Ziegler's Table[4] , was in agreement within ± 2% with those calculated using TRIM-98 code[5].

The ion beams with the energies ranging 3 - 45 MeV/amu were uniformly scanned to 100×100 mm^2 in area and used for irradiation study on dosimeters under vacuum about 2×10^{-4} Pa. The absorbed dose preliminarily estimated by fluence and stopping power values were chosen in linear dose response range of films when irradiated by the low LET radiations.

Beam fluence was monitored employing a custom-made Faraday cup (suppression:-100V) in terms of integrated charge. In advance to characteristic study of film dosimeters, uncertainty in fluence measurement was estimated by simultaneous use of a total-absorption calorimeter[1,2]. These two detectors were exposed to scanning ion beams through a pair of circular apertures of φ 30 mm in dia.(7.07 cm^2 in area). The fluence values measured by the Faraday cup $\Phi_m(cm^{-2})$ were compared with those estimated from calorimetry based on nominal incident particle energy $\Phi_c(cm^{-2})$. The related ratios of fluence Φ_m and those estimated using energy values derived from the magnetic field amplitude at an analyzing magnet. The average value of the ratios

Φ_m/Φ_c is 1.02 and averaged coefficients of variation for Φ_c is ±2% at a 68% confidence level. These results lead us to confirm that this fluence measurement system is sufficient to use for 3- 45 MeV/amu ion beams covering wide range down to a few nA/cm^2: about 0.01 – 270 nC/cm^2 as integrated charge in the Faraday cup.

3.Dosimeter characteristics study

Dose responses, electron spin resonance signal amplitude per unit dose for alanine, and optical density change per unit dose for others estimated from linear fitting of four dose points were normalized to those for ^{60}Co γ -rays or 2-MeV electrons. All the film dosimeters have a similar tendency showing decrease of relative dose response with increase of linear energy transfer (LET). The scattering range of one dose response is about ±4% at a 68% confidence level. It suggests the applicability of these dosimeters to ion beams when calibrated by low LET radiations with appropriate correction on dose responses on the basis of obtained relations.

4. Dose profile measurement

Gafchromic dosimeter which has only 7 μ m thick sensitive layer was tested for depth dose profile measurement with high spatial resolution by irradiation through a stepping multi-layer polyimide phantom. The result shows a potential of depth dose distribution measurement in 1.2 mg/cm^2 (7.5 μ m) step observing of the Bragg -peaks.

The lateral dose distribution measurement was tried by irradiation of films to 0.5-5 kGy with 450-MeV $^{129}Xe^{23+}$ ions through a Cu mesh mask having 6-μm linewidth and 19-μm line-to-line inner distance. Color change of irradiated area relevant to the mesh pattern on the mask was analyzed using a microscopic spectrophotometer (HITACHI, U-6500). Color change patterns relevant to irradiated areas were clearly identified with sufficient sharpness equivalent to the spatial resolution of 1μm.

5.Conclusion

Overall uncertainty in ion beam dosimetry employing thin film dosimeters is estimated better than ±5% at a 68 % confidence level, by addition in quadrature of uncertainty components of fluence measurement(±2%) and film dosimetry (±4%). This accuracy and spatial resolution of 1μm meet fully the requirement to ion beam dosimetry in material science and biological research using a TIARA cyclotron.

References

1)T.Kojima et al.: Radiat.Phys.Chem., 53, (1998) 115

2)T.Kojima et al.:IAEA-TECDOC-1070 (1999) 197.

3)K.Hata and H.Baba: JAERI-M 88-184 (1988)

4)J.F.Ziegler, J.P.Biersack and U. Littmark : "The stopping power and range of ions in solids", Vol.1(1985) (Permagon Press, Oxford).

5)T.Kojima et al.:JAERI-Conf 2000-1 (2000), 31

4. Inorganic Materials

4.1 Effect of Helium on Ductile-Brittle Transition Behavior in Reduced-Activation 8Cr-2W Martensitic Steel

E. Wakai*, K. Furuya**, K. Oka***, M. Tanaka***, S. Ohnuki***, Y. Kato****, F. Takada****, M. Sato**,T. Sawai* and S. Jitsukawa*

Department of Materials Science, Tokai Establishment, JAERI*, Department of Fusion Engineering Research, Naka Establishment, JAERI**, Faculty of Engineering, Hokkaido University***, Department of JMTR Hot Laboratory, Oarai Establishment, JAERI****

1. Introduction

Low-activation martensitic steels are candidate materials for the first wall and blanket structure of fusion reactors and also prominent materials for the target vessel of spallation neutron source. In these systems, the high-energy neutrons or protons induce displacement damage and generate hydrogen and helium gas atoms in the materials. Helium and hydrogen accumulations due to transmutation and implantation in these systems of martensitic steels have been considered as a potential cause for irradiation-helium-embrittlement [1-5] and -hydrogen-embrittlement [6-7]. In this study, the effect of helium on ductile-brittle transition temperature of martensitic steel has been examined by small-punch test.

2. Experimental

The material used in this study was the F82H reduced-activation 8%Cr martensitic steel (Fe-8Cr-2W-0.2V-0.04Ta-0.1C). Sheet of 0.3 mm in thickness polished by sand paper (#1000) was punched into 3 mm diameter disks. All of the specimens were fixed on the specimen holder by molten indium, and simultaneously implanted with a beam of 50 MeV-He particles, whose range was estimated to be 0.4 mm, from the AVF cyclotron at TIARA facility of JAERI. An energy degrader was used to implant helium into the specimens uniformly. The total helium concentration and displacement damage were estimated to be 100 appm and 0.04 dpa, respectively. The implantation temperature was monitored by thermocouple located at the specimen holder.

Following the helium implantation, small punch (SP) tests were carried out at temperatures between 93 K and RT. The displacement rate was 0.2 mm/min.The DBTT was obtained by measuring the SP-fracture energy, which was defined as the total area below the SP load-deflection curve, at various test temperatures. A disk of 3 mm in diameter was grasped by dies at its peripheral edge and deformed by bulge deformation mode in a cold bath. After the SP tests, the fracture surface was observed by a scanning electron microscope (SEM).

3. Results and Discussion

The load-deflection curves were measured at various temperatures from 93 K to room temperature in the unimplanted and implanted specimens. For the unimplanted F82H steel, the ductile behavior in the curves was observed at temperatures between 110 K and RT and the brittle behavior was seen below 110 K. For the 100 appm He-implanted F82H steel, the brittle behavior was observed below

130 K, and the load-deflection curves were influenced by the implantation below 130 K, but no influence of helium implantation on the load-deflection curves at temperatures betwee 118 K and RT was recognized. In Fig. 1, the dependence of SP fracture energy on test temperature is shown, and the DBTTs in the umimplanted and implanted specimens are about 110 and 130 K, respectively. The shift of DBTT induced by the helium implantation was about 20 K. The fracture surfaces were observed by SEM, and the brittle fracture mode and cleavage were seen in both specimens as shown in Fig. 2. There is no indication of grain boundary embrittlement even at low temperature after the helium implantation to 100 appm.

It is known that there is a correlation between the DBTTs obtained by utilizing standard-size CVN specimen and SP specimen for a variety of ferritic and martensitic steels. The transition temperature (SP-DBTT) is approximately linearly correlated with CVN-DBTT

SP-DBTT = α x CVN-DBTT,

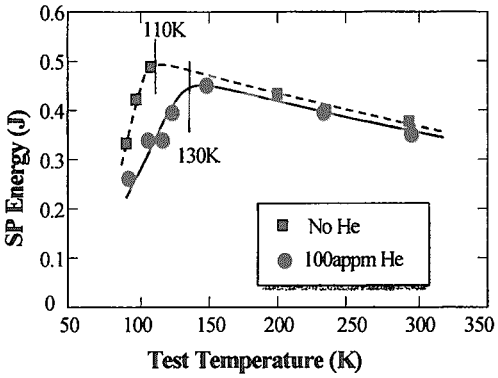

Fig. 1 Dependence of SP-fracture energy on test temperature in F82H.

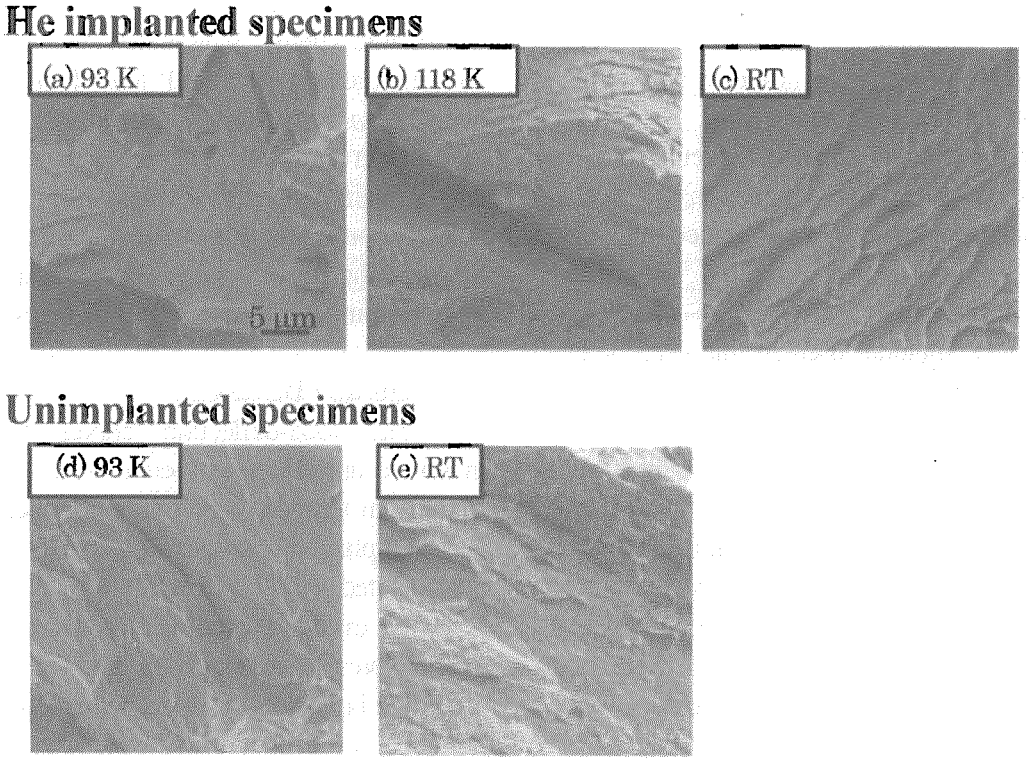

Fig. 2 Fracture surfaces in F82H steel were observed by SEM after the SP tests.
(a) and (d) brittle fracture, cleavage(transgranular) was seen, (b)mixed feature of brittle and ductile fracture, cleavage(transgranular) and dimple were seen, (c) and (e) ductile fracture, elongated dimple was seen.

where α is the correction factor ranging from 0.35 to 0.45 [8-10]. From the equation, the shift in DBTT for standard CVN specimens is estimated to be about 50 K, assuming α = 0.4. This corresponds very well to the result obtained by the isotope-tailoring experiments on helium effects utilizing nuclear transmutation helium from boron-doped F82H specimen [11]. In low dpa level less than 0.1 dpa for F82H steel, the increase of DBTT could be ignored [4,11-12]. Therefore, the cause of shift of DBTT in the helium-implanted specimen is related with helium

4. Conclusions

Helium implantation in a reduced-activation 8Cr-2W martensitic steel (F82H) was performed with a beam of 50 MeV-He particles at temperature below 323 K using a beam energy degrader to obtain uniform distribution of helium up to a concentration of 100 appm. The ductile-brittle transition temperature (DBTT) in the specimen was measured by small punch tests in which the disks of 3 mm in diameter with 0.3 mm thickness were deformed by bulge mode and the fracture surfaces of the specimen were also observed by a scanning electron microscope. The DBTT in the helium implanted specimen was about 130 K and the shift of DBTT was about +20K. The brittle fracture mode and cleavage was observed in both specimens and there was no indication of grain boundary embrittlement even at low temperature after the helium implantation to 100 appm.

Acknowledgement

The authors would like to thank the staffs in the accelerator facilities of Takasaki establishment of JAERI for their help to the implantation experiment.

References

[1] R. L. Klueh, M.A. Sokolov, K. shiba, Y. Miwa, J.P. Robertson, J. Nucl. Mater. 283-287(2000)478-482.

[2] K. Shiba, A. Hishinuma, J. Nucl. Mater. 283-287(2000)474-477.

[3] E.I. Materna-Morris, M. Rieth, K. Ehrlich, Effects of radiation on materials, STP1366, 597-611.

[4] M. Rieth, B. Dafferner, H. -D. Rohrig, J. Nucl. Mater. 258(1998)1147-1151.

[5] N. Yamamoto, J. Nagakawa, K. Shiba, J. Nucl. Mater., 283-287(2000)400-403.

[6] Y. Dai, S.A. Maloy,G.S. Bauer, W.F. Sommer, J. Nucl. Mater. 283-287(2000)513-517.

[7] N. Baluc, R. Schaublin, C. Bailat, F. Paschoud, M. Victoria, J. Nucl. Mater. 283-287(2000)731-735.

[8] J.Kameda, Acta Metallurgica, Vol. 34, No. 12, (1986)2391-2398.

[9] T. Misawa, T. Adachi, M. Saito and Y. Hamaguchi, J. Nucl. Mater., 150(1987)194-202.

[10] T. Mistushita, M. Saucedo, M.L. Joo and T. Shoji, Proceedings, KSME/JSME Joint conference, Fracture and Strength '90, Seoul, Korea.

[11] E. Wakai, M. Sato, K. Shiba, H. Tamita and S. Jistukawa, presented in American Nuclear Society, Nov., 2002.

[12] G.R. Odette. G.E. Lucas and P. Spatig, DOE/ER-0313/27, Department of Energy (2002) p.131.

4.2 Swelling behavior of F82H steel irradiated by triple/dual ion beams

E. Wakai*, T. Sawai*, K. Ando*, H. Tanigawa*, T. Aruga*, K. Oka**, S. Ohnuki**, S. Yamamoto***, H. Naramoto***, K. Kikuchi* and S. Jitsukawa*

Japan Atomic Energy Research Institute, Tokai, Ibaraki 319-1195, Japan*, Hokkaido University, Kita-ku, Sapporo 060-8628, Japan**, Japan Atomic Energy Research Institute, Takasaki, Gunma 370-1290, Japan***

1. Introduction

Helium and hydrogen accumulations due to transmutation and implantation in martensitic steels for the fusion reactor and target vessel of spallation neutron source have been considered as a potential cause for irradiation-induced helium-embrittlement and -hydrogen-embrittlement and irradiation-induced-swelling. The swelling of F82H and other 7-9Cr low-activation steels irradiated at 430°C to 67 dpa in FFTF was reported and the smallest swelling was in F82H (0.1%) compared to the other steels (0.1-0.7%). Recently, the synergistic effect of displacement damage and helium production on swelling in F82H doped with ^{10}B has been examined [1]. The swelling of F82H steel irradiated to 51 dpa was 0.6 to 1.2%, depending on helium concentration, suggesting that the swelling of martensitic steels may be enhanced by He atoms. In this study the swelling behavior of the spallation target materials and the fusion materials under the simulation ion irradiation has been investigated in F82H martensitic steel under triple/dual ion beams [2,3].

2. Experimental procedure

The material used in this study was martensitic steel, F82H (Fe-8Cr-2W-0.2V-0.04Ta-0.1C). Irradiations were performed under triple or dual ion beams in the TIARA facility at JAERI. The specimens were irradiated with a simultaneous triple or dual ions consisting of 10.5 MeV Fe^{3+} ions, 1.05 MeV He^{+} ions, and 0.38 MeV H^{+} ions or the Fe^{3+} and He^{+} ions to 50dpa (displacement per atoms) at 1 μm depth. The damage peak of the Fe^{3+} ions was at 1.75 μm from the surface, and the projected range of irradiation by helium and hydrogen atoms was controlled to be over a range from about 0.85 to 1.30 μm. This was achieved by using two aluminum foil energy degrader, based on calculations with SRIM2000 code. After the irradiation, the microstructures were examined by TEM. Following irradiation, the hydrogen depth profiles in F82H irradiated with triple ion beams were measured at room temperature by using the $^{1}H(^{15}N, \alpha\gamma)^{12}C$ nuclear resonance reaction occurred at 6.385 MeV. $^{15}N^{3+}$ or $^{15}N^{4+}$ ions were accelerated from 5.8 to 13.2 MeV by a Tandem accelerator.

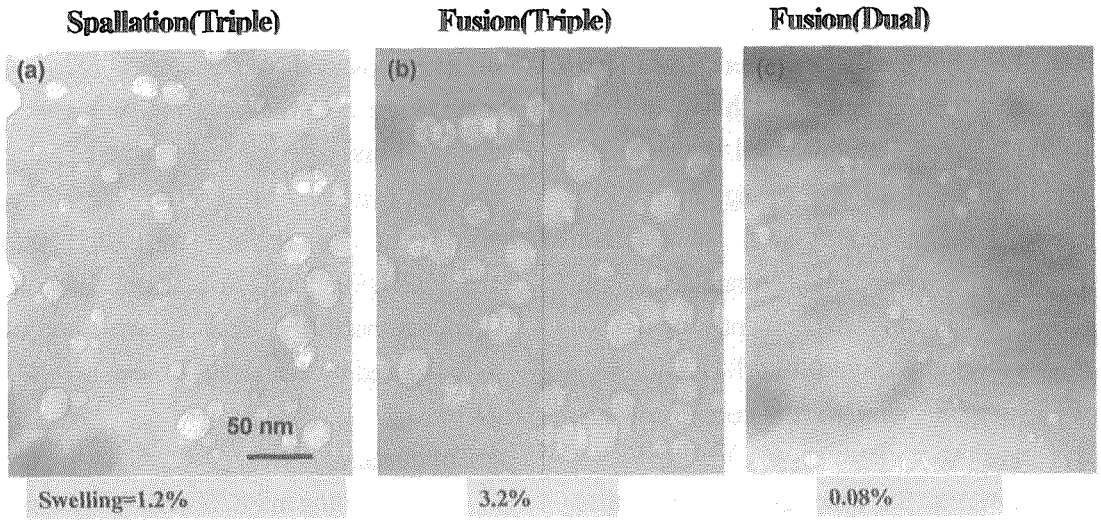

Fig. 1 Simulation experiments of cavities formed in F82H steel irradiated at 470°C to 50dpa and the area is at the depth of around 1 μm. (a) spallation condition(triple beams), (b) fusion condition (triple beams) and (c) fusion condition (dual beams).

3. Results and Discussion

Fig. 1 shows cavities formed in F82H steel irradiated at 470°C to 50 dpa by simulation experiments of cavities for the target vessel of spallation neutron source and first wall of fusion nuclear reactor. A high-density cavity was formed under spallation condition. In fusion condition, the size of cavities formed by the triple beams was larger than that under the dual beams. The size distributions of cavities were bi-modal. The dependence of swelling of F82H steels on irradiation temperature under these conditions is shown in Fig. 2. The swelling under fusion irradiation condition decreased with increasing irradiation temperature. The swelling under spallation condition had a similar tendency but it increased at 600°C. The increase may be affected by the high helium concentration. The densities of dislocations and cavities were decreased with the irradiation temperature and the densities of dislocations under those conditions were nearly equal at a temperature. In the area A, the synergistic

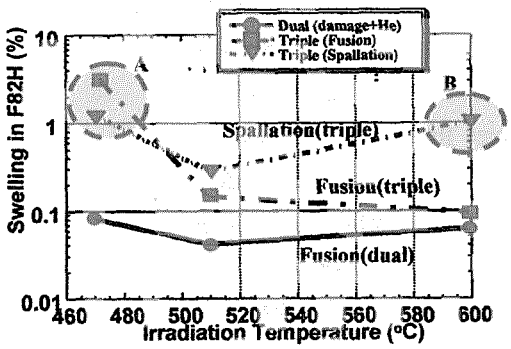

Fig. 2 Dependence of swelling on irradiation temperature in F82H steel.

effect of displacement damage by helium and hydrogen occurred, and in the area B, the enhancement of swelling was caused by the synergistic effect of displacement damage and high concentration helium. In order to examine the diffusion of hydrogen atoms in F82H steel irradiated under the spallation condition, hydrogen concentration was measured by the $^{1}H(^{15}N, \alpha\gamma)^{12}C$ nuclear resonance reaction technique after the triple ion irradiation. After a few week, the depth profiles of hydrogen

in F82H steels irradiated at 80°C to 30 dpa and 470°C to 43 dpa were measured by gamma ray counter as shown in Fig. 3. The hydrogen was detected in the F82H steel irradiated at 80°C in a range from about 0.9 to 1.3 μm, but it was not detected in the specimen irradiated at 470°C. In this experiment, the background level was about 0.13 at%H. Diffusion of hydrogen atoms in iron-based alloys was very fast at 470°C in F82H steel, however, the synergistic effect of displacement damage, helium and hydrogen on swelling in F82H steel occurred remarkably at 470°C. In order to reduce the swelling, the method of the cold working or carbon implantation was performed. The carbon implantation was performed at energies from1.0 to 2.5 MeV with a step of 0.3 MeV at 350°C. Carbides are relatively stable below 400°C, and the formation of dislocation loops gradually decreases above 300°C. The implantation range for carbon atoms corresponds to a range from 0.7 to 1.3μm, which is nearly the same as the helium and hydrogen implanted regions. The concentration of the implanted carbon atoms was estimated to be about 90 appm in peak concentration, and the displacement damage was evaluated to be 0.001 dpa in damage peak. The swelling of F82H+50CW and F82H+90appmC was about 1.4% and 0.5%, respectively, and it was successfully reduced by the heat treatment.

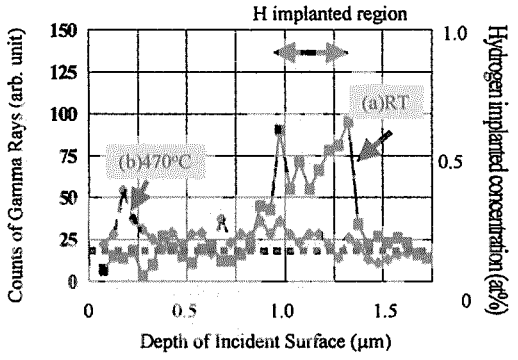

Fig.3 Depth profiles in F82H steels irradiated at 80°C to 30 dpa and 470°C to 43 dpa by a simultaneous triple beams of Fe^{3+}, He^{+} and H^{+} ions Triple beams(Spallation Target) conditions: (a) RT, 6 at%H, 0.8 at%He, 30dpa, (b)470C, 8 at%H, 0.4 at%He, 43dpa.

4. Conclusions

The swelling in F82H steel was enhanced by the synergistic effect of displacement damage by helium and hydrogen. The swelling under fusion condition decreased with increasing irradiation temperature, however the swelling under spallation condition was again increased at 600°C by the high helium concentration. The swelling of F82H steel under the simulation irradiation of fusion condition was reduced by 50% cold-working and carbon implantation, from 3.2% to 0.5 %.

Acknowledgement

The authors are grateful to members of JAERI TIARA facility for the operation of the accelerators during this work.

References

[1] E. Wakai, et al., J. Nucl. Mater., 283-287(2000)799-805.

[2] E. Wakai, et al., presented at the fifth international workshop on spallation neutron source technology, Charleston, SC, USA, 2002.

[3] E. Wakai, et al., submitted in J. Nucl. Mater., (2002).

4.3 Microstructure change with ion beam irradiation in Li_2TiO_3

D. Yamaki, T. Nakazawa, T. Aruga, T. Tanifuji, S. Jitsukawa, A. Iwase
Department of Materials Science, JAERI

1. Introduction

The Li_2TiO_3 ceramic is regarded as one of the most suitable candidates for the solid tritium breeder material of D-T fusion reactors[1]. It is known that, in an operating fusion reactor, the radiation damage in Li_2TiO_3 will be caused by fast neutrons, energetic tritons (2.7MeV) and helium ions (2.1MeV) generated in $^6Li(n,\alpha)^3H$ reaction. The irradiation damage caused by such radiations may result in the microstructure changes, and the changes may affect the characteristics of Li_2TiO_3 such as tritium release behavior, thermal properties, and so on. Thus the study of irradiation defects and microstructure change caused by irradiation in Li_2TiO_3 is essential to evaluate its irradiation performance.

Simulation of the fusion reactor environment and hence the study of a synergistic effect of atomic displacement damage in Li_2TiO_3 are presumed to be approached by a simultaneous irradiation with "triple" ion beams which consist of O^{2+}, He^+ and H^+ ion beams. In the previous study, the formation of the anatase (TiO_2) layer on the surface of Li_2TiO_3 by irradiation with triple ions has been found with Raman spectroscopy and XRD analysis[2]. In the present study, the irradiation damages in Li_2TiO_3 samples irradiated with the single and the triple ion beams were examined with Raman spectroscopy and FT-IR photoacoustic spectroscopy (PAS).

2. Experimental

The Li_2TiO_3 ceramics used in this experiment have been fabricated from 99% pure powder purchased from CERAC, Inc. The powder was cold pressed at 300 MPa into cylinders subsequently sintered at 1223K for 6 h in an Ar atmosphere. The obtained Li_2TiO_3 ceramics have approximately 78% of theoretical density. The specimens were machined from the cylinders to the form of disks with diameter of 10mm and thickness of around 1.0mm.

The Li_2TiO_3 ceramic samples were irradiated at 573K with the single and the triple ion beams of 0.25 MeV H^+, 0.6 MeV He^+ and 2.4 MeV O^{2+}. The fluence of the respective ions were estimated to be $1x10^{21}$ ions/m^2. The ion energies were so chosen that the projected ranges of the irradiated ions in Li_2TiO_3 were around 2.2 μm[3].

3. Results and discussion

3-1. Raman spectroscopy

The Raman spectra of irradiated Li_2TiO_3 samples with the respective single ion beams are displayed in Figure 1. From the comparison with the reference spectra of Li_2TiO_3 ceramics and anatase shown in ref[2], it can be seen that the Raman spectra of Li_2TiO_3 irradiated with single H^+ ion beam and single He^+ ion beam are quite resemblant to the Raman spectrum of reference spectrum of Li_2TiO_3 ceramics. However, the spectrum of the sample irradiated with single O^{2+} ion beam seems to be a superposition of the Li_2TiO_3 and anatase spectra. It clearly suggests that the formation of

anatase on the surface of Li_2TiO_3 observed in the sample irradiated with triple ion beams[2] is mainly caused by the effect of O^{2+} ion irradiation.

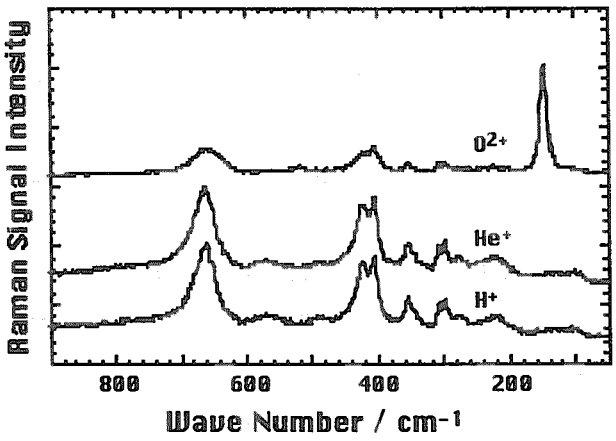

Fig.1 Raman spectra of Li_2TiO_3 ceramics irradiated by O^{2+}, He^+ and H^+ ion beam.

3-2. FT-IR PAS

The FT-IR PAS spectra of Li_2TiO_3 samples with irradiated and non-irradiated with the single and triple ion beams are presented in Figure 2. It should be noted that the photoacoustic signal is generated from the surface layers of sample with a thickness of dozen micrometers which is a function of the mirror velocity of the FT-IR interferometer and wavenumber. In this case, the mirror velocity is 2 cm/s which corresponds to the thickness of about 100 and 30 μm at 400 and 4000 cm^{-1}, respectively. As mentioned in section 2, the ion projection ranges are about 2.2 μm so that the obtained spectra of irradiated Li_2TiO_3 ceramics are a superposition of spectra of irradiated part and non-irradiated part.

The characteristic peaks in FT-IR spectra are observed in three regions; 400-1000 cm^{-1} (Fig.2(a)), 1300-1700 cm^{-1} (Fig.2(b)) and 2700-3700 cm^{-1} (Fig.2(c)). In the region of 400-1000 cm^{-1}, as shown in Fig.2(a), the spectra of samples which are non-irradiated, irradiated with H^+ ion beam and with He^+ ion beam are quite identical, which have the peaks around 450, 600 and 800 cm^{-1}. On the other hand, the signals around 450 and 600 cm^{-1} get smaller and the signal around 800 cm^{-1} becomes larger in the spectra of samples irradiated with O^{2+} ion beam and triple ion beams. It is known that the peaks attributed to Ti-O bonding appears in this region so that the observed changes in the spectra of the samples irradiated with O^{2+} ion beam and triple ion beams may reflect the generation of anatase which is observed with Raman spectroscopy.

In the region of 1300-1700 cm^{-1}, the all spectra have three main peaks around 1420, 1490 and 1550 cm^{-1} as shown in Fig.2(b). The order of peak intensities is as below; O^{2+} ion beam irradiated > non-irradiated = triple ion beams irradiated > He^+ ion beam irradiated > H^+ ion beam irradiated. This fact may suggest that the peak intensity gets larger with O^{2+} ion beam irradiation and smaller with H^+ and He^+ ion beam irradiation, and the effects of the respective ion irradiations are overlaid with the triple ion beams irradiation. In addition, the decrease of the peak intensity observed in the spectra of H^+ and He^+ ion beam irradiated samples also suggest that the microstructure change which is not observed with Raman spectroscopy, besides the formation of anatase, occurs in the Li_2TiO_3 with He^+ and H^+ ion beam irradiation.

In the region of 2700-3700 cm^{-1}, the spectra have three broad peaks around 3050, 3200 and 3480 cm^{-1} as shown in Fig.2(c). It is observed that the spectra of the samples irradiated with O^{2+} ion beam and the triple ion beams closely

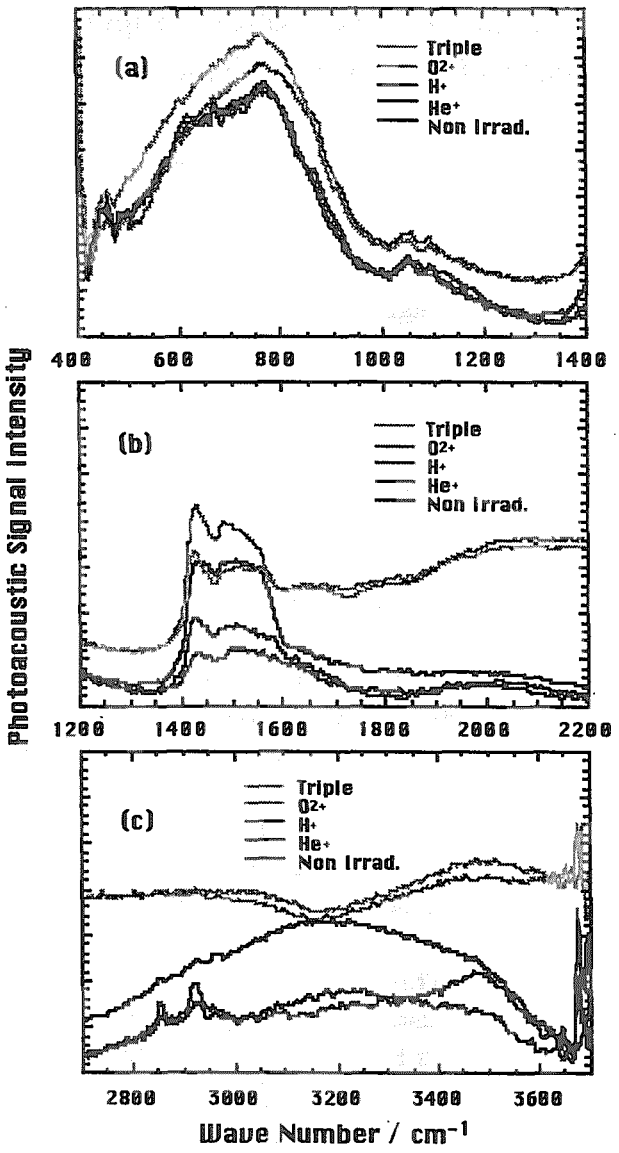

Fig.2. FT-IR PAS spectra of Li_2TiO_3 ceramics irradiated and non-irradiated by the single and triple ion beams.

coincide with each other, although the peakintensity of 3200 cm^{-1} also gets smaller in the spectra of the samples irradiated with H^+ and He^+ ion beam. This suggests that the effects of the respective ion irradiations are not overlaid with the triple ion beams irradiation in this region, differing from the case of the peaks of 1420, 1490 and 1550 cm^{-1} shown in Fig.2(b). It is also observed that the peak intensity around 3480 cm^{-1} gets smaller in the spectrum of the sample irradiated with H^+ ion beam. This supports that the some microstructure changes which do not occur in Li_2TiO_3 with He^+ ion beam irradiation may occur with H^+ ion beam irradiation.

4. Conclusion

The microstructure changes in Li_2TiO_3 irradiated with the single and the triple ion beams of H^+, He^+ and O^{2+} ions were observed with Raman spectroscopy and FT-IR PAS. The results of Raman spectroscopy suggest that the formation of anatase layer on the surface of Li_2TiO_3 is mainly caused by the O^{2+} ion irradiation. The generation of other unknown compounds with irradiations, the difference of the irradiation effects among the different kinds of ion irradiations and the effect of the simultaneous multiple ion beams irradiation are observed with FT-IR PAS measurement. The fact that the irradiation effects of multiple ion beams are not the sum of those of respective ion beams indicates the importance of the multiple ion beams irradiation experiment on the study of the irradiation behavior under the complex irradiation condition such as the fusion reactor environment.

Reference

[1] P. Gierszewski, Report no CFFTP G-9561, 1995.

[2] T. Nakazawa et al., JAERI-Review 2001-039 (2001) 146.

[3] T. Nakazawa et al., 2000 Int. Comf. on Ion Implantation Technology Proc.(2000)753.

4.4 Effect of Multi Ion-beams Irradiation on Mechanical Properties of Advanced SiC/SiC Composites for Fusion Systems

A. Hasegawa*, S. Nogami*, N. Igawa**, E. Wakai**, T. Taguchi**, S. Jitsukawa**

Department of Quantum Science and Energy Engineering, Tohoku University*, Department of Materials Science, JAERI**

1. INTRODUCTION

Silicon carbide (SiC) fibers reinforced SiC matrix composites (SiC/SiC composites) are considered to be one of the candidates for the blanket and shielding structural materials of fusion systems. These materials will be exposed to high energy (about 14 MeV) neutron irradiation. The displacement damage and transmutation caused by the neutron irradiation will occur. Transmutant products during neutron irradiation are dependent on the neutron energy spectrum. The cross-section of (n, α) and (n, p) reactions is relatively large under 14 MeV neutron irradiation. Therefore, helium (He) and hydrogen (H) gases will be formed in these materials. The He and H concentrations per dpa (displacement per atom) on the ARIES SiC blanket are calculated to be approximately 130 at.ppm and 50 at.ppm in the first-wall component, respectively [1].

The material property change of SiC/SiC composites due to the simultaneous existence of displacement damage, H and He is need to be clarified because the solubilities of H and He in SiC are very low and these gases may affect clustering of point defects. Nevertheless study on them has been limited [2-5]. Especially, the knowledge on the synergistic effects of displacement damage, H and He on the recent advanced SiC-fibers is very limited [3, 5]. SiC-fibers used in SiC/SiC composites developed for fusion systems have been improved recently. Stoichiometric SiC-fibers with almost no oxygen such as Hi-Nicalon™ Type-S and Tyranno™ SA are considered to be very promising in the view of the neutron irradiation resistance because they have dimensional and microstructural stability during irradiation [3,5], while non-stoichiometric SiC-fibers, for example Nicalon CG and Hi-Nicalon, were unstable under irradiation [2, 4, 6]. Therefore, lack of the clear understanding of the synergistic effects on these radiation-resistant SiC-fibers has to be essentially solved.

The purpose of this study is to investigate the synergistic effects of displacement damage, H and He on the mechanical properties of advanced SiC/SiC composites by using multi ion-beams irradiations at TIARA facility.

2. EXPERIMENTALS

Materials used in this study were a SiC/SiC composite with Hi-Nicalon™ Type-S fiber and a monolithic polycrystalline β-SiC. The interface material between SiC-fibers and SiC-matrix of the SiC/SiC composite was the pyrolytic graphite (~150 nm in thickness), which was fabricated by a CVD (chemical vapor deposition) process. SiC-matrix (polycrystalline β-SiC) was fabricated by an FCVI (forced chemical vapor infiltration) process. These processes were carried out at the High Temperature Materials Laboratory (HTML) of the Oak Ridge National Laboratory (ORNL). The monolithic β-SiC was fabricated by a CVD process at Roam&Haas. These samples were machined for irradiation tests into the form of 2 mm x 4.5 mm x 0.4 mm.

The simultaneous triple-ion beam irradiation was carried out at TIARA facility. The ions were 6.0 MeV-Si^{2+}, 1.0 MeV-He^{+} and 0.34 MeV-H^{+}. The He- and H-ions were irradiated using energy

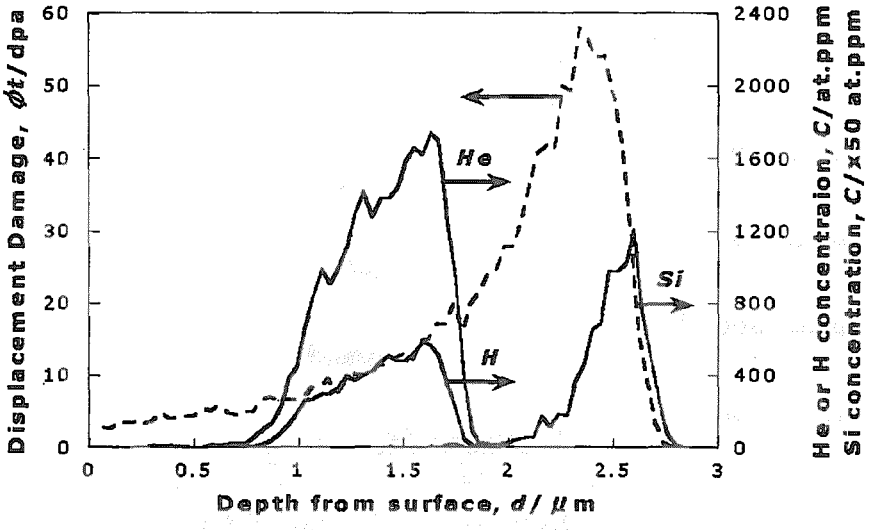

Fig. 1. Distribution of the displacement damage, and concentrations of He-, H- and Si-atoms in Type-S fiber calculated with TRIM-code.

degraders consisting of thin Al-foil. Fig. 1 shows the depth distributions of the displacement damage, and concentrations of He-, H- and Si-atoms in Type-S fiber calculated with TRIM-code [7]. The calculation was performed with the target density of 3.1 g/cm^3 [8] and the threshold energy of displacement damage of 20 eV for C-atom and 35 eV for Si-atom [9]. The displacement damage, He- and H-concentrations at the depth of 1.2 μm were ~10 dpa, ~1300 at.ppm and ~500 at.ppm, respectively. Irradiation temperatures were 1000°C and 1300°C.

Nano-indentation tests were performed using the MZT-4 (Akashi Corporation, Japan), which was equipped with a Berkovich diamond tip (68° semi-apex angle). Indentations were performed under the conditions of the constant loading (unloading) rate dP/dt and the constant maximum indentation depth h_{max}. The values dP/dt and h_{max} in this study were 3 gf/s and 150 nm, respectively. Indentations for the Type-S fibers in this study were performed in the parallel direction of the fiber-axis.

The hardness *HUT[68]* and elastic modulus E can be obtained from the load-displacement curve during indentation. *HUT[68]* was calculated from the following formula:

$$HUT[68] = k\,(P_{max} / h_{max}^2) \qquad (1)$$

where P_{max} is the maximum indentation load and k is the constant.

The procedure given by Doerner et al. [10] was used for the evaluation of an elastic modulus. The slope S of the initial unloading curve can be used for the evaluation in this procedure. The details of this procedure are written in the open literature [10].

3. RESULTS AND DISCUTTION

The calculated hardness *HUT[68]* and modulus E reflect average values of them at the plastically deformed region around the indenter imprint. Since the indentation was performed from the irradiated surface of the specimens in this work and the triple-ion beam irradiated region was at the depth of about 1 to 1.8 μm from the irradiated surface as shown in Figure 1, the adequate maximum indentation depth h_{max} has to be determined so that the plastically deformed region can be in the triple-ion beam irradiated region. Nogami et al. [11] reported that lower values of the hardness and the elastic modulus were observed when the distance from the specimen edge was smaller than about eight times the maximum indentation depth. Samuels et al. [12] investigated the sensing distance from the elastic-plastic boundary in an infinite material and a semi-infinite material including an edge for brass. From this report, the sensing

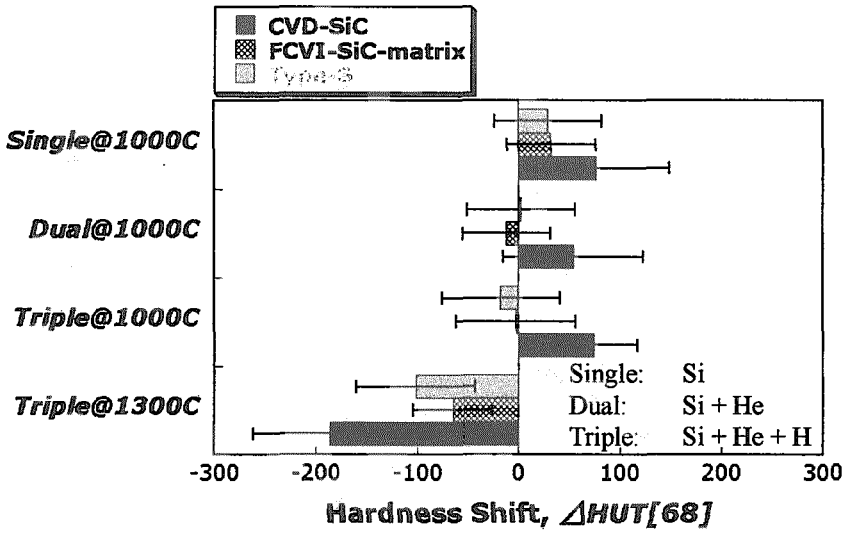

Fig. 2. The hardness changes after triple-ion irradiation on the Type-S SiC-fiber, SiC-matrix and monolithic β-SiC.

distance from the elastic-plastic boundary in the infinite material was almost the same as that in the semi-infinite one. In the view of the results by Nogami et al. [11] and Samuels et al. [12], the plastically deformed region in this study can be about eight times the maximum indentation depth h_{max}. Therefore for evaluating the mechanical property of the triple-ion irradiated region, h_{max} was determined to be about 150 nm. By using this condition, the mechanical property change after irradiation at the depth of 1.2 μm (~10 dpa, ~1300 at.ppm-He, ~500 at.ppm-H) could be evaluated.

Fig. 2 shows the hardness changes after the triple-ion irradiation on the Type-S SiC-fiber, SiC-matrix and monolithic β-SiC. Almost no change was observed on the hardness of the Type-S fiber and SiC-matrix after irradiation at 1000°C, while the hardness of the monolithic β-SiC increased at 1000°C. The hardness of three materials decreased after irradiation at 1300°C. The observed trends in the modulus were almost the same as those in the hardness.

Fig. 3 shows the comparison of the hardness changes of the He-ion-implanted and annealed monolithic β-SiC and the non-implanted and annealed one with triple-ion-irradiated one. He-ion implantation was performed at the temperature below 100°C using the energy-degrader. He-concentration in the uniformly implanted region was about 1000 at.ppm. The reduction of the hardness was observed on the He-implanted β-SiC annealed at 1200°C, while no change was observed on the β-SiC non-implanted and annealed at 1200°C. The He-mobility in a β-SiC increased above about 600°C from the result of the THDS (Thermal Helium Desorption Spectrometry) measurements [11]. These result of the hardness change of the He-implanted β-SiC and the THDS measurements indicates that the reduction of the hardness and the elastic modulus on the triple-ion irradiated β-SiC at 1300°C might be due to the microstructural change by the migration of the implanted-He.

Microstructural observations are required and are being performed to clarify the mechanism of the mechanical property change reported here.

4. SUMMARY

The hardness and elastic modulus changes of the Hi-Nicalon™ Type-S SiC-fiber and SiC-matrix in the SiC/SiC composite and monolithic polycrystalline β-SiC after the simultaneous triple-ion beam (Si-, H- and He-ions) irradiation at 1000°C and 1300°C were investigated and was compared with the He-implanted and annealed β-SiC. The following results were obtained;

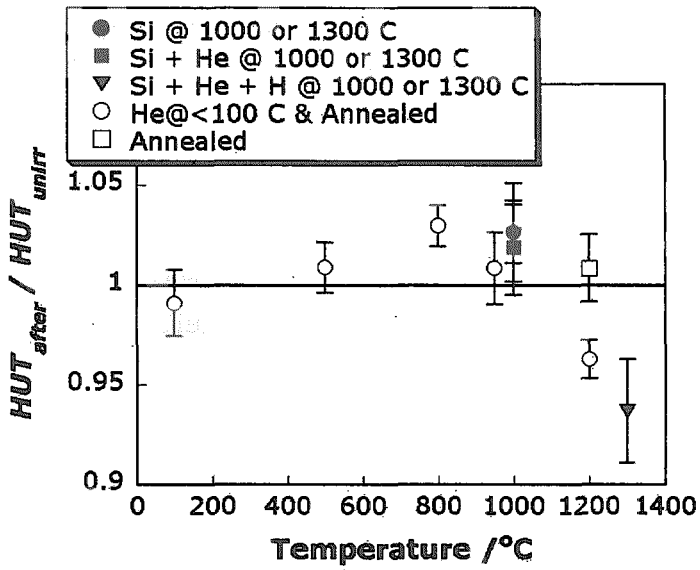

Fig. 3. The comparison of the hardness changes of the He-ion implanted and annealed monolithic β-SiC with triple-ion irradiated one.

(1) Almost no change was observed on the hardness of the Type-S fiber and SiC-matrix after irradiation at 1000°C, while the hardness of the monolithic β-SiC increased at 1000°C.
(2) The hardness of the Type-S SiC-fiber, SiC-matrix and monolithic β-SiC decreased after irradiation at 1300°C.
(3) The reductions of the hardness and the elastic modulus were observed on the He-implanted β-SiC annealed at 1200°C, while no change was observed on the one non-implanted and annealed at 1200°C.

ACKNOWLEDGEMENTS

The authors are grateful to Dr. L.L. Snead (Oak Ridge National Laboratory) and Dr. A. Kohyama (Kyoto university) for providing the SiC/SiC composite material. We wish to thank all the staffs of the electrostatic accelerator group of TIARA for their operation of the accelerator.

REFERENCES

1) L. El-Guebaly, ARIES II/IV Report, to be published.
2) S. Nogami et al., Mater. Trans. Vol. 42, No. 1 (2001) 171-175.
3) T. Taguchi et al., J. Nucl. Mater. in press.
4) S. Nogami et al., J. Nucl. Mater. 283-287 (2000) 268-272.
5) H. Kishimoto et al., to be published in J. Nucl. Mater.
6) A. Hasegawa et al., J. Nucl. Mater. 231 (1996) 245-248.
7) J.F. Ziegler et al., The stopping and Ranges of Ions in Mater. Vol. 1. Pergamon, New York, 1985.
8) M. Takeda et al., J. Nucl. Mater. 258-263 (1998) 1594-1599.
9) S.J. Zinkle et al., J. Nucl. Mater. 251 (1997) 200-217.
10) M.F. Doerner et al., J. Mater. Res. 1(4) (1986) 601-609.
11) S. Nogami et al., to be published in the Effects of Radiation on Materials, ASTM STP 1447.
12) L.E. Samuels et al., J. Mech. Phys. Solids. Vol. 5 (1957) 125-134.

4.5 Damage evolution in high energy multi ion-irradiated BCC metals and the interaction between gas atoms (H and He) and damage defects

I. Mukouda*, Y. Shimomura**, D. Yamaki***, T. Nakazawa***, T. Aruga*** and S. Jitsukawa***
Graduate School of Engineering, Hiroshima University*, Hiroshima Institute of Technology**, Department of Materials Science, JAERI***

1. Introduction

For fusion reactor applications, there is an interest in vanadium and its alloys. Hydrogen and helium atoms are generated by nuclear transmutation in the fusion environment. These gas atoms play an important role in the evolution of the damage microstructure. It is well known that helium is active in cavity nucleation. Sekimura et al. [1] have carried out on multiple beam ion irradiation to study the role of gases. In the present work, quantitative experiments were carried out study the role of helium and hydrogen in the evolution of damage microstructure in irradiated materials. It is possible to control the concentration of gas atoms in irradiated metals by ion irradiation at high energy. We examined void formation in high energy ion-irradiated pure vanadium by both single beam (5 MeV Ni) and dual-beam (5MeV Ni ion and 600 keV He or 260kV H ion) irradiation. The ion energy was selected so that the projected range of the gas ions in vanadium might coincide with depth of peak damage (1.3 μm) calculated by the TRIM 95 code. Specimens for TEM cross sectional observation were prepared by a FIB (Focused Ion Beam) device. The relation between gas atoms and damage structure was derived from experimental results.

2. Experimental Procedure

The pure vanadium had a nominal purity of 99.8%. This material was called as-received V (V(AR)). Some specimens were degassed by melting in vacuum at 10^{-5} Pa in a levitation furnace [2]. This specimen was called residual-gas-free V (V(RGF)). Annealed disks of 3mm in diameter and 0.05 mm thick were prepared from each material. The irradiation was carried out with the TIARA (Takasaki Ion Accelerators for Advanced Radiation Application) accelerators at the Takasaki-establishment of JAERI (Japan Atomic Energy Research Institute) at 500 and 600°C. The ion energy was selected so that the projected range of the gas ions in vanadium coincides with the depth of peak damage (1.3 μm) calculated by the TRIM 95 code [3]. The peak damage rate was 2 x 10^{-3} dpa/s and total dose at the damage peak was 22 dpa. The ions stop within the depth of two microns from the surface and damage was formed up to this depth. For quantitative investigation, the damage structure has to be observed as a function of depth. We utilized FIB microscopy. The FIB generates 30 keV Ga ions and illuminates specimen surface with glancing angle. To preserve the surface of the ion-irradiated metals from sputtering, we deposited tungsten on the irradiated surface. In our previous work, it was found that interstitial atoms form near surface clusters throughout FIB-thinned specimens. To overcome this difficulty, we developed a TEM specimen preparation method which is a combination of FIB thinning and electro-polishing [4-6]. To remove regions damaged by the Ga ions, the

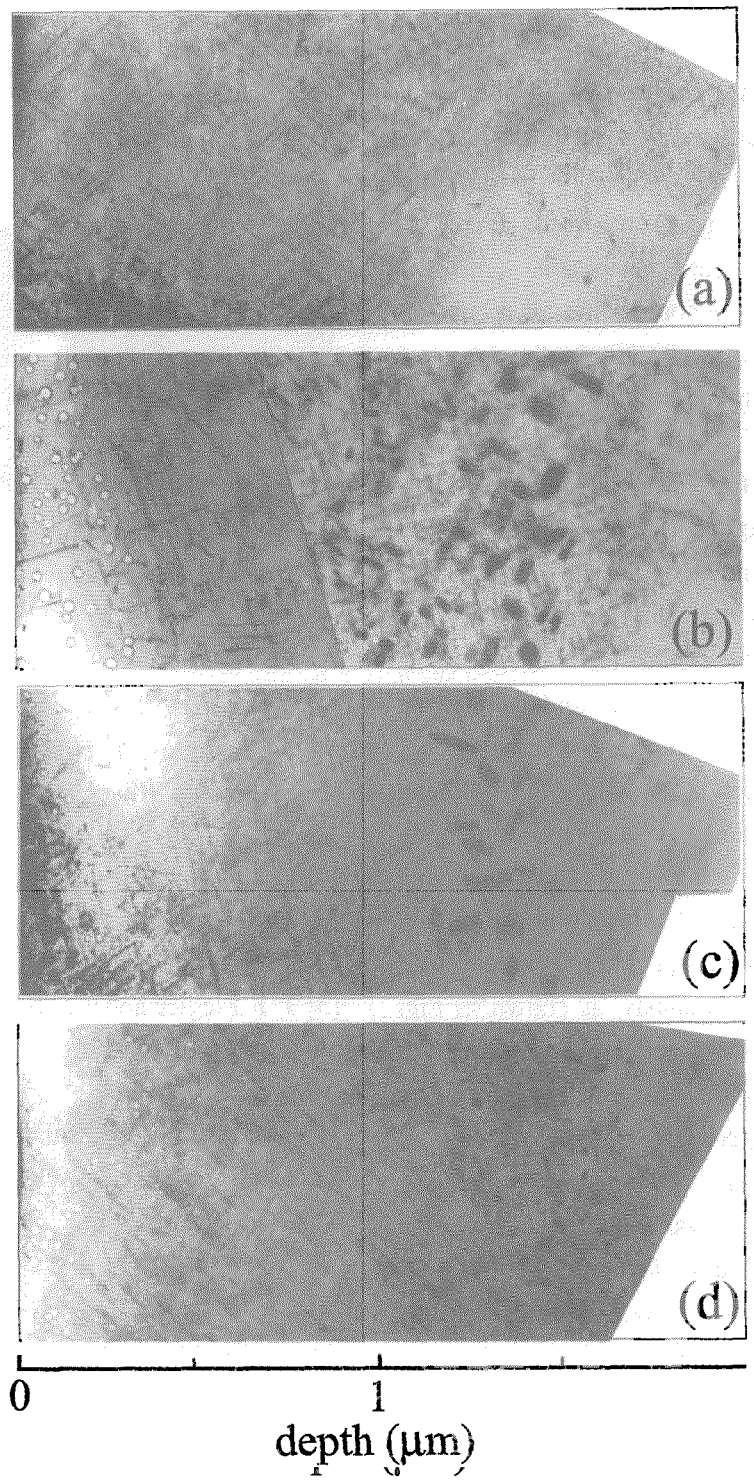

Fig. 1 Damage structure of ion-irradiated, as-received pure vanadium. (a) 5MeV Ni ion irradiation at 500°C, (b) 5MeV Ni ion irradiation at 600°C and (c) 5MeV Ni + 0.26MeV H ion irradiation at 600°C (d) 5MeV Ni + 0.6MeV He ion irradiation at 600°C.

specimens were electro-polished in a solution of 20% H_2SO_4 and 80% methanol cooled to -30°C at an applied potential of 12V for 1 sec. The specimens were electro-polished to remove the region damaged by FIB. After electro-polishing, no dot type defects were observed.

3. Results and Discussion

When only nickel ions were used, voids formed in the region from the surface to a depth of about 0.5 μm when irradiated at 500 and 600°C, as shown in Fig. 1(a) and 1(b). However, in the region of the damage peak, voids were not observed. Needle-like precipitates of about 100nm in length were observed in all specimens covering the whole penetration depth of the ion. It is thought that the precipitate is some type of carbide, because there is oriented <100> direction [7] and the specimen includes a few hundred ppm carbon as a impurity. Moreover, in the specimen irradiated at 600°C, granular precipitates were observed in the region of 1.0 to 1.5 μm depth. In the case of Ni + H irradiation, the size of the voids was small and the number density was similar to that in the case when only nickel ions were used, as shown in Fig. 1(b) and 1(c). Void swelling was suppressed by simultaneous hydrogen irradiation. Void formation was observed within the whole ion penetration depth in the specimen irradiated with Ni + He ions simultaneously, as shown in Fig. 1(d). The needle-like precipitate was observed. Needle-like precipitation formed in any combination of Ni, Ni + H, Ni + He irradiation, but void formation depended on gas ion implantation. In pure vanadium, helium atoms promote void nucleation for irradiation at 500 and 600°C in the low dose region. In the case of Ni + H irradiation at 500°C, small voids were observed within the whole ion penetration depth, while hydrogen atoms suppressed void formation in the case of irradiation at 600°C. These results show that hydrogen atoms trap small vacancy clusters at 500°C, and vacancy clusters and H atoms or molecules dissolved with increasing temperature. Fig. 2 shows void contrast images of depth in 0.1-0.5 μm for V(AR) and V(RGF), respectively. In Fig. 2(b), the number of needle-like precipitates decreased compared with that in Fig. 2(a). It is thought that precipitates acting as a sink were decreased by melting in vacuum.

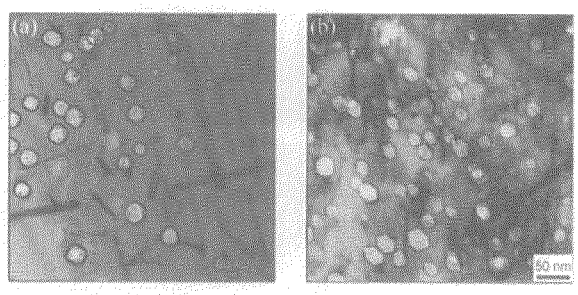

Fig. 2 Void formation in 0.1-0.5μm region irradiated with only nickel at 600°C (a) V(AR) (b) V(RGF).

References

[1] N. Sekimura, T. Iwai, Y. Arai, S. Yonamine, A. Naito, Y. Miwa and S. Hamada, J. Nucl. Mater., 283-287 (2000) 224-228.

[2] K. Sugio, Y. Shimomura, I. Mukouda and M. Kiritani, Radiation Effects and Defects in Solids, 157 (2002) 43-51.

[3] J. F Ziegler and J.P. Biersack, The Stopping and Range of Ions in Solids (Pergamon Press, New York, 1985)

[4] I. Mukouda, Y. Shimomura, T. Iiyama Y. Katano, D. Yamaki, T. Nakazawa and K. Noda, Mat. Res. Soc. Symp. Proc. Vol. 540 (1999) 549-554.

[5] Y. Shimomura and I. Mukouda, Mat. Res. Soc. Symp. Proc. Vol. 540 (1999) 527-532.

[6] I. Mukouda, Y. Shimomura, T. Iiyama, Y. Harada, Y. Katano, T. Nakazawa, D. Yamaki and K. Noda, J. Nucl. Mater. 283-287 (2000) 302-305.

[7] K. Ochiai, H. Watanabe, T. Muroga, N. Yoshida and H. Matsui, J. Nucl. Mater. 271-272 (1999) 376-380.

4.6 Effects of Dose Rate on Microstructural Evolution in Austenitic Alloys

N. Sekimura, T. Okita, T. Sato, Y. Yang, Y. Hashimoto,
S. Jitsukawa*, Y. Sawai*, Y. Miwa* and S. Saito*
Department of Quantum Engineering and Systems Science, University of Tokyo
Department of Nuclear Energy System, JAERI*

1. Introduction

Most of high fluence data required for the irradiation testing of fusion and fission reactor materials are derived from accelerated irradiation experiments such as accelerators or test reactors with high dose rates, although some excellent experiments have recently shown strong effects of dose rate on macroscopic changes [1) 2)]. It is therefore very important to fully evaluate the effects of dose rate on microstructural evolution, and to develop models incorporating such dose rate effects in order to make predictions of the irradiation performance of structural materials.

In this study, dose rate effects on microstructural evolution are investigated in austenitic model alloys employing ion irradiation.

2. Experimental Procedure

Simple model austenitic alloy, Fe-15Cr-16Ni is prepared from high purity Fe, Cr, and Ni. by arc-melting. They are rolled to sheets of 0.2 mm in thickness. Standard 3 mm TEM disks are then punched and annealed for 30 minutes at 1050°C in a high vacuum of 10^{-5} Pa wrapped within Zr foils. Afterwards, they are mechanically and electrically polished. Irradiation proceeds with 12.0 MeV Ni^{3+} ions in the TIARA (Takasaki Ion Accelerators for Advanced Radiation Application). In this first series of irradiation, no gas atoms are pre-injected or simultaneously injected. Irradiation dose ranges from ~0.2dpa to ~20dpa, irradiation dose rate from $1.0x10^{-4}$ dpa/sec to $1.0x10^{-3}$ dpa/sec and irradiation temperature 300, 400 and 500°C. After irradiation, the specimens were electrochemically thinned to reach an observation depth, followed by back-thinning.

Analysis was conducted using a JEOL 200CX transmission electron microscope operating at 200 kV.

3. Results and Discussion

Figure 1 shows dislocation microstructures observed in Fe-15Cr-16Ni irradiated with Ni^{3+} ions. The radiation-induced microstructures are dense, especially at the lower temperatures, but rather simple, being comprised primarily of faulted dislocation loops, some unfaulted perfect loops, and a few network dislocations. At lower dose rate, the dislocation structure is mainly dominated by the faulted loops with the Burger's vector b=1/3a [111], and the density of

the faulted loops increases with dose. On the other hand, at higher temperature and higher dose, it is clearly observed that faulted loops grow large enough to become unfaulted perfect loops and decomposed into the network dislocations. These findings indicate that the dislocation evolution model should quantitatively incorporate not only the nucleation and growth of loops, but also their unfaulting and conversion to network, especially for predictions of materials irradiated for long periods.

Figure 2 shows an Arrhenius plot of dislocation loop density at 0.17 dpa. At every test temperature tested, lower dose rate enhances loop nucleation. At lower dose rates, the ratio of point defect fraction absorbed by sinks to that by recombination is higher compared to high dose rates [3], which accelerates nucleation of the dislocation loops. When the controlling process of interstitial loop nucleation is the reaction of two thermally migrating interstitials, which is applied to this model austenitic alloys with very few amounts of impurities, the nominal activation energy of the process is given by one half of the migration energy of interstitials [4]. In this experiment, the migration energy of interstitial is found to be 1.1 eV. This parameter is very important to develop models incorporating dose rate effects on microstructural evolution, especially at lower temperature ~ 300°C where the light water reactors are operated.

4. Summary

Solution-annealed model austenitic alloys are irradiated with ions to investigate the effects of dose rate on microstructural evolution. The dislocation is mainly dominated by faulted loops at the temperature between 300 and 500°C up to 2 dpa, and lowering dose rate increases the density of faulted loops. At higher dose, however, it is observed that faulted loops grow large enough to become unfaulted and form network dislocations. The interstitial migration energy is estimated to be 1.1 eV by the Arrhenius plot of the dislocation loop density.

References

1) T. Okita, N. Sekimura, F. A. Garner, L. R. Greenwood, W. G. Wolfer and Y. Isobe, the 10th International Symposium on Environmental Degradation of Materials in Nuclear Power Systems 2001, on CD-ROM with no page numbers

2) F. A. Garner, M. L. Hamilton, G. M. Bond, B. H. Sencer, T. Okita, N. Sekimura, D. L. Porter, T. R. Allen and W. G. Wolfer, to be published in J. Nucl. Mater. 2002

3) T. Okita, T. Sato, N. Sekimura and F. A. Garner, PRICM-4 2001, in press

4) N. Yoshida, Q. Xu, H. Watanabe, T. Muroga and M. Kiritani, J. Nucl. Mater. 191-194 (1992) 1114.

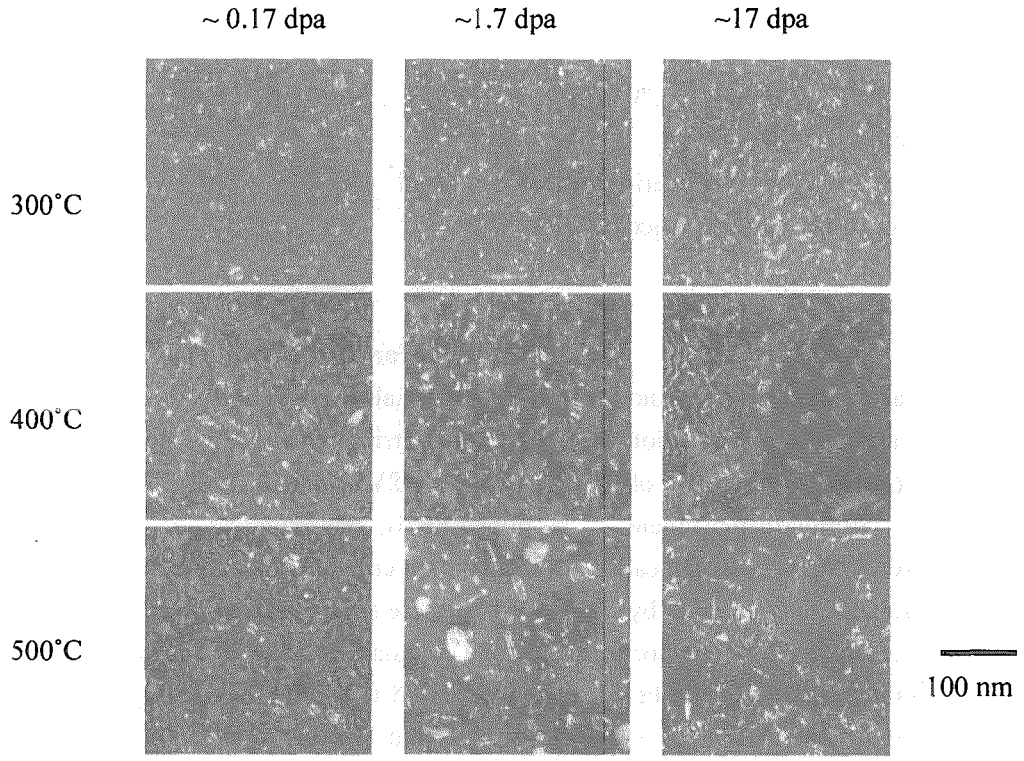

Figure 1 Dislocation microstructures in Fe-15Cr-16Ni irradiated with Ni^{3+} ions at 4.0 x 10^{-4} dpa/sec.

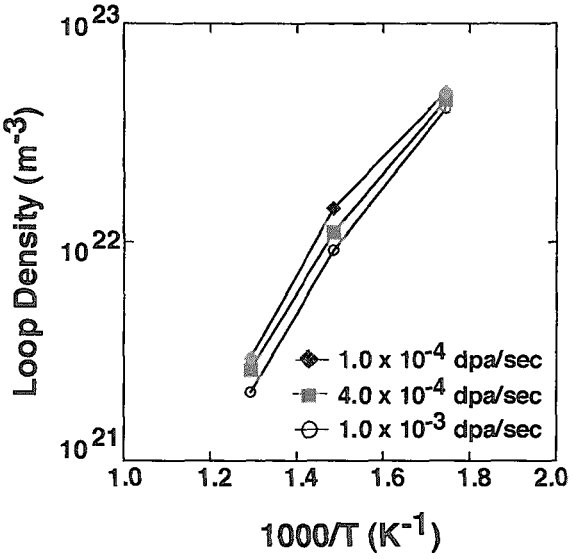

Figure 2 Arrhenius plot of dislocation loop density at 0.17 dpa.

4.7 Investigation on Irradiation-Induced Hardening of F82H Steels Irradiated by Dual/Triple Ion Beams

M. Ando[*], H. Tanigawa[*], E. Wakai[**], T. Sawai[**], A. Naito[**], and S.Jitsukawa[**]
Department of Fusion Engineering Research, JAERI[*]
Department of Materials Science, JAERI[**]

1. Introduction

One of the most critical issues in research and development of reduced activation ferritic/martensitic steels (RAFs) is the effect of irradiation-produced heavy atomic displacement damage, helium and hydrogen on mechanical properties, which are simultaneously induced by 14 MeV neutron irradiation. Irradiation hardening and embrittlement occur in RAFs, when they are neutron irradiated at lower temperatures (<623 K) [1-2], but the mechanism of irradiation-induced hardening has not been clearly understood. In addition, the effect of helium on irradiated properties is not sufficiently understood, because the helium production rate is different between fusion and fission neutron environments. Helium generation can be approximated by using mixed-spectrum neutron irradiation of ferritic steels doped with ^{10}B or ^{58}Ni. However, the mechanical evaluation of this effect is not necessarily simple. Multi-ion irradiation methods [3] provide a convenient and accurate way to simulate this condition, although the damaged volume is limited to the specimen surface. Ultra micro-indentation technique can accurately measure the irradiation-induced hardening of this small surface volume.

The purpose of this study is to investigate irradiation-induced hardening due to displacement damage in self-ion irradiated F82H steels and the effect of helium and hydrogen on hardening under dual/triple ion beams.

2.Experimental procedure

2.1 Materials and preparation

The materials used in this study were reduced activation ferritic/martensitic steels (F82H; Fe-8Cr-2W-0.2V-0.04Ta-0.1C) and 1% Ni-doped F82H. The chemical compositions and heat treatment conditions were shown in table 1. A bulk of these steels was cut into specimens of the small coupon type. The size of the specimens was $3\times6\times0.8$ mm^3 and one of the 6×0.8 mm sides was irradiated after polishing by the SiC paper up to #4000 and 0.3 μm alumina powder to an electrolytic surface finish.

2.2 Ion Irradiation

The ion-beam irradiation experiment was carried out at the TIARA facility of JAERI. The specimens were irradiated at 540-740 K by 10.5 MeV Fe^{3+}, 1.05 MeV He^+ and 380 keV H^+ ions. He implantation was performed using aluminum foil energy degrader in order to control He distribution in the depth range of about 0.5~1.3 μm from the specimen surface. The irradiation was performed to 5-20 dpa at the depth of 1.0 μm and the damage rate was about 1.0×10^{-3} dpa/s at this depth.

2.3 Micro-indentation hardness

The irradiated specimens were then indentation-tested at a load range of 10-49 mN using an UMIS-2000 (CSIRO, Australia) ultra micro-indentation testing system. The direction of indentation was chosen to be parallel to the ion beam axis, or normal to the irradiated surface.

2.4 Microstructure observation

The irradiated specimens were machined into thin films, with a Hitachi FB-2000A focused ion

beam (FIB) processing instrument with a micro-sampling system. The details of the FIB micro-sampling procedure have been explained elsewhere [4]. The thin films were made so that they included the ion-beam axis. The ion used in this process was Gallium ion accelerated to 30 keV. The microstructural examination was carried out using a JEOL JEM-2000FX transmission electron microscope (TEM) operating at 200 kV.

3. Results

3.1 Temperature dependence of irradiation hardening

Micro-indentation tests were performed on each of F82H steels at loads to penetrate about 400 nm. Figure 1 shows the temperature dependence of micro-hardness in each of F82H. Irradiation hardening was caused for all irradiated specimens. For F82H (Std), a very strong irradiation hardening by about 30% arose at irradiation temperature 620 K, while weak irradiation hardening was measured for the specimens irradiated at 740 K. This temperature dependence of irradiation hardening agreed approximately with that of micro-hardness in F82H steels irradiated at DuET Facility[5]. As a result of TEM observation, a large amount of fine dislocation loops, dot-like defects and network dislocations were observed in the ion irradiated F82H, which caused most hardening at 620 K. The major contributors to the irradiation hardening are likely to be the fine interstitial dislocation loops.

On the other hand, 1% Ni-doped F82H caused a heavy hardening over 60% at 540 K. This result is similar to irradiation behavior of 2% Ni-doped F82H in HFIR at low irradiation temperature (<573 K).

3.2 Dose dependence of irradiation hardening (under dual/triple beams)

Figure 2 shows the results of micro-indentation hardness of F82H steels irradiated up to 20 dpa at 640 K. For F82H steels (Std), hardness of dual ion beam (Damage+Helium) irradiated specimens tended to be large compared with that of single beam (self ion) irradiated specimens. This result indicated that large amount of helium atoms (>300 appmHe) enhanced the irradiation hardening. It is considered that this enhancement of irradiation hardening is attributed to the production of finer interstitial-type clusters and moreover many small helium babbles.

Similarly, 1%Ni-doped F82H caused a larger hardening than F82H (Std) at 20 dpa. Furthermore, it was considered that the irradiation hardening increased under dual/triple irradiation.

4. Conclusions

Irradiation hardening was caused for all ion-irradiated F82H specimens. Particularly, a strong irradiation hardening by about 30% was caused at irradiation temperature about 620 K. However weak irradiation hardening was measured for the specimen irradiated at 740 K.

It has been indicated that the evaluation of the synergistic effect of helium (or hydrogen) on irradiation hardening requires an irradiation dose, at least 20 dpa.

References

1) A. Hishinuma, A. Kohyama, R. L. Klueh, D. S. Gelles, W. Dietz, K. Ehrlich, J. Nucl. Mater. **258-263**(1998)193-204.

2) K. Shiba, A. Hishinuma, J. Nucl. Mater. **283-287**(2000)474-477.

3) A. Kohyama, Y. Katoh, M. Ando, K. Jimbo, Fusion Engineering and Design **51-52**(2000)789-795.

4) T. Hirose, H. Tanigawa, M. Ando, A. Kohyama, Y. Katoh and S. Jitsukawa, Materials Transactions, Vol.42 No.3 (2001) 389-392.
5) M.Ando et al., "Evaluation of Hardening Behavior of Ion Irradiated Reduced Activation Ferritic/Martensitic Steels by an Ultra-Micro-Indentation Technique", ICFRM-10.

Table 1 Chemical compositions and heat treatment conditions

	C	Cr	W	V	Ta	Mn	Si	Ni	P	Ti	S	N
F82H	0.090	7.71	1.95	0.16	0.02	0.16	0.11	-	0.002	-	0.002	0.006
1% Nidoped	0.095	7.97	1.98	0.18	0.05	0.11	0.10	0.98	0.003	0.005	0.0022	0.0025

- F82H (Std): normalized 1313Kx30min, Tempered 1023x1hr
- F82H (Over temper): normalized 1313Kx30min, Tempered 1083x1hr
- 1%Ni doped F82H: normalized 1313x30min, Tempered 1023x1hr
- Low Temperature hot rolled F82H: normalized 1223x30min, Tempered 1023x1hr

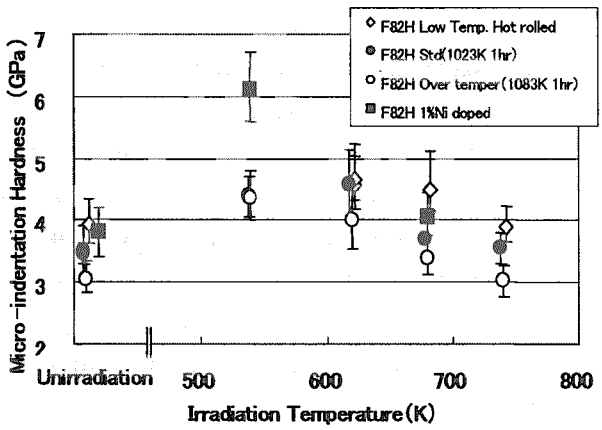

Fig. 1 Temperature dependence of irradiation hardening

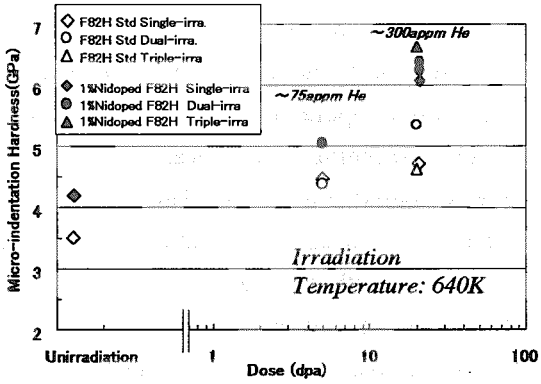

Fig. 2 Dose dependence of irradiation hardening

4.8 Effect of Triple Ion Beam Irradiation on Mechanical Properties of High Chromium Austenitic Stainless Steel

I.Ioka*, M.Futakawa*, Y.Nanjyo*, T.Suzuki* and K.Kiuchi*
Department of Nuclear Energy System, JAERI*

1. Introduction

The ultra high burnup(>100GWD/t) of LWR is considered to be an important technology for establishing nuclear power plants as one of the most promising future energy system from a view point of reducing radioactive waste and electrical cost. Cladding materials with the excellent long performance under heavy irradiation would be required to these developments. The high chromium austenitic stainless steel(25Cr-35Ni-0.2Ti UHP)[1] was selected as one of candidates that are possible to be made by the present engineering technologies. It is important to suppress environmental cracking and ductility loss on the high chromium austenitic alloy for the cladding tube. Triple ion beams were used for simulating the effect of irradiation on the mechanical properties of the candidate material. However, the ion irradiated area is limited to the very shallow surface layer (<2μm in depth) so that the irradiation damage is distributed around the thin layer. An indentation technique has been applied to examine the ion irradiation effect on the mechanical properties of the thin layer[2].

In this study, the change in apparent hardness of the very shallow surface layer of the irradiated material was calculated from the results of microindentation test. The Swift's power low constitutive of the damaged parts was derived from the microindentation test combined with an inverse analysis[3] using a finite element method (FEM). The material properties of the candidate material were compared with those of Type 304SS.

2. Experimental procedure

The chemical composition of candidate material is shown in Table 1. The tube of 11.3mm in outer diameter, 0.4mm in thickness and 1000mm in length was produced by incorporating the thermo-mechanical treatment so-called SAR (strained, aged and recrystallized)[4] from the candidate material. Type 304SS tubes which had been used to the cladding tube of the past commercial LWRs were also examined as a reference.

The irradiation condition was selected based on the condition calculated with computer simulation by assuming 100Gwd/t(MOX) on ABWRs. The dose rate, helium by (n, α) reaction and hydrogen by (n, p) reaction were simulated by the ion irradiation of 12MeV Ni^{3+}, 1.1MeV He^{+} and 380keV H^{+} at 573K corresponding to cladding surface temperature. The He^{+} and H^{+} ions were implanted in depth ranges from 1.0 to 1.5μm using energy degraders of aluminum foil. The concentration of He^{+} and H^{+} ions in the implanted range were 100-150 appmHe and 1000-1600 appmH, respectively. The dose was about 30-70dpa in the implanted range.

The microindentation test was carried out on the surface of specimens at room temperature. Two types of indenters were used for the microindentation test. One is the Berkovich indenter for measuring the apparent hardness, the other is the conical indenter that has a hemispherical apex with radius of 1.2μm for deriving the constitutive equation.

The inverse analysis was carried out using an explicit FEM code, LS-DYNA, which enables us to roughly analyze a large deformation accompanying with contacting behavior. In the analysis, the indenter and specimen were treated as axisymmetric two-dimensional bodies to take calculative efficiency into account. The modeled indenters were perfectly rigid. The mesh size is determined to be sufficiently fine to keep accuracy: the minimum element size around the apex contacting zone was 0.05μm.

The constitutive equation of the material installed into the model was assumed to be a simple power-law which is generally believed to be applicable to normal metallic materials as follows:

$$\sigma = E\varepsilon \quad \sigma \le \sigma_y \tag{1}$$

$$\sigma = A(\varepsilon_0 + \varepsilon)^n \tag{2}$$

$$\varepsilon_0 = (\sigma_y / A)^{1/n} - (\sigma_y / E) \quad \sigma > \sigma_y \tag{3}$$

where, σ is true stress, ε true strain, E Young's modulus, σ_y yield stress, A work hardening coefficient and n work hardening exponent. Hereafter, we have to identify the following material constants; σ_y, A and n through the inverse analysis on the load-depth, L-D, curve.

The flow chart of the identification with inverse analysis is illustrated in Fig. 1. Here, $\mathbf{C}$ and $\mathbf{E}$ are determinants of material constants and estimated errors of material constants. $\mathbf{Z}$ and $\mathbf{Y}$ are determinants of experimental and calculated values on L and dL/dD. $\mathbf{R}$ is determinant of error in measuring systems. S_{max} is the maximum number of steps in the divided L-D curve. $\mathbf{H}$ is $\partial\mathbf{Y}/\partial\mathbf{C}$. The procedure of the inverse analysis is as follows.

1) $\mathbf{C}_0$, $\mathbf{E}_0$, $\mathbf{R}$ and S_{max} are input as initial values.
2) $\mathbf{Z}_s$ of L and dL/dD at step S is input.
3) $\mathbf{Y}_s$ of L and dL/dD at step S is calculated by FEM code.
4) The estimated values on $\mathbf{C}$ and $\mathbf{E}$ are given by the following equation of Kalman filter using each value, $\mathbf{C}_s$, $\mathbf{E}_s$, $\mathbf{Y}_s$, $\mathbf{H}_s$ and $\mathbf{R}$ at step S,

$$\mathbf{C}_S = \mathbf{C}_{S-1} + \mathbf{E}_S\mathbf{H}_S\mathbf{R}^{-1}\left(\mathbf{Z}_S - \mathbf{Y}_S\right) \quad (4)$$

$$\mathbf{E}_S = \left(\mathbf{E}_{S-1}^{-1} + \mathbf{H}_S^{T}\mathbf{R}^{-1}\mathbf{H}_S\right)^{-1} \quad (5)$$

5) Go back to 2) and repeat the process up to S_{max}. Finally we can obtain the optimal values $\mathbf{C}_{Smax}$ estimated at final step S_{max}.

3. Results and discussion

The relationships between load and depth obtained by the microindentation test of 25Cr-35Ni-Ti UHP and Type 304SS were expressed as the L/D-D curves. The slope of L/D-D curve is in direct proportion to the appearance hardness of the material. The slope of the ion irradiated curve is higher than that of the unirradiated curve up to a depth of 0.4μm. Fig.2 shows the relative ratio of appearance hardness for the irradiated specimens normalized to that of unirradiated specimens.

Figure 3 shows the L-D curves measured using the conical indenter, and the calculated results using material constants in Eqs (1)-(3) identified according to the method with the inverse analysis on the L-D curve. The calculated L-D curves agree well with the experimental ones. The material constants estimated from the inverse analyses on the L-D curves of 25Cr-35Ni-Ti UHP and Type 304SS are summarized in Table 2. Increase in yield stress of Type 304SS was bigger than that of the 25Cr-35Ni-Ti UHP. It is well known that a hardness can be related to a yield stress. The result is in fairly good agreement with the change in apparent hardness as shown in Fig.2. The change in the value of A is the same for both specimens by ion irradiation. The value of n corresponds to the uniform deformation of the material. After ion irradiation, the decrease in n of Type 304SS was bigger than that of 25Cr-35Ni-Ti UHP. So, it seems that the ductility loss of Type 304SS by ion irradiation is larger than that of 25Cr-35Ni-Ti UHP. As a result, the irradiation hardening of the candidate is expected to be lower than that of Type 304SS from Fig.3 and the estimated material constants.

4. Conclusions

The mechanical properties of the ion irradiated material which is a candidate for ultra-high burnup fuel cladding were examined using the novel technology used for the indentation test combined with numerical calculation.

(1) The apparent hardness of Type 304SS was higher than that of the candidate after ion irradiation.
(2) The constants in the constitutive equation for the ion irradiated thin layer were determined by the inverse analyses with Kalman filter.
(3) The mechanical properties of the irradiated thin layer were deduced using the obtained constitutive equation.
(4) Increase in yield stress of Type 304SS was bigger than that of the candidate. The result is in fairly good agreement with the result of apparent hardness.

References

[1] K.Kiuchi et al., IAEA TCM, Argentina, Nov. 15-19,(1999).
[2] I.Ioka, et al., 7th Inter. Conf. on Nucl. Eng., Tokyo, Apr.19-23, ICONE-7095(1999).
[3] M.Futakawa, et al.,
[4] K.Kiuchi, et al., J. Nucl. Mater., 179-181, 481(1991).

Table 1 Chemical Composition of the Material Tested in Weight Percent (%).

Materials	Fe	C	Si	Mn	P	S	Cr	Ni	Ti	N	O	Co
25Cr-35Ni-Ti UHP	bal.	0.0013	<0.005	0.001	0.001	0.0009	24.55	34.99	0.18	0.0014	0.0011	
Type 304SS	bal.	0.063	0.49	1.45	0.016	0.012	18.72	10.27				0.03

Table 2 The material constants estimated from the inverse analyses on the L-D curves of 25Cr-35Ni-Ti UHP and Type 304SS

		σ_y, MPa	A, MPa	n
Type 304SS	Unirrad.	213	1464	0.29
	Irrad.	528	1564	0.23
	Irrad./Unirrad.	2.45	1.07	0.79
25Cr-35Ni-Ti UHP	Unirrad.	191	1397	0.36
	Irrad.	411	1492	0.33
	Irrad./Unirrad.	2.15	1.07	0.92

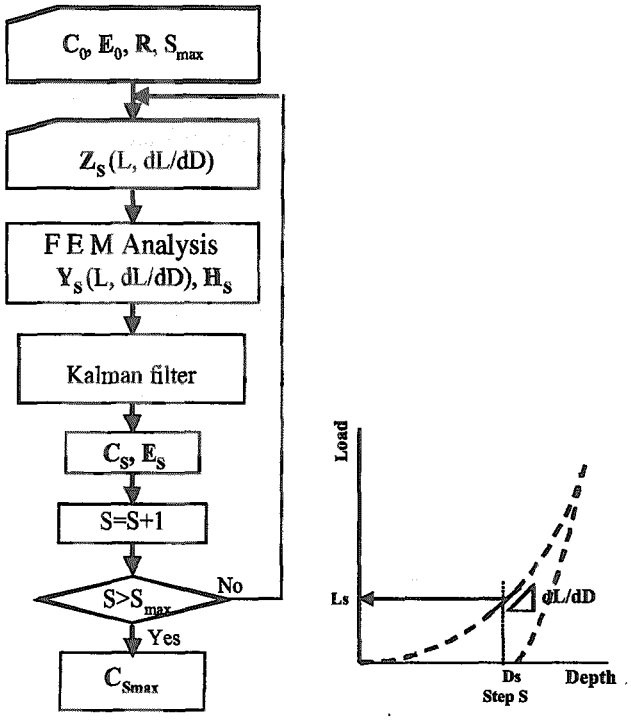

Fig.1 Flow chart for identification of material constants

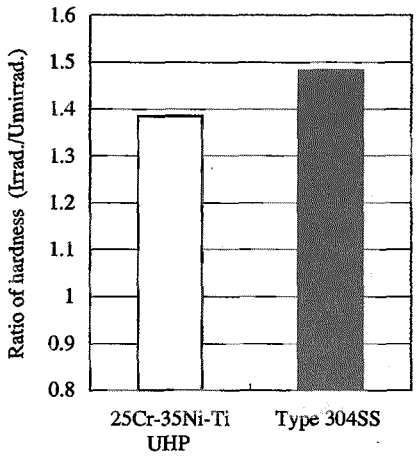

Fig.2 Relative ratio of hardness for specimens irradiated 50dpa by triple ion beams to that of unirradiated specimens

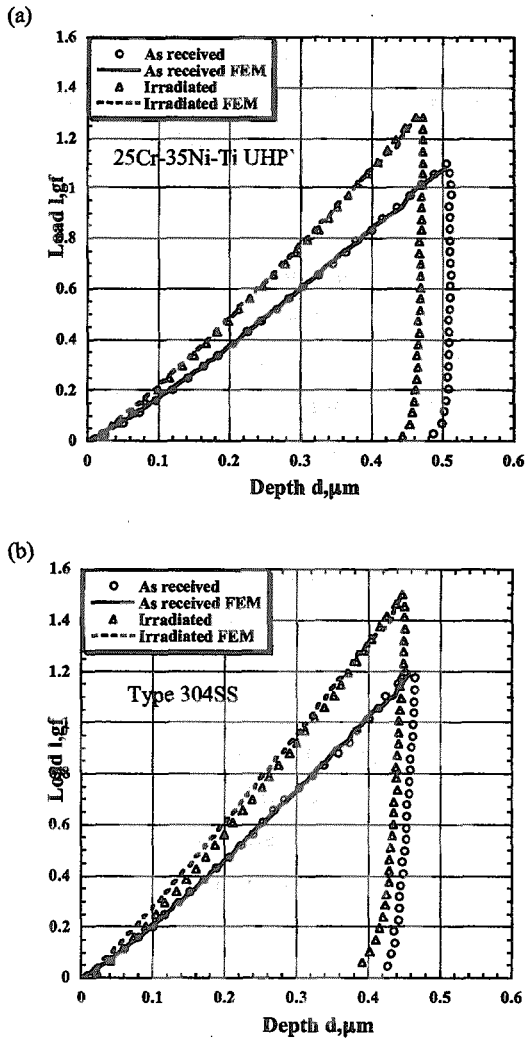

Fig.3 L-D curves measured using the conical indenter, and the calculated results by the inverse analysis

4.9 Effect of ion irradiation on mechanical property of materials contact with liquid metal

M.Futakawa*, Y. Kurata**, I. Ioka*, S, Saito**, A.Naito*, S. Hamada*, and Y. Kogawa**

Department of Nuclear Energy System, JAERI *

Center for proton accelerator facilities, JAERI **

1. Introduction

The liquid metals are expected to be used as neutron spallation targets, i.e. mercury for a high intensive neutron source [1] and lead-bismuth for accelerator-driven systems (ADSs) for transmutation of minor actinides and long-lived fission products [2]. The compatibility of the structural materials with the liquid metals is one of the crucial issues from the viewpoint of structural integrity and determination of lifetime of components under irradiation condition due to proton beam and spallation reaction. Liquid metal embrittlement, LME, is the classical problem, which many researchers have been reported so far [3,4]. The LEM occurs with combination among the kind of liquid and solid metals, temperature, imposed stress, oxygen contents, etc. and the features and mechanisms are still open questions. Lately, it has been reported that the fatigue strength of certain martensitic steel is clearly decreased in the lead-bismuth and the LME effect on the fatigue is discussed [5]. The material property at the interface between the liquid and solid metals under irradiation condition should be investigated to understand the feature of the compatibility to liquid metal and the LEM. The schematic diagram of the experiment using TIARA facility to simulate irradiation condition is illustrated in Fig.1. In this paper, the LME due to mercury against austenitic stainless steel, JPCA was examined by using the indentation technique that gives information on material properties of a small zone irradiated with ion beam and influenced by mercury immersion. In order to quantitatively evaluate the material property, the inverse analysis was applied to the load and depth curves measured by the instrumented indentation machine. The technique will be applicable to understand the localized corrosion degradation, stress corrosion cracking, radiation damage etc., from the viewpoint of micro and/or nano property changes.

2. Experimental

Specimen is a disk of 3mm in diameter with 0.2mm thickness. The electrochemically polished specimens were irradiated at a temperature of 200°C with triple ion beams; 12MeV Ni^{3+}, 750keV He^{+} and 290keV H^{+}, and dual ion beams; Ni^{3+}, He^{+} and He^{+}, H^{+}. The SRIM97 code was used to compute the implanted ion concentration and the displacement dose as a function of depth beneath the specimen surface. The displacement damage in the specimen is mainly attributed to Ni^{3+} ion implantation. The peak dose position is around 2μm. The peak positions of implanted He^{+} and H^{+} ions are controlled so that the effect of implanted Ni^{3+} ions can be neglected. At the depth of approximately 1.3μm in the specimen, the

dose is ca. 10 dpa and the He/dpa and H/dpa ratios are about 200 and 2000 appm/dpa, respectively. In case of the dual ion beam with He^+ and H^+, the amounts of implanted ions were equal to those in the triple ion beam irradiation. The irradiated specimens were immersed into the mercury of 300 cc covered by Ar gas. The temperature of the mercury was raised up to 150 ℃ and kept to be constant up to certain periods, max. 2000 h. The indentation tests were carried out before and after the irradiation and immersion tests using the indenter with a hemispherical apex with radius of 1.2 μm and Berkovich indenter.

3. Inverse analysis

Mechanical property change at the interface between liquid and solid metals was evaluated by using indentation technique. The inverse analysis was applied to the load and depth curves measured by indentation technique in order to quantitatively evaluate the constitutive equation that defines the relationship between load and deformation. The inverse analysis was carried out using the FEM model combined with Kalman filter, described in detail elsewhere [6]. The shape of the indenter is spherical because it was confirmed that the accuracy of identification of the constitutive equation using the spherical indenter is much better than that using the conventional Berkovich or Bikkers indenters. The formulation of the constitutive equation is assumed by the following Swift power low equation.

4. Results

Figure 2 shows the load/depth and depth, L/D-D curve measured by Berkovich indenter, in which the slope of the L/D-D curve is corresponding to the apparent hardness. The difference between the L/D-D curves of the as-received and 100 h immersed ones is clearly recognized: the slope of the surface layer contacting with the mercury is larger than that of substrate, although the slope of the as received specimen is almost constant independently of the depth. It means that the surface becomes harder by immersing into the mercury. The depth at which the slope changes is defined by the characteristic depth, d_c. The characteristic depth indicates the thickness of the surface layer with different properties from those of the substrate. Figure 3 shows the relationship between the characteristic depth, d_c and the immersion time, t. It is recognized that d_c increases with increasing t and the surface properties was clearly affected by the mercury immersion. In general, the depth for hardness measurement should be chosen to be less than the 1/7 thickness of the measured surface layer to avoid the influence on the hardness from the substrate [7], i.e. the thickness of the surface layer affected by the mercury immersion is 7 times larger than d_c at least. That is, the thickness influenced by mercury is thicker than 3.5 μm after 500 hr immersion.

Figure 4 shows the change of slope due to the mercury immersion and irradiation. Independently of irradiation, the hardness increases by the mercury immersion. The hardness of specimens irradiated with (Ni^{3+}, He^+, H^+) and (Ni^{3+}, He^+) is about 2 times higher than that of as-received one. It seems that H^+ ion enhances the increase of hardness due to mercury immersion. The mercury immersion and (Ni^{3+}, He^+, H^+) irradiation increase the hardness up to 2.4 time as high as

that of as received one. Figure 5 shows the evaluated nominal stress and strain curve in uniaxial tensile test by inverse analysis. Uniform elongation up to onset of necking deformation reduced to about 30 % due to the mercury immersion. This behavior seems to be associated with LME. Further studies on the effect of irradiation on LME are in progress.

References

[1] JAERI-Conf 99-003, 1999.

[2] Sasa, T., Oigawa, H., Kikuchi, K. and Ikeda,Y., Proceedings of AccApp '01, Reno, USA.

[3] Old C.F., Jour. Nucl. Mat. 92 (1980) 2-25.

[4]Gorse, D., Goryachev, S., and Auger, T., Procs. of MC02, March, 2002, Tsukuba, Japan.

[5] Kalkhof, D., private cominucation.

[6] Futakawa, M., Wakui, T., Tanabe, Y., and Ioka, I, 10th APCNDT Proceedings, Brisbane, Sept. 2001, CD-ROM.

[7] Futakawa, M., Wakui, Ioka, I., and Eto, M., Jour. Euro. Ceram. Soci. 20(2000) 1135-1143.

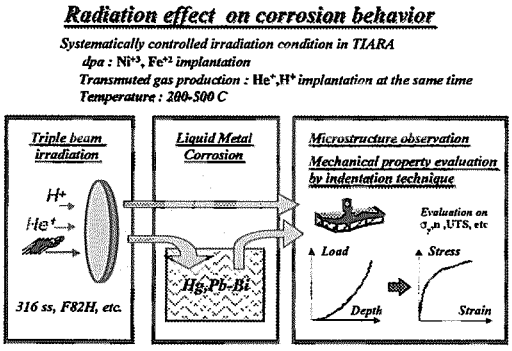

Fig.1 Schematic diagram of investigation

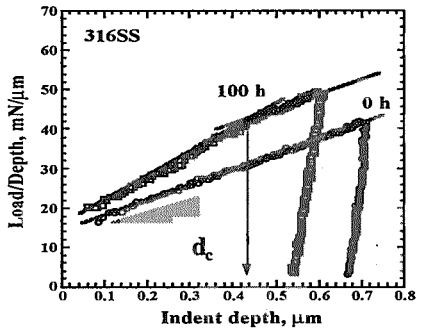

Fig. 2 L/D-D curves after 100h immersion in Hg

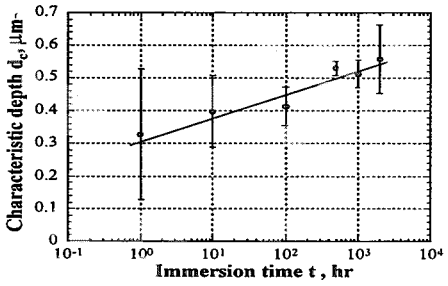

Fig. 3 Relationship between d_c and t

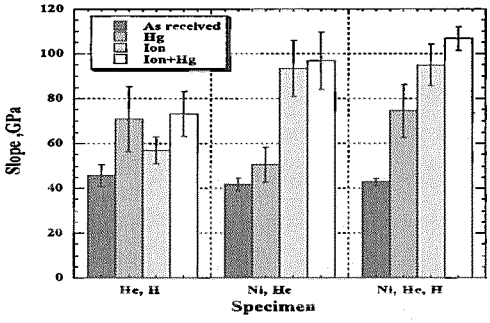

Fig. 4 Effect of irradiation and Hg immersion on hardness

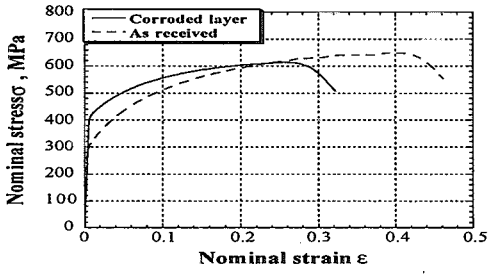

Fig. 5 Effect of Hg immersion on nominal strain and stress curve

4.10 Microstructure evolution of the advanced fuel cladding material by triple ion irradiation

Y.Nanjo*, I.Ioka*, A.Naito*, S.Kiuchi*
K.Ogura**, S.Miyamoto**, Y.Kuroda**
T.Anekawa***
Department of Nuclear Energy System, JAERI*
Japan Atomic Power Company**
Tokyo Electric Power Company***

1. Introduction

From economical and ecological viewpoints, the burnup extension more than 100GWd/t for the advanced LWRs with MOX fuel is important and effectual technology. We have been developing the advanced fuel cladding material, austenitic stainless steel, for ultra high burnup[1]. Austenitic stainless steels in nuclear power plant condition have problems of IGSCC and ductility loss. Therefore, for the advanced fuel cladding material, i.e., several countermeasures was taken adjustment of chemical compositions for getting the sufficient phase stability and corrosion resistance for Cr reduction near intergranular, purification of alloy and modification of metallographic structure for obtaining the fine grain with uniformly dispersed precipitates.

In this paper, the advanced fuel cladding material and SUS304, the fuel cladding material utilized in 'Mutsu' atomic power ship, were irradiated by triple ion beams to evaluate microstructure evolutions.

2. Experiment

2.1 Preparation of specimen

Chemical compositions of the advanced fuel cladding material and SUS304, the fuel cladding material used in Mutsu are shown in Table 1. Ultra high purity ingots of the advanced material were produced by the melting method composed with VIM (vacuum induction melting) and CCIM (cold crucible induction melting). The ingots were annealed at 1330 K for 30 minutes, and processed to the tube with 60% cold working. For the tube, the two heat treatments were taken continuously, the first is aging treatment at 823 K for 15 hours to uniformly stabilize impurities as precipitati--ons, and the second is recrystallized treatment at 1048 K for 10 hours to obtain fine grain. Finally, 7% cold working was applied to the tube for obtaining sufficient strength and straightening. The advanced material tube, 11.3mm in outer diameter and 0.4mm in thickness, was prepared by above process. SUS304 tube, 10.5mm in outer diameter and 0.4mm in thickness, was produced with the normal tube making process.

The outside of the advanced material tube was mechanically polished to obtain plane area with larger than 3mm width. The ϕ3mm disk was cut from the plane area by slurry drill, and the another side of the disk was mechanically polished. The surface for ion irradiation was buff-polished and electrochemically polished. The specimens of SUS304 tube were prepared with the

Table 1 Chemical composition of the advanced material and SUS304 of 'Mutsu'(wt%)

	Fe	Cr	Ni	Ti	C	N	O	S	Si	Mn	P
Advanced material	bal.	24.55	34.99	0.18	0.0013	0.0014	0.0011	0.0009	<0.005	0.001	0.001
SUS304 of 'Mutsu'	bal.	18.72	10.27		0.063			0.012	0.49	1.45	0.016

same process, too.

2.2 Irradiation by triple ion beams

For simulating the (n,p), (n, α) reactions and displacement damage by neutrons under 100GWd/t of ultra high burnup, the specimen was irradiated at 300℃ with triple ion beams of 12MeV Ni^{3+}, 380KeV H^+ and 1.1MeV He^+ at TIARA of JAERI Takasaki. H^+ and He^+ ions were irradiated through the energy degraders for spreading the implanted range, and were implanted to 1.0-1.5 micrometer in depth. For the calculation of the depth distribution of Ni, H, He concentration and displacement damage, TRIM(ver. 1998 code)[2] was used. Ni concentration corresponding to the matrix was less than 1.0 at% up to 1.5 micrometer depth. The disk was irradiated to 50 dpa, which is equal to the simulation result under ultra high burnup for 10 years, at 1.2-1.3 micrometer depth from the bombarded surface. H and He concentration at 1.2-1.3 micrometer depth were 30 appm/dpa and 3 appm/dpa, respectively.

After irradiation, TEM specimens were prepared by electrochemically removing surface layer to 1.2-1.3 micrometer from the bombarded side and then that surface was masked with the insulator. The specimen was thinned by electrochemic--ally polishing the unbombar--ded surface. Microstructures were examined with a JEOL 2000FX electron microscope operated at 200KeV.

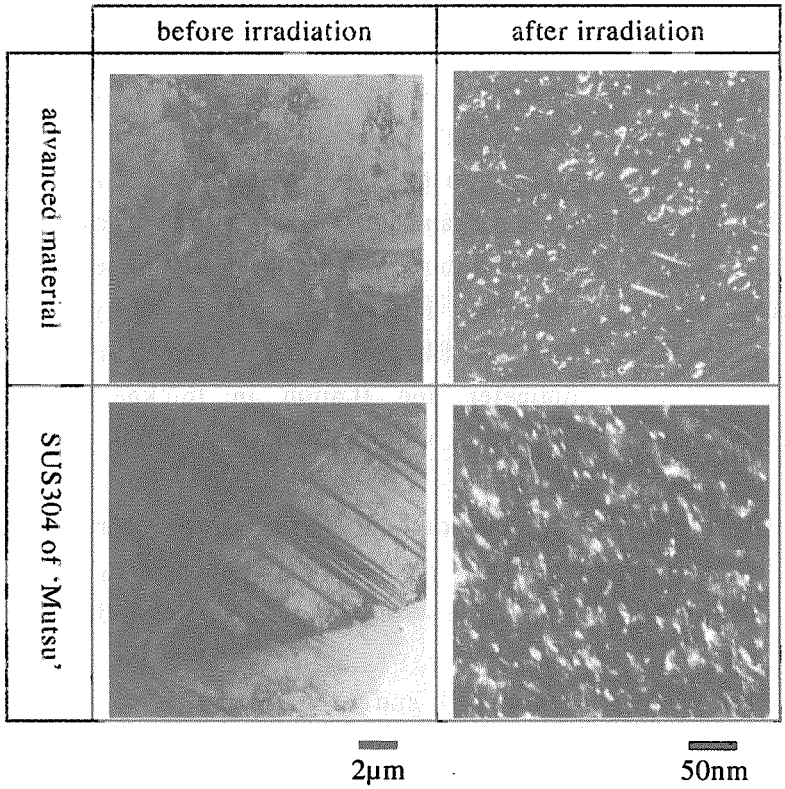

Fig.1. Microstructure evolution of the advanced material and SUS304 of 'Mutsu' before and after irradiation.

3. Result and Discussion

Fig.1 shows microstruct--ures of the advanced material and SUS304 before and after irradiation. The micrographs after irradiation observed were (110) plane in a dark field. SUS304 is almost uniform around 20 micromet--er grain, and many twin crystals exist in it. No precipitations were observed in grain and grain boundary, but stress induced ferrite is

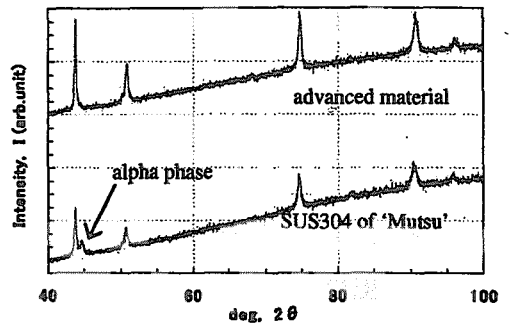

Fig.2 X-ray diffraction analysis of the advanced material and SUS304 of 'Mutsu'.

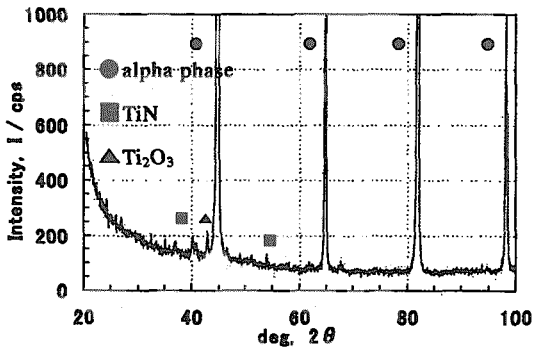

Fig.3. X-ray diffraction analysis of the residues extracted from the advanced material.

confirmed by X-ray diffraction analysis as shown in Fig.2. The advanced material has fine grains in the range of several micrometers to tens of micrometers. Precipitations are uniformly distributed in grains. Target metallography is obtained. Precipitations were extracted and evaluated by X-ray diffraction analysis. Precipitates consist of ferrite, TiN and Ti_2O_3 as shown in Fig.3.

After irradiation, dislocation loops and stacking fault tetrahedron are observed in both materials. But voids and bubbles are not observed. It is supposed that irradiation temperature of 573 K is low and ion irradiation rate is faster than that in actual condition. Fig.4 shows the number density of dislocation loop in the advanced material and SUS304, respectively. Total number of dislocation loops in the advanced material is almost equal to that of SUS304. However, peak diameter of dislocation loop of the advanced material and SUS304 are 7nm and 9nm, respectively. Loops larger than 30 nm were observed in SUS304 only. From the difference of the rate of ecological growth, the microstructural evolution of the advanced material is expected to be lower than that of SUS304.

Cr segregation around grain boundary will be evaluated in future.

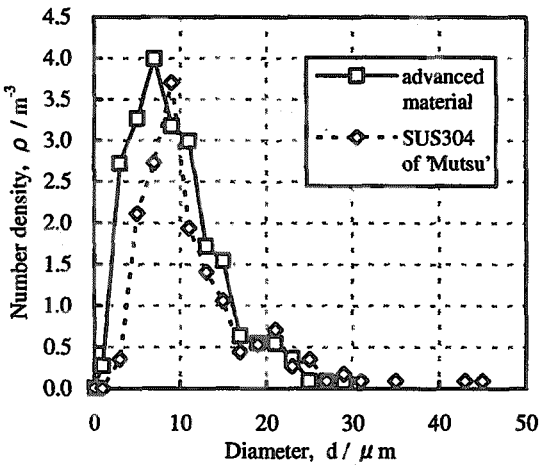

Fig.4. Number density of the dislocation loop in the advanced material and SUS304 of 'Mutsu'.

Reference

1) K.Kikushi et.al., "Development of Advanced Cladding Materials for Burnup Extension", IAEA TCM Reports on Technical and Economic Limit to Fuel Burnup Extension, Argentina, Nov 15-19 (1999)

2) J.F.Ziegler et.al., "The Stopping and Range of Ion in Solids", vol.1, Pergamon Oress, New York (1985)

4.11 Effects of irradiation on microstructure of Zircaloy-2

Susumu Yamada*, Joji Ohta*, Takeshi Sonoda**, Motoyasu Kinoshita**, Tomotsugu Sawai*** and Siro Saikawa***

Surface Science Department, Central Research Institute of Electric Power Industry (CRIEPI)*, Nuclear Energy Systems Department, CRIEPI**, Department of Materials Science, JAERI***

1. Introduction

In order to reduce costs of electric power generation by using boiling water reactors (BWRs), improvement and development of fuel cladding tubes, tolerant for long life-time (high burn-up) under severe operating conditions, are required. The Zircaloy-2 which is a zirconium-based alloy with predominant addition of Sn (about 1.5wt. %) is used for fuel cladding tubes in BWRs. The fuel cladding tubes show outstanding performance of corrosion resistance although it has been recently reported that loss of ductility occurs at high burn-up[1]. It is considered that this is due to a combination of the following effects; radiation damage introduced by neutrons, a high content of hydrogen accumulated by corrosion and a deformation caused by mechanical stress. In order to develop more tolerant advanced fuel cladding tubes, it is important to clarify each effect on the loss of ductility.

This study is focused on the irradiation-induced changes in microstructures of Zircaloy-2.

On a joint research project between CRIEPI and KTH (Royal Institute of Technology, Sweden), microstructures of Zircaloy-2 irradiated in the commercial nuclear reactor (BWR Ringhals-1, Sweden) were characterized. The fuel was irradiated in the reactor for nearly 10 years and the accumulated burn-up was 60 MWd/kgU. By comparing microstructures of Zircaloy-2 irradiated by ions with those irradiated by neutrons, better understanding of the mechanism for the loss of ductility could be possible.

2. Experiment procedure

The Zircaloy-2 fuel cladding tubes of 8×8 BWR fuel design were used in the present study. The alloys have been irradiated in the 3 MV tandem accelerator at TIARA facilities of JAERI. Irradiation was performed with 12 MeV Zr^{4+} ions at 573 K and the nominal dose was 18 dpa. For the irradiation experiment, the tube was processed into disks of 3 mm in diameter and fragments. The direction of incident ion beam was perpendicular to the cladding tube axis. Thin foils for transmission electron microscopy (TEM) observation were prepared by either electropolishing or focused ion beam (FIB) methods. Specimens for a plan view observation were prepared by the former method. The latter method was applied to prepare thin foils for cross-sectional observation. Microstructures have been characterized using TEMs (200kV JEOL 200CX and 300kV field emission TEM Hitachi HF-3000) at a Komae research laboratory of CRIEPI. Characterization of the irradiated materials with neutrons was performed using a TEM (200kV JEOL 2000EX) at KTH.

3. Result and discussion

Figure 1 shows a typical bright-field (BF) TEM image of Zircaloy-2 under ion-irradiation. A plan view observation was performed. Entangled dislocations which are visible in the matrix are thought to be formed by ion irradiation.

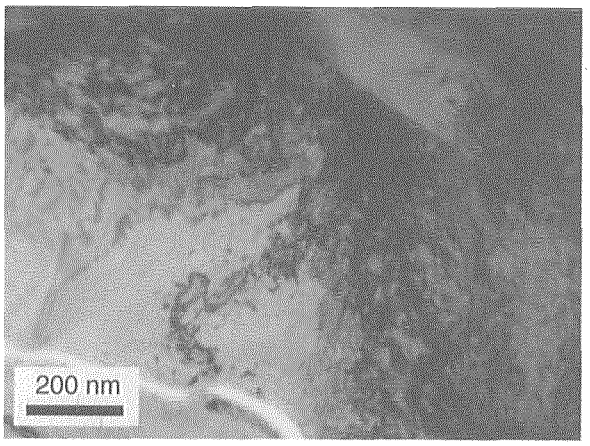

Fig. 1 Typical micrograph of Zircaloy-2 under irradiation with 12 MeV Zr^{4+} ions at 573K.

Figure 2 shows a cross-sectional BF TEM image of Zircaloy-2 under ion-irradiation. Microstructures are visible up to the depth of about 4 μm from a cladding tube surface. Dislocations such as voids and loops formed by irradiation were not observed in the matrix. From the electron diffraction study, no amorphous structures of grains and precipitates were observed.

The depth distribution of cascades has been calculated using Monte Carlo computer code, SRIM-2000. The defect depth was characterized by the center of the cascades. The SRIM calculation predicted that defects are distributed in the direction of depth and the peak of the damage is at the depth of about 2μm. Contrary to the result obtained analytically, the depth distribution of defects was not visible in the present study. On the other hand, a contrast of moiré-like fringe was observed on the whole specimen. The contrast was varied with crystallographic orientation of a grain. Similar contrast was observed in unirradiated Zircaloy-2. Therefore, it is concluded that the contrast was not formed by irradiation with Zr ions but formed by FIB irradiation. In the case of semiconductors, it has been pointed out that lattice defects and amorphous layers are formed by FIB processing. However, at the moment the influence of FIB irradiation on metals is not clear. The contrast of moiré-like fringe should occur by an overlap between planar faults formed by FIB.

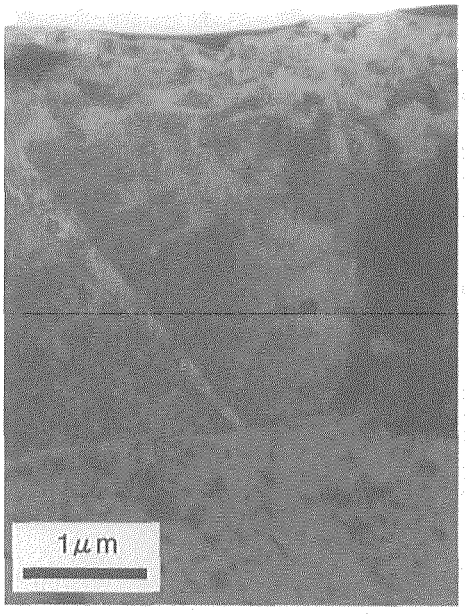

Fig. 2 TEM cross-section image of Zircaloy-2 under irradiation with 12 MeV Zr^{4+} ions at 573K.

Typical BF TEM images of Zircaloy-2 under neutron-irradiation are shown in Figs. 3. TEM specimens were prepared by electropolishing. Dislocation loops with <a>-component ($\boldsymbol{b}$ = 1/3<11-20>) lying parallel to the prism plane were observed in the matrix (Fig.3(a)). The TEM observation was performed in the direction perpendicular to the cladding tube axis. The loops were also observed in hydrides. Size of the loops was about several nms in diameter. Long

and straight <c>-component ($\boldsymbol{b}$ = 1/6<20-23>) dislocations lying parallel to the basal plane were observed in the matrix (Fig.3(b)). The TEM observation was performed in the direction parallel to the cladding tube axis. The dislocations were aligned regularly and a spacing of the lines is about 30nm. In the present observations, the microstructures irradiated with ions (Fig. 1) are not similar to those irradiated with neutrons.

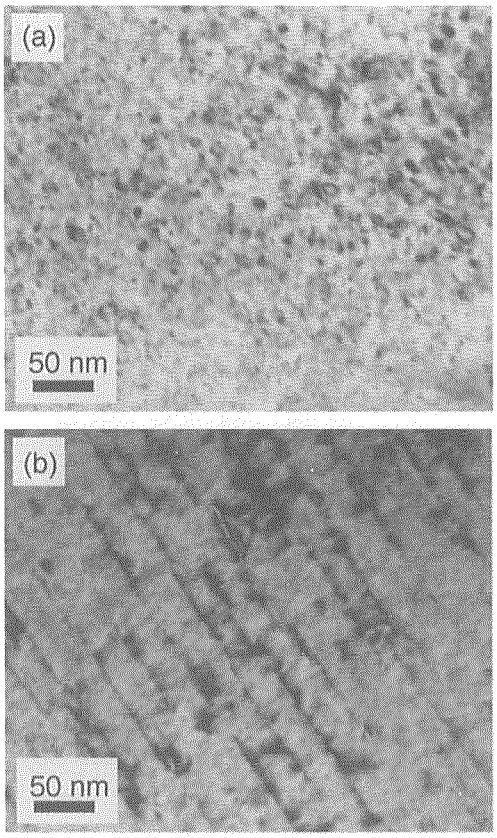

Fig. 3 TEM images of Zircaloy-2 under neutron-irradiation. In (a) <a>-component dislocation loops, and in (b) <c>-component dislocation loops.

The results are summarized as follows.

(1) Microstructures irradiated with ions are not similar to those irradiated with neutrons.

(2) It should be noted that lattice defects such as a stacking fault is formed by FIB.

(3) Dislocation loops with <a>-component and <c>-component are observed at neutron-irradiated Zircaloy-2.

References

1) Report on High Burn-up Fuel Safety Experiments, Nuclear Power Engineering Corporation, March 2002 (in Japanese).

4.12 Effects of Initial Grain Boundary Segregation on Radiation-Induced Segregation in SUS 316L Stainless Steel

F. Kano*, A. Naito** and I. Ioka**
Toshiba Corporation*
Department of Material Science, JAERI**

1. Introduction

The recent mechanistic consideration on irradiation assisted stress corrosion cracking (IASCC) has focused on the role of grain boundary (GB) segregation. The chromium (Cr) depletion at grain boundary due to irradiation is considered to be the most important factor because stress corrosion cracking susceptibility of thermally sensitized stainless steels is determined by the degree of Cr depletion at grain boundary[1]. Chromium depletion at grain boundaries in stainless steels has been regarded as a predominant cause for SCC in LWR components. The chromium depletion caused by irradiation, namely radiation induced segregation (RIS), takes place in contrast to the Cr enrichment caused by thermal processing of alloys. The behavior of molybdenum (Mo) is similar to that of Cr concerning the binding property to carbon and RIS .

We investigated the irradiation characteristic of the SUS 316L SS having initial grain boundary segregation of Cr and Mo induced by heat treatment.

2. Experimental

The specimens examined were sheets of SUS 316L (similar to Type 316L SS) stainless steel (10 mm in thickness). The chemical composition is shown in Table 1. All the specimens were heat treated at 1065℃ for 77 minutes, followed by water-cooling. Subsequently, special thermal treatment, shown in Fig.1, was carried out to enrich Cr around the grain boundary using SUS 316L rod specimens with 8mm-diameter and 12mm-length.

The 3mm-diameter TEM disks were irradiated with 12MeV Ni^{3+} ions at 573K up to 3 dpa at 1μm depth from the surface. The damage peak depth and Ni ion range peak depth were over 3μm. It is known by analysis that at 1 μm-depth the influence of nickel ion can be removed by TRIM calculation. After irradiation, surface layer of the specimen was removed by electropolishing by 1μm-depth and the specimen was back-thinned for perforation in $HClO_4$ + CH_3COOH solution.

Table 1 Chemical composition of specimen

316L	C	Si	P	S	Ni	Mn	Cr	Mo	Fe
(wt%)	0.008	0.51	0.018	0.008	12.58	0.95	16.49	2.61	bal.

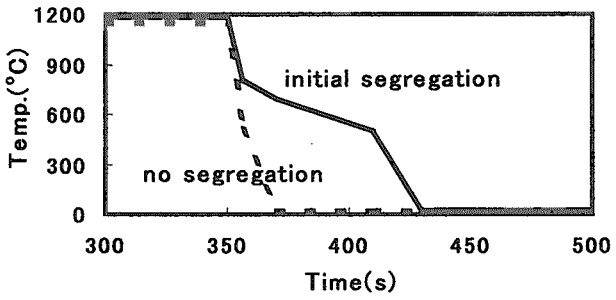

Fig.1 Heat treatment process. The solid line shows the special process that makes the initial segregation, and the dashed line shows the normal process for solution- anneal.

Microstructural observation and compositional analysis across grain boundary were conducted using a FE-TEM (TOPCON EM-002BF, 200kV) with an EDS analyzer. Beam size of the probe electron for the analysis was 0.4 nm on the specimen.

3. Results

Fig. 2 shows the compositional profiles of adequately solution– annealed 316L SS, which exhibited no segregation initially, measured by EDS across the grain boundary before and after 1.3 dpa irradiation. Fig. 3 shows compositional profiles of 316L SS, which initially have segregation around grain boundary due to special heat treatment, before and after 1.3 dpa irradiation. No precipitate was observed in grain and at grain boundary before and after irradiation in all specimens. Compositional mappings of Cr and Mo for the specimen with special heat treatment before irradiation are shown in Fig.4. A black line in the center of a STEM image shows the grain boundary, and Cr and Mo concentrated along grain boundary uniformly with 1nm width.

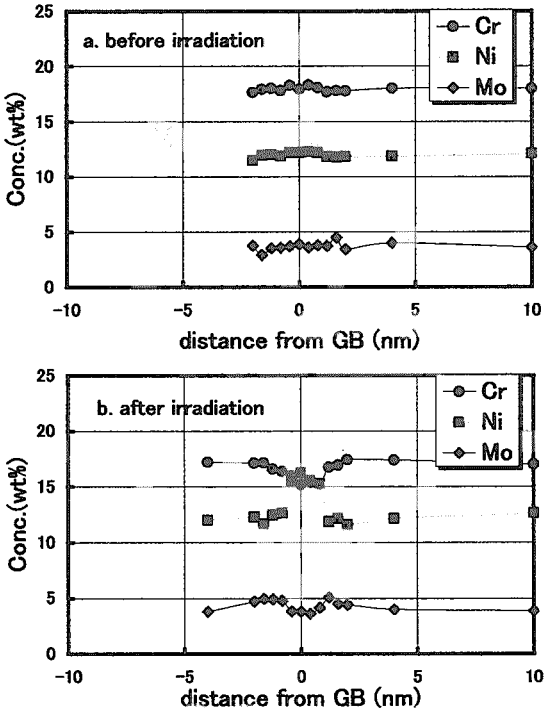

Fig.2 Grain boundary segregation of Cr, Mo and Ni in solution-annealed 316L before and after irradiation.

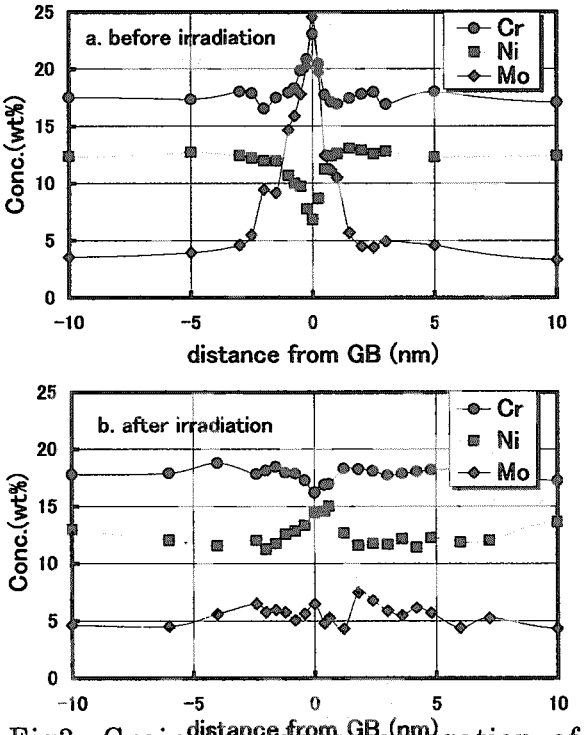

Fig3. Grain boundary segregation of Cr, Mo and Ni in specially heat treated 316L before and after irradiation.

The dependency of Cr+Mo concentration change at grain boundary on irradiation fluence is shown in Fig.5. Up to 2 dpa, Cr+Mo depletion at grain boundary is restrained. It is clear that Cr+Mo depletion rate is higher when the Cr +Mo concentration was higher at grain boundary by initial segregation.

It is suggested that there is a proper amount of initial segregation, because Cr and Mo atoms are thought to interact with irradiation-introduced point defects easily when their densities are high at grain boundary. However, SUS 316L having initial segregation of Cr and Mo by special heat treatment is useful to prevent their depletion up to 2 dpa.

4. Summary

We have succeeded in controlling initial segregation of Cr and Mo at grain boundary. SUS 316L SS having suitable initial segregation at grain boundary is expected to be useful for IASCC prevention.

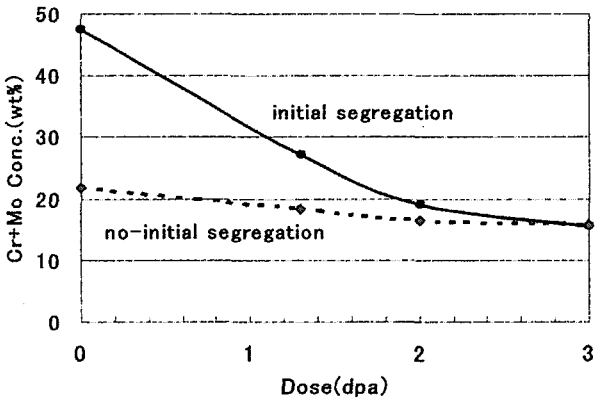

Fig.5 Cr + Mo concentrations at grain boundary in solution-annealed and specially heat treated 316L as a function of irradiation fluence.

Reference

1) S. M. Bruemmer, E. P. Simonen, P. M. Scott, P. L .Andresen, G. S. Was, J. L. Nelson, J. of Nuclear Materials 274(1999), 299-314.

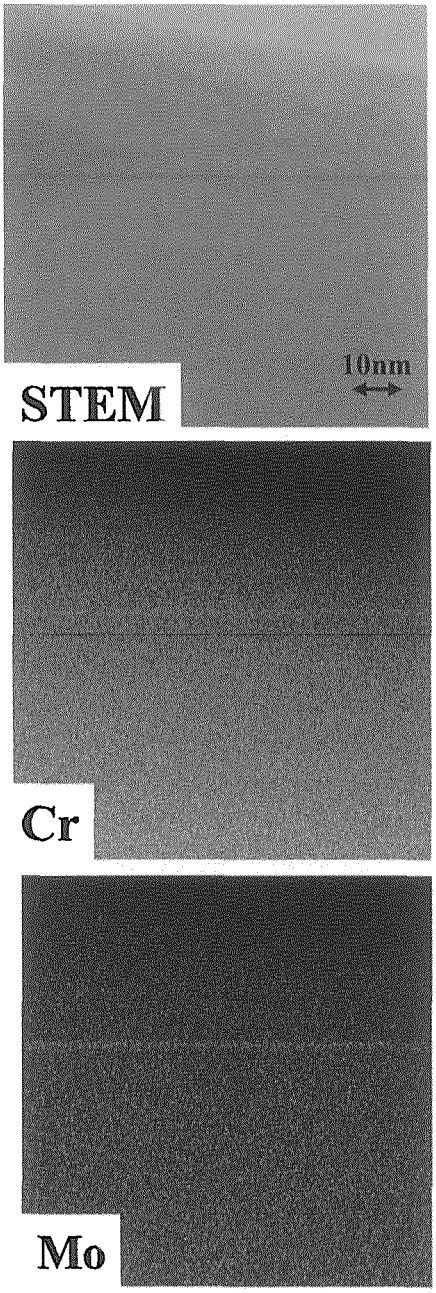

Fig.4 2-dimentional composition mapping of Cr and Mo by TEM/EDS

4.13 Effect of an electric field on the formation process of dislocation loops in He^+-irradiated α-Al_2O_3

T. Higuchi*, K. Yasuda*, K. Shiiyama*, M. Kutsuwada*, K. Tanaka*,
C. Kinoshita*, H. Abe**
Department of Applied Quantum Physics and Nuclear Engineering,
Kyushu University*
Nuclear engineering research laboratory, The University of Tokyo**

1. Introduction

α-Al_2O_3 is one of the candidate materials for insulators and radiofrequency windows in International Thermonuclear Experimental Reactor (ITER), and will be exposed to irradiation with a displacement damage rate of 10^{-10}-10^{-7} dpa/s under applied electric fields ranging from 10 to 1000 kV/m. The kinetic behavior of radiation-induced defects accompanied by the electric charge in ionic crystals such as α-Al_2O_3 is influenced by applied electric field. In spite of the importance of defect kinetics under electric fields, no investigations on the kinetic behavior of radiation-induced defects have been done.

In order to understand the kinetics of radiation-induced defects under electric fields, we have developed a device that enables one to perform irradiation at high temperatures with applied electric fields. The formation process of dislocation loops in α-Al_2O_3 under an applied electric field of 100 kV/m is shown in the present report.

2. Experimental

2.1 Development of the device

The developed device consists of an alumina insulating tube (5 mm in the outer diameter and 40 mm in length), around which Pt wire (0.5 mm in diameter) is wrapped in a heater coil. The specimen was held inside the tube by using two pieces of inner alumina insulating tubes. Electric contact was made by using vapor deposited titanium on both edges of the specimen surface. Pt ribbon (1 mm in width and 0.05 mm in thickness) was used as an electric wire. The performance of the device was confirmed by measuring the electrical conductivity of single crystals of α-Al_2O_3 : a higher insulating ability (less than 10^{-9} S/m at 800 K with 300 kV/m) was obtained with the device.

2.2 Specimens and ion-irradiation

Specimens used in the present study were single crystals of α-Al_2O_3 (Bicron Ltd.). Thin foil electron transparencies of α-Al_2O_3, whose surfaces were parallel to the $(11\bar{2}0)$ plane, were prepared from disk-shaped specimens with 3 mm in diameter and 100 μm in thickness by using dimpling and ion-thinning techniques. He^+-ion irradiation was carried out at 760 K with an acceleration voltage of 100 kV under the electric field of 100 kV/m and a fluence of 1×10^{20} He^+/m^2, which induces displacement damage of 0.5 dpa at the penetration depth of 50-200 nm. The post-irradiation microstructure was observed by a conventional TEM (JEM-2000EX) at 200 kV. Weak-beam dark-field (WBDF) technique was used to observe small defect clusters, typically 1-5 nm in size, by using g (g=0002) at the $3g$ Bragg condition.

3. Results and Discussion

Fig.1 shows WBDF images of α-Al_2O_3 irradiated with 100 keV He^+ ions at 760 K to a damage level of around 0.5 dpa with and without the electric field of 100 kV/m. These images were taken around areas corresponding to 40, 130 and 230 nm in thickness. The dot contrasts whose size is 1-4 nm are considered to be interstitial-type dislocation loops, based on the previous reports of electron and ion-irradiated α-Al_2O_3[1]. It is seen from fig.1 that the

density of dislocation loops in specimens irradiated with the electric field is low compared to that in the specimen irradiated without the electric field. Fig.2 quantifies the areal density of dislocation loops in α-Al_2O_3 as a function of specimen thickness. It reveals that the electric field suppresses the density of dislocation loops to be about 1/10 and 1/2 of that without the electric field at a thin region (40 nm) and thicker regions (>200 nm), respectively[2]. It has been also found that the electric field enhances the growth of loops. The average size of dislocation loops with the electric field is 1.2-1.4 times as large as that without the electric field. Fig.3 shows the ratio of the number of interstitials included in dislocation loops in the specimen irradiated with the electric field to that without the electric field, or f. The value of f is seen to be around 0.1 at thin regions (~50 nm) and reaches 1 around 250 nm after the monotonic increase, indicating the number of interstitials contained in dislocation loops to be small in the specimen irradiated with the electric field, especially within areas thinner than 250 nm. Most of interstitials at thinner regions are, therefore, considered to disappear at surface sinks. In conclusion, the electric field increases the surface sink strength.

4. Summary

We have developed a sample holder that enables one to perform He^+-ion irradiation at temperatures from 300 to 800 K with the maximum applied electric field of 300 kV/m. The formation process of dislocation loops has been investigated in α-Al_2O_3 with the applied electric field of 100 kV/m. The density and the size of dislocation loops in irradiated α-Al_2O_3 are found to decrease and increase respectively, and the number of interstitials contained in dislocation loops decreases with the electric field. These results lead to a conclusion that the electric field increases the strength of surface sinks.

References

[1] S.J. Zinkle and GP. Pells, J. Nucl. Mater. 253 (1998) 120-132.

[2] K. Yasuda, T. Higuchi, K. Shiiyama, C. Kinoshita, K. Tanaka and M. Kutsuwada, submitted to Philos. Mag. Lett.

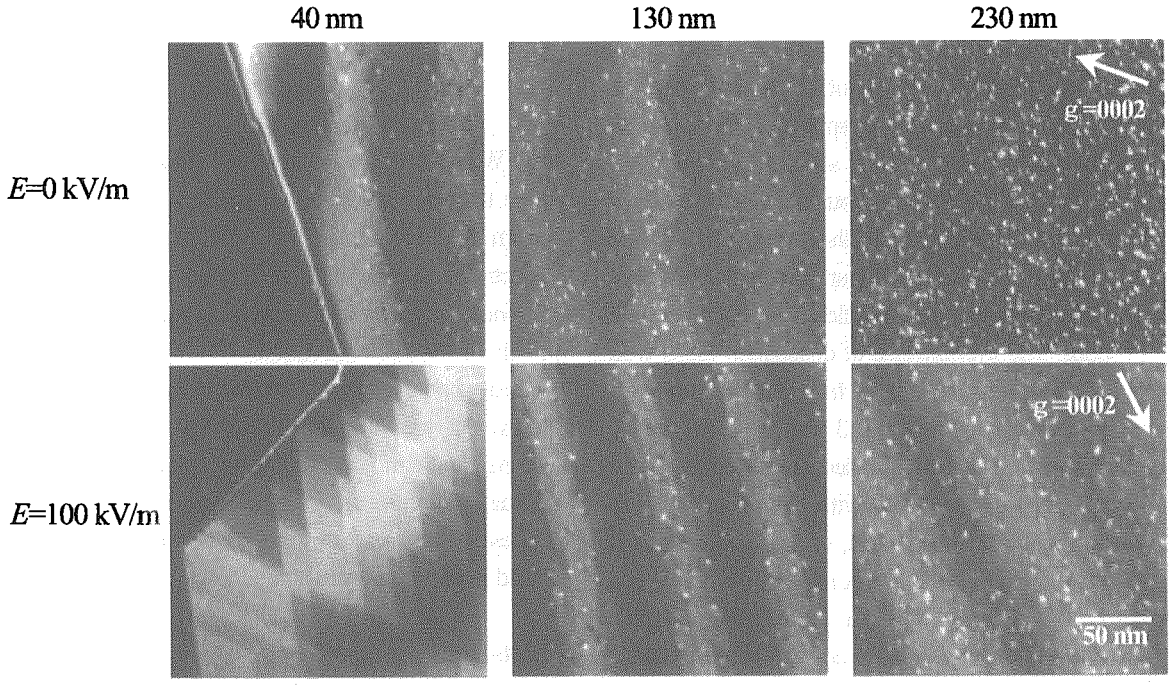

Fig.1. Weak-beam dark-field images of wedge-shaped α-Al_2O_3 specimens irradiated by He^+ ions at 760 K with and without the electric field E=100 kV/m to a fluence of 1×10^{20} He^+/m^2. The specimen thickness of observed areas are 40, 130 and 230 nm.

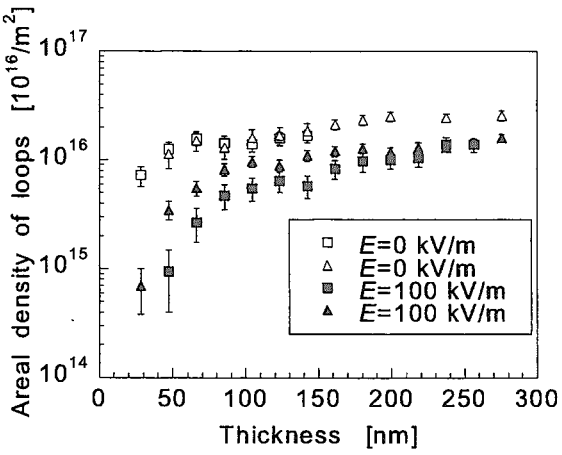

Fig.2. Thickness dependence of areal density on dislocation loops in α-Al_2O_3 irradiated with and without the electric field at 760 K to a fluence of 1×10^{20} He^+/m^2. Two data sets are shown for both specimens irradiated with and without the electric field, which were measured at different regions. No significant differences are seen in data obtained from different regions.

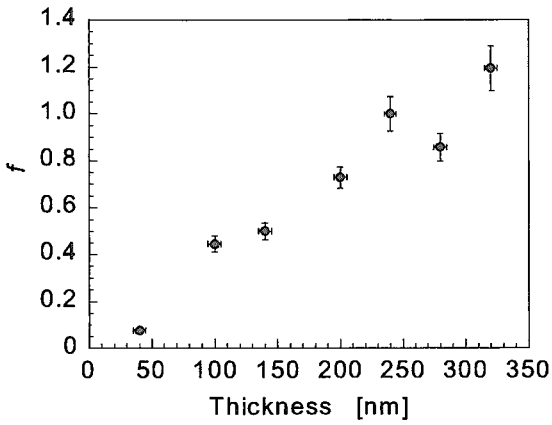

Fig.3. Ratio of the number of interstitials included in dislocation loops in α-Al_2O_3 irradiated with the electric field 100 kV/m to that without the field at 760 K, f, as a function of specimen thickness.

4.14 Photoluminescence properties of Tb implanted GaN

Yasuo Nakanishi*, Akihiro Wakahara*, Hiroshi Okada*, Akira Yoshida*,
Takeshi Ohshima** and Hisayoshi Itoh**
Department of Electrical and Electronic Engineering, Toyohashi University of Technology*, Department of Material Development, JAERI**

1. Introduction

For optoelectronic devices in a UV-visible region, GaN and related compounds are one of the attracted materials because their band-gap can be varied from 6.2 eV for AlN to 1.9 eV for InN. Recently, bright blue/green light-emitting diodes (LEDs) were successfully achieved due to the progress of crystal growth. On the other hand, it is well known that rare earth impurities in a semiconductor act as an effective luminescence center, which has very narrow line width and very small thermal quenching.[1] Some researchers reported that Tm, Er and both Eu and Pr doped into GaN indicate blue,[2] green,[3] and red[4),5] emissions, respectively.

To introduce rare earth impurities into GaN, the ion implantation is one of the useful technique to realize mono-lithic multi-color LED devices. After the ion implantation of rare earth impurities, an annealing of the sample is required to remove the implantation damage and to activate implanted rare earth impurities. However, the optimum conditions for the implantation and the annealing are not cleared. It is also not known that relations between the luminescence properties and the local structure around the rare earth impurity. In this study, we have conducted an ion implantation of Tb into GaN, and investigations were made to clarify the relation between the luminescence properties and the annealing conditions.

2. Experimental

As a host material, epitaxial GaN films was grown by atmospheric pressure metalorganic vapor phase epitaxy (MOVPE) on sapphire (0001) substrate. Properties of the GaN film used in this study are summarized in Table.I. Full width at half maximum of GaN (0002) x-ray rocking curve was about 240 arcsec.

Tb implantation was carried out in TIARA. Acceleration voltage and Tb dose were 200 keV and $1 \times 10^{14} \sim 2 \times 10^{15}$ cm^{-2}, respectively. Figure 1 shows an example of Tb profile calculated by TRIM95 simulation program. As shown in Fig.1, as a dose of 1×10^{15} cm^{-2} is assumed, a concentration peak depth of 50 nm from the sample surface and a peak concentration of 2.7×10^{20} cm^{-3} are expected.

After the implantation, to remove the implantation damage in GaN film, an annealing of the implanted sample was made in the hot-wall type electric furnace. To prevent N decomposition from GaN sample, the annealing process was carried out in mixture of nitrogen and NH_3 at atmospheric pressure. The annealing conditions are summarized in Table.II. In this study, we varied the per-

Table I: Properties of GaN epitaxial film.

growth method	MOVPE
substrate	sapphire (0001)
film thickness	2 μm
FWHM of GaN(0002) XRC	240 arcsec

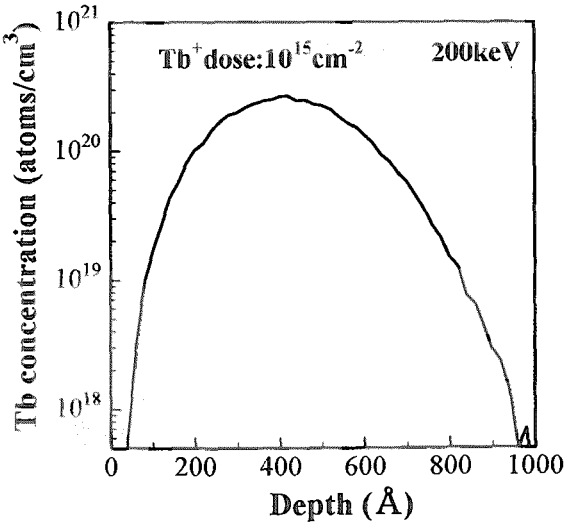

Figure 1: An example of TRIM simulation.

centage of NH_3 in the atomosphere in range of 10% to 100%. We also varied annealing time and temperatures in range of 10 min to 180 min, and 950°C to 1100°C, respectively.

Characterization of samples was made by reflection high energy electron diffraction (RHEED), atomic force microscope (AFM), differential interference contrast Nomarski, and photoluminescence (PL) measurement.

3. Results and Discussion

Figure 2 shows the surface morphology of as-implanted and the annealed samples. Surface morphology became rough as the annealing temperature or amount of Tb dose was increased. By comparing the surface morphology between before and after the annealing, it was found that the surface morphology after the annealing depends on the Tb dose. The change of surface morphology was small for the sample with Tb dose of 7×10^{14} cm^{-2} or less. On the other hand, for the sample with Tb dose of 1×10^{15} cm^{-2} or more, degradation of the surface morphology was marked.

Table II: Annealing conditions.

atmosphere	NH_3:N_2 (NH_3 10, 33, 100%)
pressure	atmospheric pressure
Temperature	950, 1000, 1050, 1100°C
Time	10, 60, 180 min

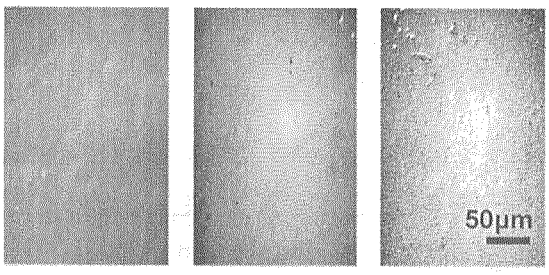

Figure 2: Surface morphology of the as-implanted and annealed samples.

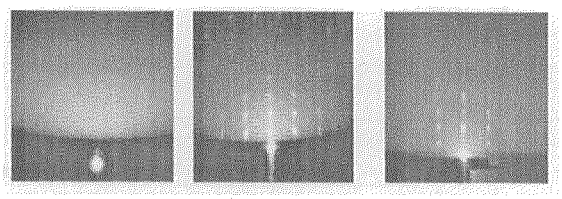

Figure 3: RHEED pattern of the as-implanted and annealed samples (Tb dose of 1×10^{15} cm^{-2}).

In Fig.3, RHEED patterns from the annealed sample at various temperatures are shown. From these RHEED patterns, it is suggested that the crystallinity can be recovered by the annealing at annealing temperature of 950°C or higher. As seen in Fig.3, the crystallinity was almost recovered by the annealing at temperature of 1050°C.

As seen in the middle of Fig.3, in the case of the higher dose of Tb, it was appeared that a ring-like RHEED pattern which seems to be caused by a formation of TbN near the surface of the sample. The formation of TbN is thought to be come from the Tb out-diffusion due to higher Tb concentration than the solid solubility limit.

Figure 4 shows PL spectra of undoped GaN and Tb doped GaN at 14K. Here, Tb doped sample was annealed at 1050°C for 60 min in nitrogen atmosphere containing 33% NH_3. Tb doped sample showed luminescence peaks at around 380nm and in 450–650 nm together with the luminescence at 360 nm which corresponds to the band edge emission.

The wavelength of the observed peak at around 380 nm agree well with emission due to the $^5D_3$

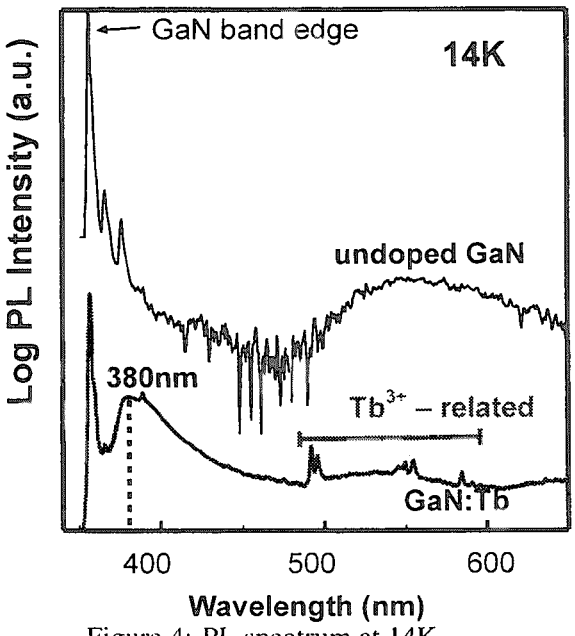

Figure 4: PL spectrum at 14K.

to $^7F_6$ transition of 4f state electron in Tb^{3+}, however, judging from their rather broad luminescence, it is difficult to say that the observed peak at around 380 nm are related to $^5D_3 \rightarrow {}^7F_6$ transition in Tb^{3+}.

On the other hand, sharp peaks in 450–600 nm can be assigned to $^5D_4 \rightarrow {}^7F_6$ (494, 496 nm), $^5D_4 \rightarrow {}^7F_5$ (545, 549, 555 nm), and $^5D_4 \rightarrow {}^7F_4$ (585 nm).

In relatively lower dose of Tb, observed luminescence at around 500 nm, which is due to the transition of 4f electron in Tb^{3+}, have increased with amount of Tb dose. As the Tb dose exceeded 2×10^{15} cm^{-2}, however, the intensity of the luminescence decreased drastically. By considering the appearance of TbN in the sample having a relatively high dose of Tb, one of the reason of the observed concentration quenching in higher dose, is that implanted Tb does not get into the GaN crystal as expected. The other reason is thought to be caused by the capturing of the excited carriers by TbN.

Next, we have investigated the annealing temperature condition. Figure 5 shows the annealing temperature dependence on the intensity of PL peaks of the near band edge (NBE) emission of GaN, the broad luminescence peak at around 380 nm, and the luminescence due to $^5D_4 \rightarrow {}^7F_6$ transition in Tb^{3+} at 492 nm. As shown in Fig.5, in the annealing temperature range of 1000–1050°C, NBE emission was increased. This suggests the improvement of the host GaN crystallinity by annealing at 1000–1050°C. With this crystallinity improvement, both of the luminescence at around 380 nm and 492 nm were also increased. However, after the annealing above 1050°C, these luminescence became weak. This might be caused by the N decomposition from GaN above 1050°C which temperature is higher than GaN growth temperature of 1000°C. Thus, from these results, the optimum annealing temperature in this study is thought to be 1050°C.

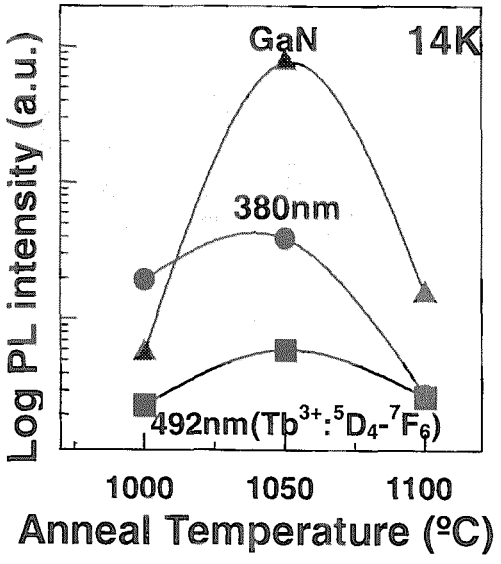

Figure 5: Annealing temperature dependence on PL intensity.

4. Conclusion

Tb has been incorporated into GaN epitaxial film by ion implantation. As increased the Tb dose, the appearance of TbN was seen. After the annealing, luminescence was observed at around 380 nm and 450–600 nm. Luminescence observed in 450–600 nm was assigned to the 4f-4f transition in Tb^{3+}. Optimum annealing temperature in this study found to be 1050°C from the temperature dependence of PL intensity.

References

1) P.N.Farannec, H.L'Haridon, M.Salvi, D.Moutonnet, and Y.L.Gulliou, Electron. Lett., 25 (1989) 718.

2) A.J.Steckl, M.Garter, D.S.Lee, J.Heikenfeld, and R.Birkhahn, Appl. Phys. Lett., 75 (1999) 2184.

3) M.Garter, J.Scofield, R.Birkhahn, and A.J.Steckl, Appl. Phys. Lett., 74 (1999) 182.

4) J.Heikenfeld, M.Garter, D.S.Lee, R.Birkhahn, and A.J.Steckl, Appl. Phys. Lett., 75 (1999) 1189.

5) L.C.Chao, A.J.Steckl, Appl. Phys. Lett., 74 (1999) 236.

4.15 Formation process and stability of radiation-induced non-equilibrium phase in silicon (III)

S. Ohnuki*, E. Shioya*, M. Takeda**, T. Suda*, S. Watanabe*, .A. Miyashita**, M. Ishino***, O.Yoda***
Dept. Mater. Sci., Fac. Engin., Hokkaido Univ. Sapporo 060-8628, Japan*
Dept. Mater. Sci. Miyagi Technical Collage, Natori 981-1239, Japan**
JAERI Takasaki, Watanuki-machi, Takasaki 370-1292, Japan***

1. Introduction

Multilayer materials with the alternation of heavy and light elements in nano-scale have been used for soft X-ray mirrors [1,2]. The main reason to the decrease in reflectivity comes from the roughness of the interface and the heterogeneity of the period [3]. An important material issue is the stability of such nano-scale structure. Compared with bulk materials, atomic diffusion in the multilayer materials can be enhanced by high-energy particle irradiation. Therefore, the stability of nano-multilayer can be studied by thermal annealing and high energy particle irradiation.

In Mo/Si system, there are three typical intermetallic compounds, i.e. of $MoSi_2$, Mo_5Si_3 and Mo_3Si, which are different in crystal structure and composition, but the phase stability under irradiation is not surveyed in nano-scale. In this study, we focused on the non-equilibrium phase formation and diffusion process in multilayer materials by using high-resolution microscopy.

2. Experimental Procedure

Multilayer samples of alternation of Mo and Si were prepared by ion beam sputtering method on Si substrates [4]. The thickness of each layer with typically less than 10 nm and the total thickness with 100nm were selected for having nominal compositions of inter-metallic compounds in Mo/Si system. TEM specimens were prepared by the conventional cross-sectional method using ion thinning. The cross-sectional observation was performed with 200 kV TEM (2000FX), and the high-resolution electron microscopy (JEM-2010F). 1 MeV Si^+ ion beam irradiation was carried out in TIARA Tandem facility Takasaki, and "in-situ" observation of microstructure was carried out in a 1250 kV HVEM (JEM-ARM 1300) with a dose rate of 1×10^{20} /cm^2/sec at room temperature.

3. Results and Discussion

3.1 Multilayer Structure

Figure 1 shows the cross-sectional structure in the specimen, Mo_3Si (100 nm/10 periods). The dark contrasts are Mo layers with thickness of 7.1nm, and the bright contrasts are Si layers with thickness of 2.2 nm. Diffraction spots of SAD show preferential orientation <110> in Mo crystal, and super lattice diffraction comes from alternation of Mo layers.

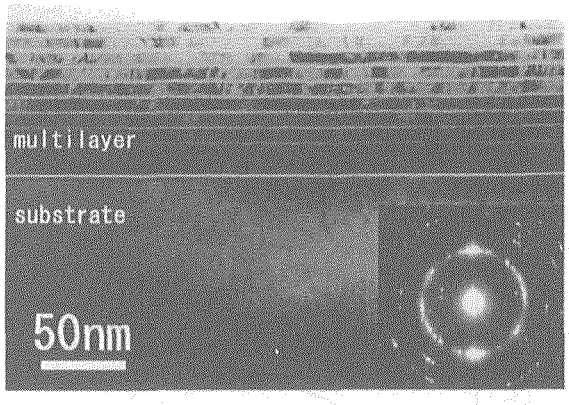

Fig. 1 Typical microstructure of multilayer materials as-deposited condition

Lattice image of Mo/Si multilayer material, where Mo layers are poly-crystalline with less than 10 nm in thickness, shows a preferential orientation of <110> direction, while Si layers are amorphous structure. It can be noted that

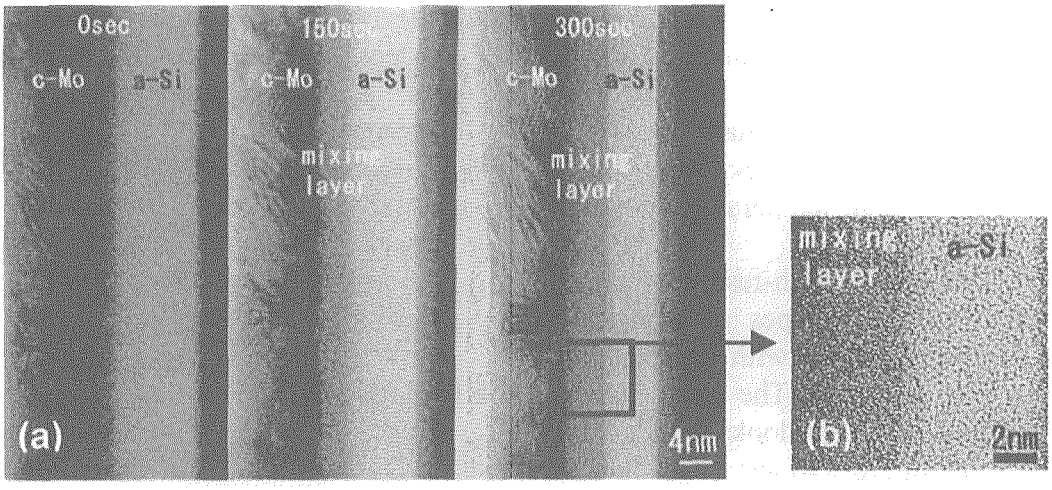

Fig.2. Amorphization process(a) and two types of amorphous stricture (b) in Mo/Si

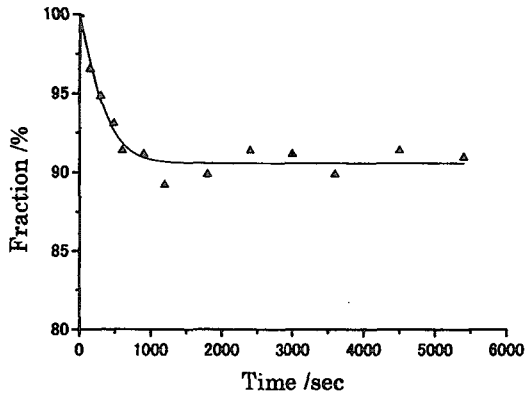

Fig. 3. Shrinkage of layer distance observed during electron irradiation.

transtion layers exist at each interface about 1 nm in thickness. The thickness of these layers differs between over and under Si layers, i.e., thicker at the Mo-on-Si than at the Si-on-Mo interface [5, 6] . Possible reason for the formation of the transition layer is physical mixing or chemical combination during the sputter deposition. The thickness of the transition layer increased with decreasing the specimen thickness.

3.2 Structure change under e-irradiation

"In-situ" high-resolution observation was performed under electron-irradiation at an ambient temperature. Figure 2 (a) shows a mixing process in multilayer sample, Mo_5Si_3, under electron irradiation. Although periodic structures were basically stable after thermal annealing up to 773 K, we observed that c-Mo layers mixed with a-Si layer, and all of the area turned to amorphous structure with homogeneous contrast after irradiation. It should be noted that the position of the layers shifted to the left side after irradiation, which means the shrinkage due to irradiation.

Figure 3 shows the shrinkage as a function of irradiation time. The shrinkage finished very quickly and the reduction rate was almost 10%. In general, amorphization may increase the volume, but covalent bonding materials are exceptional. For example, c-Si reduces the volume with several percents after amorphization. However, this reduction occurred during the mixing of a-Si and c-Mo. It seems that this phenomenon is related to

the mixing process between the larger size atom and the smaller size atom. In Ti/TiC multilayer, the value of the inter-diffusion coefficient is higher by many orders of magnitude than that expected from extrapolation of high temperature bulk data [7].

Figure 2(b) shows high-resolution image from Fig. 2(a). Two types of amorphous layers were observable; with dark contrast and with bright contrast. The mean distance of dots in the dark area looks smaller than that in the bright area, which means that the atomic density in the mixed layer should be high comparing with that in bright area of amorphous Si. Those phenomena under irradiation could be related to the atomic behavior in the system composed of heavy and light elements.

4. Conclusion

Microstructure and amorphization of Mo/Si multilayers in nano-scale were investigated by cross-sectional TEM and in-situ observation under electron-irradiation.

1. The multilayer structure was composed of c-Mo and a-Si in several nanometer levels. The transition layer of amorphous structure exists at each interface in as-deposited sample.
2. Electron-irradiation enhanced the extension of the transition layer, which is an amorphous structure with dark contrast.
3. Extreme shrinkage of 10 % was observed during irradiation, which means that this process makes an amorphous phase with high density of an ideal glass structure.

REFERENCES

[1] D. M. Solina et al.: *Thin Solid Film*, 372 (2000) 94 –103.

[2] A. M. Baranov: *Optics Communications*, 167 (1999) 23 –26.

[3] H. Takenaka, T. Kawamura: *Journal of Electron Spectroscopy and Related Phenomena*, 80 (1996) 381-384.

[4] A. Ulyanenkov et al.: *Journal of Applied Physics*, 87 (2000) 7255-7260.

[5] T. Morihashi et al.: *Applied Surface Science*, 100/101 (1996) 84 –88.

[6] B. Heidemann et al.: *Applied Surface Science*, 78 (1994) 133-140.

[7] I. Dahan et al.: *Thin Solid Film*, 377-378 (2000) 687 –693.

4.16 Effect of Cr-Ion Implantation in TiO_2: Realization of Impurity Concentration Gradients

T. Yamaki, T. Sumita, S. Yamamoto, A. Miyashita and H. Itoh
Department of Material Development, JAERI

1. Introduction

Titanium dioxide (TiO_2) has many attractive characteristics related to various technological applications. The illumination of TiO_2 with light of suitable energy, namely higher than its bandgap energy, gives rise to promotion of electrons from the valence to the conduction band, leaving positive holes in the valence band. TiO_2 is a typical n-type semiconductor especially when prepared in a reducing environment. This certainly raises the Fermi level, leading to formation of a space charge region, i.e., depletion layers in TiO_2. The resulting upward band bending of TiO_2 reduces electron-hole recombinations at the surface, thereby enhancing photochemical quantum yields. The efficiency of this so-called charge carrier separation is the major determinant in the overall photoinduced processes of TiO_2 and so such transient behavior is the most fundamental problem to be solved. We previously presented a new method to investigate carrier dynamics in the surface layer of semiconductors using a pulsed laser as an excitation source without metal contacts and an applied bias[1]. In this method, referred to as the photoinduced transient charge separation (PITCS) measurement, the behavior of the transient electron-hole pairs is followed by taking time-resolved curves of their discharges. We can estimate the number of the charged carriers which are photogenerated and then reach the surface, as a function of the irradiated photon energy. Consequently, the PITCS signal is considered to be a direct probe of charge carrier separation dynamics.

TiO_2 in itself makes use of only about 5% of the solar beams to induce photochemical reactions because of its large bandgap energy (> 3.0 eV). The effective utilization of visible light, therefore, is one of the important subjects for the increased applicability of TiO_2. To this end, transition-metal doping has been widely performed by many research groups. Wittmer et al.[2] reported that Cr doping in powdered anatase TiO_2 reduced its bandgap, depending on the dopant concentration. Among various doping techniques, ion implantation enables one to introduce dopants in a controlled manner at specific depths. Thus, it is expected that the depth profile of Cr concentrations realized by this technique can modify the band structure of TiO_2 in the direction perpendicular to the surface.

In the present study, the ion implantation and subsequent thermal treatment were performed to prepare Cr-doped TiO_2, in which impurity concentrations increased from the bulk to the surface. The PITCS measurements were then applied for the first time to examine the space charge layer modified by the impurity doping. In the Cr-doped layer with visible-light photoresponses, the separation of the electron-hole pairs was activated possibly by the resulting concentration gradient.

2. Experimental Section

TiO_2 films were deposited by pulsed laser deposition (PLD) on a (0001) α-Al_2O_3 substrate. The details regarding preparation procedures and instruments were recently reported[3]. From structural analyses by X-ray diffraction, it was found that this film was epitaxially grown in the (100) rutile phase. Ion implantations in the films were carried out at room temperature with 150 keV

Cr^+ at a nominal fluence of 5.0×10^{14} to 1.0×10^{16} ions cm^{-2}. In the experiments to check the irradiation damage and its recovery, we used <1 0 0> oriented single crystal slices of rutile for irradiation under the same conditions. All the implanted samples were annealed in air at 600 °C for 5 h. Helium ions of 2.0 MeV were generated by a 3 MV single-ended accelerator and utilized for Rutherford backscattering and channeling (RBS-C) studies. Secondary ion mass spectroscopy (SIMS) probed the Cr depth profiles in the as-implanted and subsequently annealed TiO_2 films. The basis for the PITCS method was described in our previous paper[1]. The efficiencies of the surface charge separation were measured at wavelengths of 337-520 nm using a N_2 pumped dye laser as the excitation source.

Furthermore, we prepared Cr-doped rutile films by PLD, in which Cr stripes were fixed on the rotational Ti target. The PITCS signal of these films was compared to that of the ion-implanted samples to demonstrate the effect of the in-depth impurity distribution.

3. Results and Discussion

Figure 1 shows the RBS-C results for a TiO_2 single crystal, implanted at a dose of 1.0×10^{16} ions cm^{-2} and then annealed at 600 °C for 5 h in air. The damage peaks were clearly seen in the as-implanted state. On the other hand, after the thermal treatment, the scattering yield of the aligned spectrum decreased to the level of an unimplanted sample. This indicates the complete disappearance of the displaced atoms. As a result, the pronounced recovery in the Ti and O sublattices is achieved by a recrystallization within the total thickness of the implanted region.

Figure 2 shows the SIMS Cr depth profile of the TiO_2 film annealed at 600 °C after the implantation of 5.0×10^{15} Cr^+ ions cm^{-2}, comparing the result of the as-implanted sample in the insert. Apparently, a significant amount of implanted atoms diffused thermally to the outer surface. This led to formation of a new phase where the impurity concentration increased steadily towards the surface. Such the impurity migration during the annealing was recently observed for the implanted semiconductor single crystals[4]. Based on this result, the Cr-doped TiO_2 film was prepared by PLD in such a way that it had the same impurity concentration at the top surface. The PLD method made it possible to dope the impurity homogeneously in depth. In the following, the

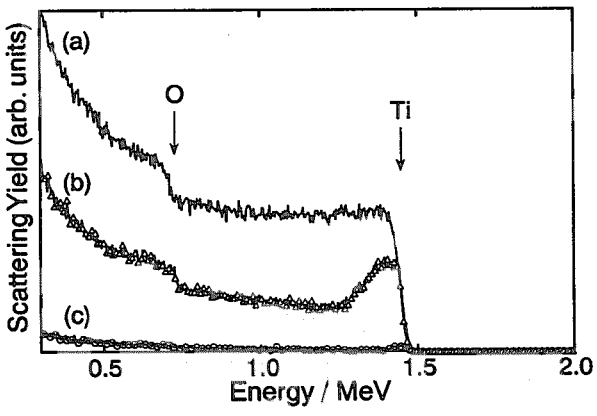

Fig. 1. 2.0 MeV $^4He^+$ random (a) and <1 0 0> aligned RBS spectra of the TiO_2 rutile single crystal implanted with 150 keV Cr^+ (1.0×10^{16} ions cm^{-2}) at room temperature (b) and subsequently annealed in air at 600 °C (c).

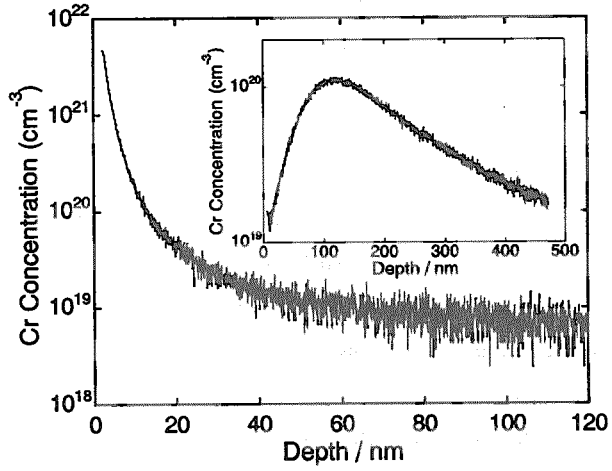

Fig. 2. SIMS Cr depth profile of the 150 keV Cr^+-implanted TiO_2 film after the annealing at 600 °C. For comparison, the result of the as-implanted sample is shown in the insert.

PITCS of this film will also be measured to clarify the relationship between the Cr depth distribution and charge separation efficiency.

The PITCS results were obtained for the Cr-doped and pure TiO_2 films to estimate their charge separation efficiencies as a function of incident-light wavelengths. The TiO_2 film showed a positive transient discharge (measured as the voltage drop). According to the polarity convention of the PITCS signal for n-type semiconductors, this means the vectorical hole transport toward the surface due to the upward band bending. Because the holes diffusing into the outermost layer without the recombination are detected, the charge separation efficiency corresponds to their proportion to the number of incident photons. This value can be calculated by fitting the discharge curve with a theoretical equation[1].

Figure 3 shows the wavelength dependence of the surface charge separation efficiency. In contrast to pure TiO_2, the Cr-doped film showed photoresponses in the visible region irrespective of the doping method. This observation was accompanied by the bandgap reduction from pure TiO_2; the bandgap energy of the homogeneously Cr-doped film was determined to be 2.52 eV by the spectral analysis. Based on the band calculations of the electronic structures of metal-doped TiO_2[5,6], we previously attributed the bandgap shift to the charge-transfer transitions between the Cr d-electrons and the TiO_2 conduction or valence band.

The major point to note here is that the efficiencies of the Cr-doped film prepared by ion implantation were much larger than those of the PLD film over the entire wavelength range and reached a maximum of 25% at 337 nm. In general, the PITCS signals are influenced by the crystalline quality and surface dopant concentration in the film. However, as stated above, the effect of these film properties should be insignificant enough to be ignored in the present discussion. It is reasonable, therefore, to consider that only the obvious difference between the two films, i.e., the depth profile of Cr concentrations determines the charge carrier dynamics responsible for the efficient separation, of course, although the possibility that such transient processes might involve some other complexities cannot be excluded. In other words, a gradient of Cr atoms whose concentration increases with decreasing depths into the surface modifies the band structure of TiO_2 to improve the property of the electron-hole pair separation. The in-depth bandgap change due to such a concentration gradient is likely to produce a favorable band bending.

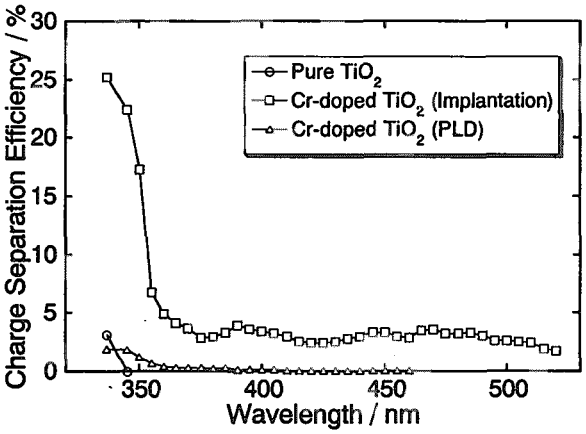

Fig. 3. Charge separation efficiency for the pure and Cr-doped rutile TiO_2 films as a function of the wavelengths of incident light.

References

1) T. Sumita, T. Yamaki, S. Yamamoto and A. Miyashita, Jpn. J. Appl. Phys. 40 (2001) 4007.
2) H. Wittmer, J. Engeldinger, R. Hempelmann, H.D. Breuer, Z. Phys. Chem. 214 (2000) 709.
3) T. Yamaki, T. Sumita, S. Yamamoto and A. Miyashita, J. Cryst. Growth 237-239 (2002) 574.
4) T. Yamaki, T. Sumita and S. Yamamoto, J. Mater. Sci. Lett. 21 (2002) 33.
5) T. Umebayashi, T. Yamaki, H. Itoh and K. Asai, J. Phys. Chem. Solids, in press.
6) T. Umebayashi, T. Yamaki, H. Itoh and K. Asai, Appl. Phys. Lett., 81 (2002) 454.

4.17 Modification of C_{60} Thin Films by 7-MeV $^{12}C^{2+}$ Ion Irradiation

Kazumasa Narumi*, Yonghua Xu*, Kiyoshi Miyashita** and Hiroshi Naramoto*
Advanced Science Research Center, JAERI*
Gunma Prefectural Industrial Technology Research Laboratory**

1. Introduction

C_{60} molecules can condense in a closed-packed crystalline form. How such a *dual* structure is damaged by ion bombardment has received considerable attention from the points of view of both basic science and application. Although many works on this subject have been reported[1-5], basic understanding does not seem to be enough yet.

In the present study, the structural changes have been investigated in C_{60} thin films on Si(111) substrates irradiated with 7-MeV $^{12}C^{2+}$ ions. Raman-spectroscopy analysis was performed for investigation of chemical state of the film due to the ion irradiation, while atomic force microscopy (AFM) was used for evaluation of surface morphology and electric conductivity.

2. Experimental

Thin films of C_{60} were prepared by molecular beam epitaxy on Si(111) substrates that were n-type and whose resistivity was less than 0.02 Ωcm. A surface oxide was removed by immersing in a 5% HF solution. Pure C_{60} powder of 99.99 % (Term USA) was loaded into a Knudsen cell in a deposition chamber whose base pressure was 2×10^{-6} Pa. During the deposition, the temperature of the substrates was 165 °C and the pressure in the chamber was lower than 5×10^{-6} Pa. The deposition rate was about 0.6 nm/min. X-ray-diffraction analysis indicated that C_{60}(111) layers in an fcc crystal grew with its <111> axis along to the <111> axis of Si. After the deposition, the specimens were set in an irradiation chamber, whose base pressure was 1×10^{-5} Pa. The specimens were then irradiated with 7-MeV $^{12}C^{2+}$ ions at room temperature with the use of the 3-MV Tandem accelerator of JAERI/Takasaki. The films were about 200 nm thick so that almost all of C ions could pass through the film. The fluence was 1.0×10^{13} to 7.3×10^{16} /cm^2. Typical current density was around 1 μA/cm^2. A part of a specimen was covered with a mask, so that each of the specimens had an *unirradiated* area. AFM analysis of the films was performed in air using JEOL JSPM-4200 after the irradiation: Surface morphology and electric conductivity of the films were evaluated simultaneously using the contact mode AFM with an Au-coated Si cantilever. Raman-spectroscopy analysis was performed in air with Nanofinder (Tokyo Instruments, Inc.), where the 488 nm spectral line of an Ar^+ laser was used to excite the specimen and the power of the laser was about 0.5 mW.

3. Results and Discussion

Figure 1 shows fluence dependence of Raman spectra of C_{60} films on Si(111) irradiated with 7-MeV $^{12}C^{2+}$ ions. It can be seen easily that the intensity of the two lines of A_g mode is decreasing with the increasing fluence, and finally the spectral features for the C_{60} molecule are hardly observed at the highest fluence. On the other hand, a broad and asymmetric line between 1000 and 1700 cm^{-1}, characteristic for all forms of amorphous carbon, appears and it is prominent at the fluence of 1.0×10^{16} /cm^2, where spectral features for the C_{60} molecule are still recognized slightly. Graphitization is not observed even at the highest fluence. The result indicates that the collision with the energetic ion

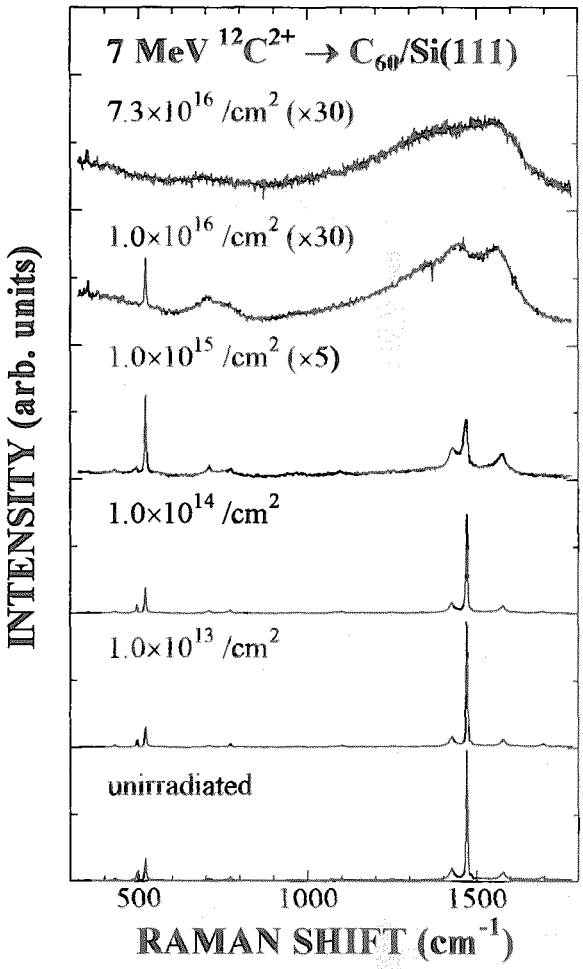

Fig. 1 Fluence dependence of Raman spectra of C_{60} films on Si(111) for the irradiation of 7-MeV $^{12}C^{2+}$ ions.

decomposes the C_{60} molecule, which transforms C_{60} films into a form of amorphous carbon. It should be noted that no new peak or peak shift is observed in the present ion irradiation: The fact indicates no intermediate fragments of a C_{60} molecule generated by ion impact.

At the dose of 1.0×10^{15} /cm^2, we observed the broadening of the line of $A_g(2)$, the "pentagonal pinch" mode. The previous works reported that the broadening of the line at the "pentagonal pinch" mode due to the appearance of a shoulder at a lower frequency was observed, and concluded that the result indicated the polymerization of the C_{60} film[3, 4]. The line broadening observed in the present study can also be attributed to the polymerization; in fact, the Voight-line-fit analysis reveals that the broadening of the line is due to peaks at frequencies lower than 1469 cm^{-1} where the line of $A_g(2)$ for pristine C_{60} is observed[6].

Figure 2 shows typical results of the AFM analysis of the C_{60} film, where topographic and current images were measured simultaneously. The results of an unirradiated film are shown in Fig. 2(a): The current image was measured with sample-biased voltage of +1.0 V and the current scale is shown on a logarithmic scale on the right-hand side of the image. The detected current was several tens pA that was the same order as the dark current of our AFM system. The result indicates that the pristine film is almost insulating. For the films irradiated with 7-MeV $^{12}C^{2+}$ ions at low fluences, the same results were obtained. Detectable current was observed for the film irradiated with 7-MeV $^{12}C^{2+}$ ions up to the fluence of 1.1×10^{16} /cm^2 as shown in Fig. 2(b), where the sample-biased voltage was +1.0 V. As shown in the current scale, a brighter area is more conductive, while current detected in a dark area is the same order as the dark current. This change of the electric conductivity by the ion irradiation agrees with the fluence dependence of the Raman spectra; the observed Raman spectrum shows the decomposition of the C_{60} molecule and the amorphization. Thus it is interpreted that the observed change of the electric conductivity is attributed to the appearance of conductive carbon species associated with the dissociation of the C_{60} molecule through the collisions with energetic ions.

References

1) R. G. Musket, R. A. Hawley-Fedder and W. L. Bell, Radiat. Eff. Defects 118 (1991) 225.
2) R. Kalish, A. Samoiloff, A. Hoffman, C. Uzan-Saguy, D. McCulloch and S. Prawer, Phys. Rev. B 48 (1993) 18235.
3) J. Kastner, H. Kuzmany and L. Palmetshofer,

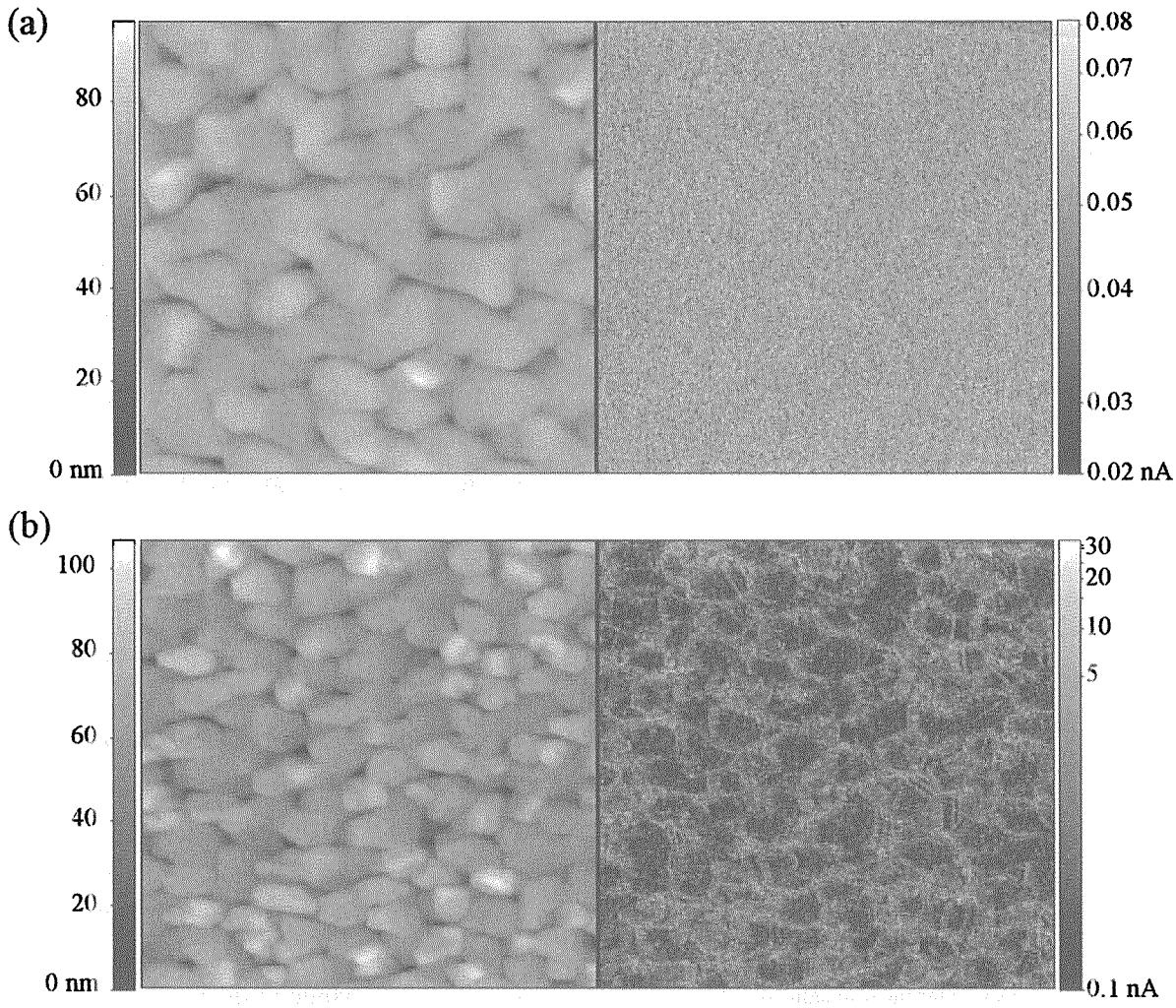

Fig. 2 Topographic (left) and current (right) images measured simultaneously with the AFM; (a) the unirradiated C_{60} thin film and (b) the film irradiated with 7-MeV $^{12}C^{2+}$ ions up to the fluence of 1.1×10^{16} /cm^2. The scanned area is 3×3 μm^2. In the current image, a brighter area indicates that the film is more conductive. Take notice of the current scale of (a) that is different from that of (b).

Appl. Phys. Lett. 65 (1994) 543.

4) S. Prawer, K. W. Nugent, S. Biggs, D. G. McCulloch, W. H. Leong, A. Hoffman and R. Kalish, Phys. Rev. B 52 (1995) 841.

5) D. Fink, R. Klett, P. Szimkoviak, J. Kastner, L. Palmetshofer, L. T. Chadderton, L. Wang and H. Kuzmany, Nucl. Instrum. Methods B 108 (1996) 114.

6) A. M. Rao, P. Zhou, K. -A. Wang, G. T. Hager, J. M. Holden, Y. Wang, W. -T. Lee, X. -X. Bi, P. C. Eklund, D. S. Cornett, M. A. Duncan and I. J. Amster, Science **259** (1993) 955.

4.18 Investigation of the resonant vibration modes of self interstitial atoms in hcp metals by low temperature specific heat measurement

M.Watanabe
Department of Materials Science, JAERI

1.Introduction

Some theories[1] predict the resonant vibration modes due to self interstitial atoms in metals, which have large amplitudes and low frequencies. These kinds of modes for a single defect present an important problem for physics of lattice defect. The resonant vibration modes have an important influence on properties of phonons. To verify the existence of these modes, we measured the specific heat of electron-irradiated hcp metals(Zn) at low temperatures.

2.Experimental

The specimens used in this work were Zn single crystals with dimensions of $11.5^{\Phi} \times 0.5$ mm^3. The irradiations with 2-MeV electrons to the dose of 1.55×10^{18}/cm^2 at 25K were performed by using a low temperature irradiation facility interfaced to TIARA 3MV single-ended accelerator. Before and after irradiation, we measured the specific heat of the specimen under the adiabatic condition between 5K-45K.

3.Results and discussion

Fig.1 shows the specific heat change in Zn<0001> after irradiation to the dose of 1.55×10^{18}/cm^2 at 25K. Fig.2 and Fig.3 show the specific heat change after 60K annealing and after 300K annealing in Zn<0001> irradiated to the dose of 1.55×10^{18}/cm^2 at 25K respectively. Fig.4 shows the specific heat change in Cu(fcc metals) after irradiation to the dose of 7.73×10^{17}/cm^2 at 19K and subsequent 60K annealing[2]. Fig.5 and Fig.6 show the specific heat change after irradiation and after 300K annealing in Mo(bcc metals) irradiated to the dose of 6.49×10^{17}/cm^2 at 23K respectively[2].

In fcc metals(Cu) and bcc metals(Mo), the peak of the specific heat change which originates in the resonance vibration modes below 20K was found out, as shown in Fig.4, Fig.5 and Fig.6. This temperature range is lower than the 1st stage of the recovery observed by electrical resistance measurement etc.

In the verification experiment of Zn, the peak of the specific heat change which originates in the resonance vibration modes below 20K was found out like Cu and Mo. The specific heat change resulting from the resonance vibration modes of Zn was small after irradiation and was large after 300K annealing. This means that the resonance vibration modes after 300K annealing became large.

4.Summary

In the verification experiment of Zn(hcp metals), the peak of the specific heat change which originates in resonance vibration modes below 20K was found out like Cu(fcc metals) and Mo(bcc metals).

Reference

1) A.Scholz and Chr.Lehmann, Phys.Rev. B6(1972)813.
2) M.Watanabe, TIARA Annual Report 2000, p144 (2001)

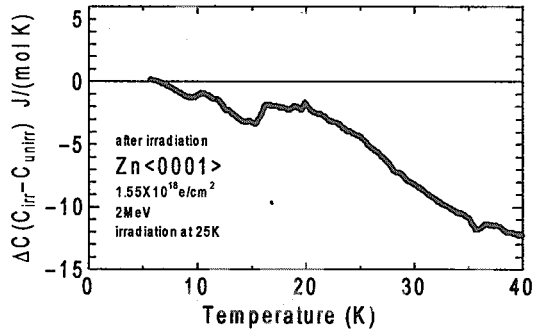

Fig.1. Specific heat change in Zn<0001> after irradiation to the dose of 1.55×10^{18}e/cm^2 at 25K.

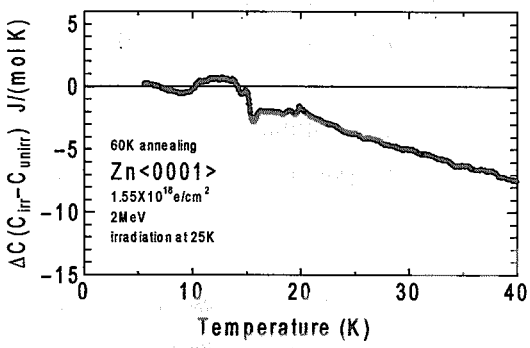

Fig.2. Specific heat change after 60 K annealing in Zn<0001> irradiation to the dose of 1.55×10^{18}e/cm^2 at 25K.

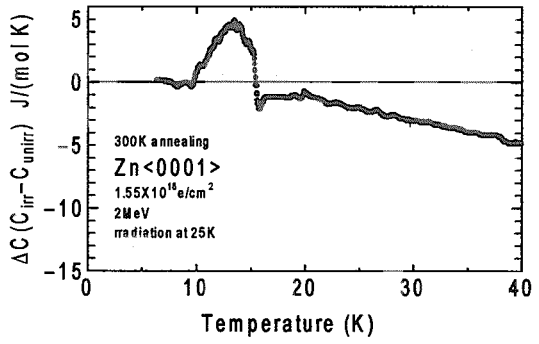

Fig.3. Specific heat change after 300 K annealing in Zn<0001> irradiation to the dose of 1.55×10^{18}e/cm^2 at 25K.

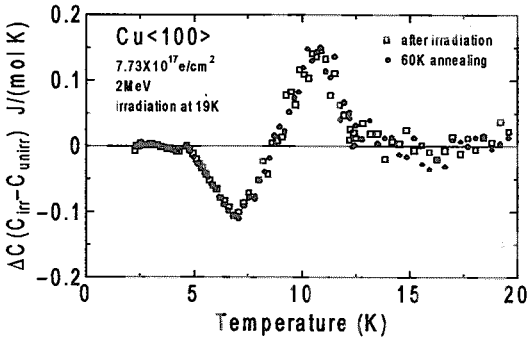

Fig.4. Specific heat change in Cu<100> after irradiation to the dose of 7.73×10^{17}e/cm^2 at 19K and 60K annealing

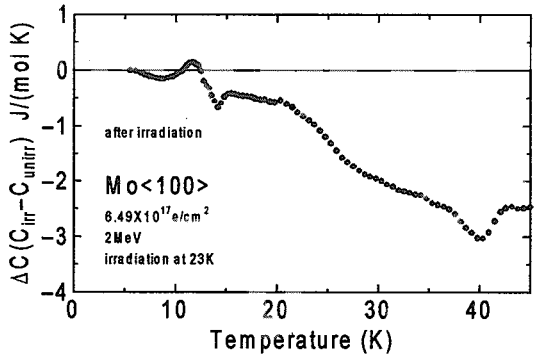

Fig.5. Specific heat change in Mo<100> after irradiation to the dose of 6.49×10^{17}e/cm^2 at 23K.

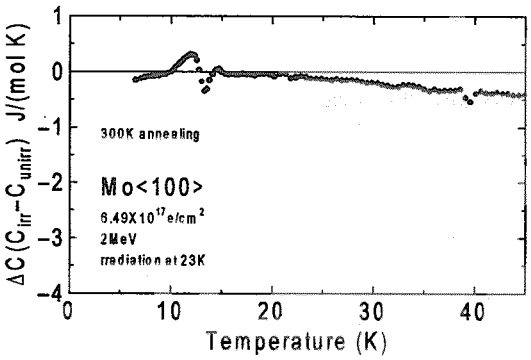

Fig.6. Specific heat change after 300 K annealing in Mo<100> irradiation to the dose of 6.49×10^{17}e/cm^2 at 23K.

4.19 Hydrogen migration in electron irradiated Pd-based alloys

K. Yamakawa*, Y Chimi** A. Iwase**, T. Yano*, N. Ishikawa**
Department of Electric and Electronic Engineering,
Faculty of Engineering, Ehime University*,
Department of Materials Science, JAERI**

1. Introduction

In the previous papers, the diffusivities of hydrogen isotopes in Pd and Pd based alloys at low temperatures have been obtained by measuring the electrical resistivity increase due to the ordering of hydrogen isotopes around 50K [1-6]. In these experiments the disordered hydrogen atoms were produced by quenching the specimen into liquid helium from the temperature at which the hydrogen atoms are structurally in disordered state and the resistivity measurements were done in liquid helium during the annealing.

Vajda et al.[7] obtained smaller activation energies (about halves of ours), for hydrogen isotopes in both fast cooled and/or electron irradiated Pd-H(D) alloys, comparing with our results of quenched cases.

In the present experiment, to clarify the cause of the disagreement between our results and their results, the disordered hydrogen atoms have been produced by electron irradiation and the specimens have been annealed at a constant heating rate and the resistance has been measured at the same temperature as that they have measured. The resistance change has been analyzed by the cross-cut method without using the value of the order of reaction and the assumptions used by Vajda et al.

2. Experimental Procedures

The Pd based alloy specimens (Pd-1at. %Fe-H and Pd-1at. %Ag-H) were prepared and hydrogen-charged by the similar method as shown in the previous papers [3,4]. Before each electron irradiation, the specimens were slowly cooled down, from around 80K, at a constant rate of 0.5K/min below 15K to obtain the structurally ordered state of hydrogen atoms. Then the specimens were irradiated with 0.5 MeV electrons from single ended accelerator in TIARA branch of JAERI.

The energy of electrons was selected as 0.5 MeV to prevent from producing the defects in Pd lattice. The total fluence of each irradiation was ~ 5 x 10^{20}e/m^2. The temperatures of the specimens during the irradiation were below 15K. After the irradiations the specimens were heated-up to higher temperatures at various rates and the electrical resistance of the specimens was measured in situ at the temperatures. The constant heating rates used in the present experiment were between 0.057K/min and 1.85K /min.

3. Experimental Results and Discussion

It has been already clarified by previous investigations [3-11] that the electrical resistivity of Pd alloys increases by ordering of hydrogen isotopes and decreases by disordering of the isotopes. In the present experiment, the resistance of the Pd based alloys decreases due to hydrogen disordering by the electron irradiation and increases due to hydrogen ordering by the annealing. Typical resistance curve of the electron irradiated specimen(Pd-1at.%Ag) during heating-up is shown in Fig. 1 together with a heating-up curve for the same specimen after the

slow cooling for the same heating-up rate, 0.057 K/min. The difference between the curves in Fig.1 shows the recovery of resistance due to hydrogen disordered by the irradiation. A group of normalized recovery curves for the irradiation are shown in Fig.2 for various heating rates. The recovery curves show clear sub-stage at lower temperature range comparing with the recovery curves for fast cooled case in which the curves show one stage (Fig.3). The migration energy of hydrogen in this temperature range is obtained by cross cut method at various recovery levels for these recovery curves. The obtained results are shown in Fig.4 for each level of the recovery in Fig.2 in electron irradiated case. The rates in the figure near the lines show the level of the recovery in Fig.2. The slope of the line shows the activation energy of hydrogen migration at each recovery level. These activation energies are shown in Fig.5 for various levels of the recovery in the electron irradiated case and fast cooled case for Pd-1at %Fe and Pd-1at, %Ag alloys. The activation energy at low temperature stage for the irradiated Pd-1at. %Fe is lower by about 15meV than that for the fast cooled case. On the other hand, the activation energy at low temperature stage for Pd-1at. %Ag is similar to the value for the fast cooled case. For high temperature stage of both alloys, the energy is lower than that for the fast cooled case, in this analysis. These results show that hydrogen disordering by electron irradiation causes two different hydrogen configurations. The value of the activation energy in the irradiated case in pure Pd and Pd alloys shows similar behavior with the results in the case where the specimen were quenched into liquid helium. In case of using this experimental method which is similar to that used by Vajda et al., the activation energy of hydrogen migration in Pd based alloys shows the same value as that in our quenched cases [5-6].

References

1) K. Yamakawa and H. Maeta, Scripta Met. Mater. 25, 1129(1991).
2) K, Yamakawa and H. Maeta, Defect Diffu. Forum 95-98, 311 (1993),
3) H. Maeta and K. Yamakawa, Defect Diffu. Forum 95-98, 305(1993),
4) K. Yamakawa and H. Maeta, Scripta Met. Mater. 32, 967(1995).
5) K. Yamakawa and H. Maeta, Scripta Met, Mater. 29, 1577(1993).
6) K. Yamakawa and H. Maeta, Scripta Met, Mater. 29,411 (1993).
7) P. Vajda, J.P. Burger, J.N. Daou and A. Lucasson, Phys. Rev. B33, 2286(1986).
8) O . Blaschko , P . Fratzl and R. Klemencic, Phys. Rev. B24, 277(1981).
9) S.J. Kennedey, E. Wu, E.H. Kisi, E.M. Gray and B. J. Kennedy, J. phys.: Condens. Matter 7, L33(1995).
10) T.E. Ellis, C.B. Satterthwaite, M.H. Mueller and T.O. Brun, Phys. Rev. Lett. 42,456(1979).
11) B.M. Geerken, H. Hemmes and R. Griessen, J. Phys. F14, 813(1984).

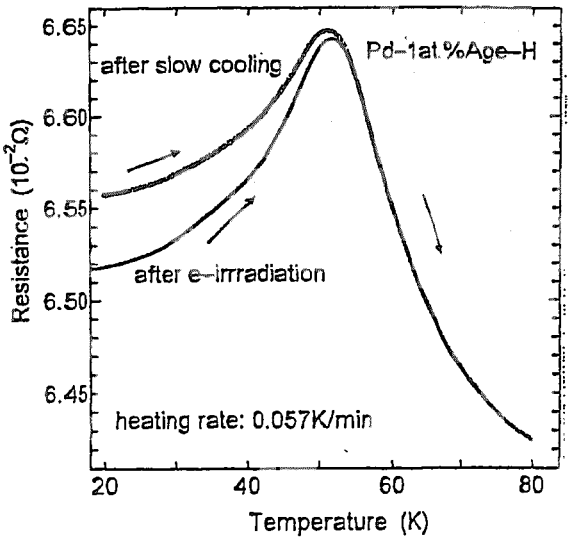

Fig.1 Electrical resistance curves during heating at 0.057 K/min after electron irradiation and slow cooling, respectively.

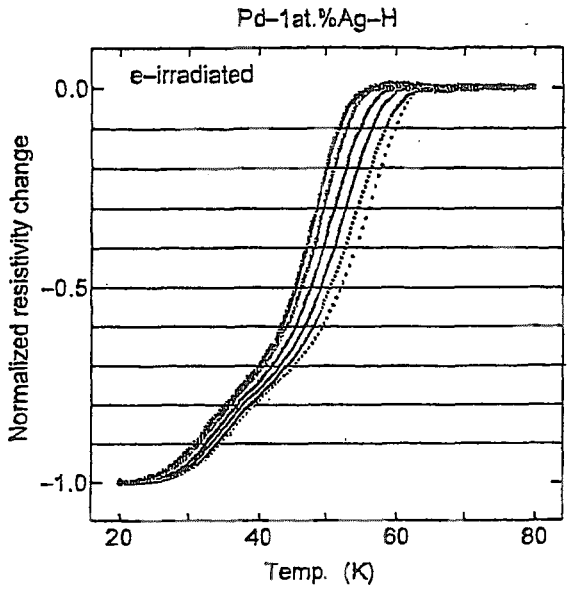

Fig.2 Normalized recovery curves of the electrical resistance after electron irradiation at various heating rates, 0.057, 0.12 ,0.24, 0.47, 0.94, 1.84 K/min (from left side to right side).

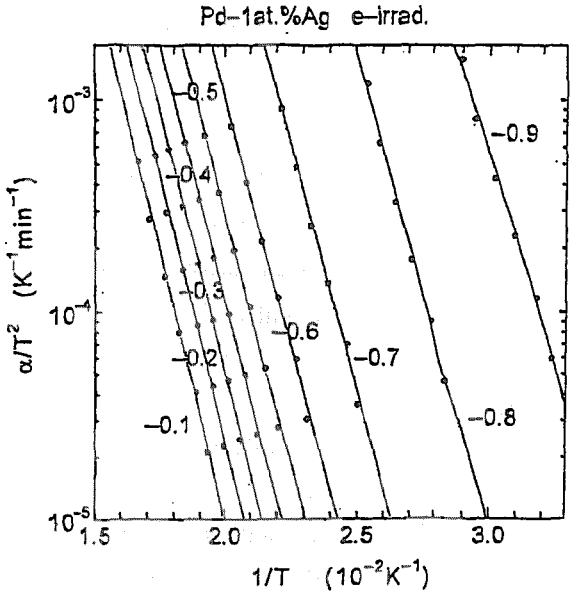

Fig.4 Results of cross cut method at each level of resistance in Fig.2. Slope of the line shows activation energy for hydrogen migration.

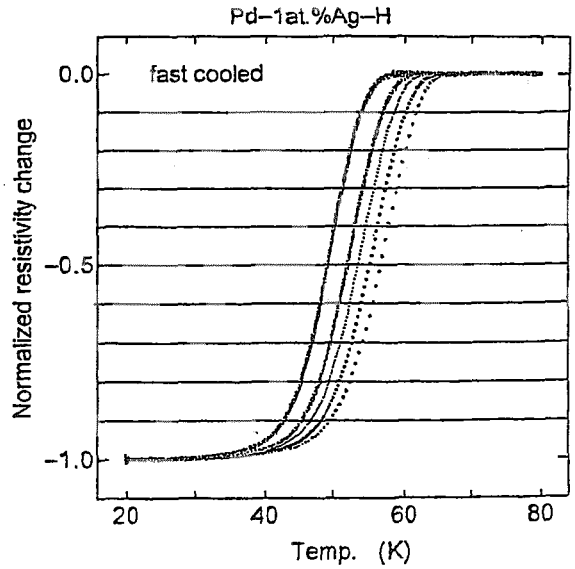

Fig.3 Normalized recovery curves of the electrical resistance after fast cooling at various constant heating rates, 0.057, 0.24, 0.47, 0.94, 1.84 K/min (from left side to right side).

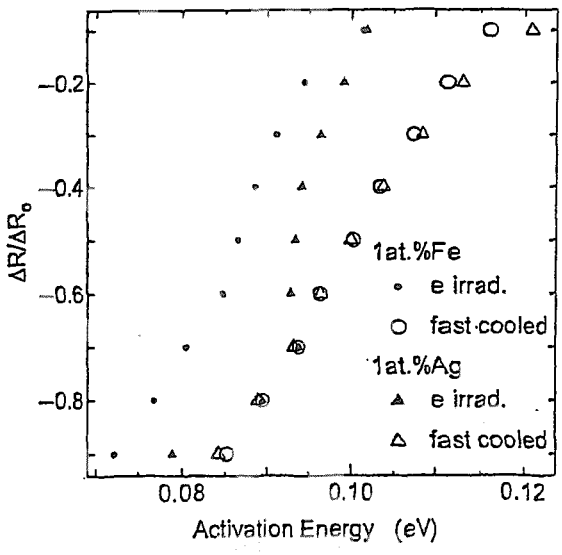

Fig.5 Activation energy for hydrogen migration in Pd-1at. %Fe and Pd-1at.%Ag alloys at the each level in Fig . 2.

4.20 Electron Irradiation Effect in Oxygen-Deficient $EuBa_2Cu_3O_y$

N. Ishikawa*, Y. Chimi*, A. Iwase*, H. Wakana**, T. Hashimoto**,
O. Michikami**
Department of Materials Science, JAERI*
Faculty of Engineering, Iwate University**

1.Introduction

In oxide superconductors $EuBa_2Cu_3O_y$ (y=7) irradiated with energetic electrons, point defects are created in lattice system and the electrical resistivity increase is observed with increasing electron fluence. In the previous study of electrical resistivity change due to irradiation with electrons and ~1MeV ions, it has been found that the initial slope of electrical resistivity-fluence curve is proportional to the energy transfer through elastic collision. This means that the process of defect production due to electron irradiation can be understood as a simple process that is described as elastic displacements of target atoms[1] as long as $EuBa_2Cu_3O_y$ (y=7) oxide superconductor is concerned.

However, we do not know what kind of parameter determines the absolute value of electrical resistivity change per unit electron fluence. In order to find a key to solve this problem, we have artificially removed oxygen atoms from $EuBa_2Cu_3O_y$ (y=7) by a thermal treatment, and irradiated the oxygen-deficient $EuBa_2Cu_3O_y$ (y=6) specimen. Comparison between the resistivity change due to electron irradiation for $EuBa_2Cu_3O_y$ (y=7) and that for $EuBa_2Cu_3O_y$ (y=6) shows that there is a correlation between the resistivity value before irradiation and the irradiation-induced resistivity increase.

2. Experimental Procedure

A c-axis oriented $EuBa_2Cu_3O_y$ (y=7) thin film was prepared on MgO substrate, and it was heated in low oxygen partial pressure. The oxygen-deficient $EuBa_2Cu_3O_y$ was expected to have oxygen content of y=6, since its c-axis lattice parameter was larger by 1.2% than that of $EuBa_2Cu_3O_y$ (y=7). The resistivity at 100K was ρ_o=4.2Ωcm before irradiation. The fluence dependence of electrical resistivity was measured by four-probe method. The specimens were irradiated at low-temperature (100K) with 0.46 and 2.00MeV electrons from a 3MV single-ended accelerator in TIARA, JAERI-Takasaki. In order to avoid the possible irradiation effect of the electrode, the rectangular-shaped slit was placed on the sample, and only the sample was irradiated. In-situ measurement of fluence dependence of electrical resistivity at 100K was performed.

In order to study the thermal stability of irradiation-induced defects, the irradiated sample was annealed up to 300K, and the resistivity was measured during the annealing.

3.Results and Discussion

Figure 1 shows $\Delta\rho/\rho_o$ as a function of

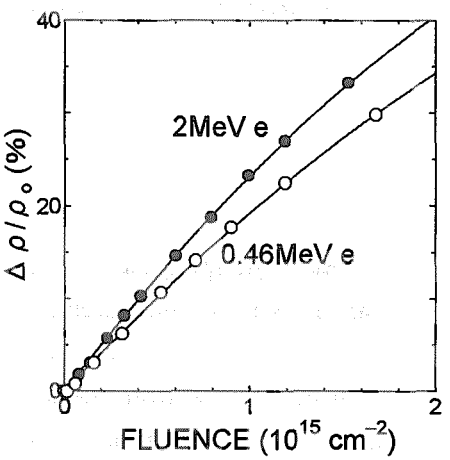

Fig.1 Change in resistivity normalized by the resisitivity before irradiation plotted as a function of fluence for $EuBa_2Cu_3O_y$ (y=6) irradiated with 2MeV electrons. The result for 0.46MeV irradiation is also shown for comparison.

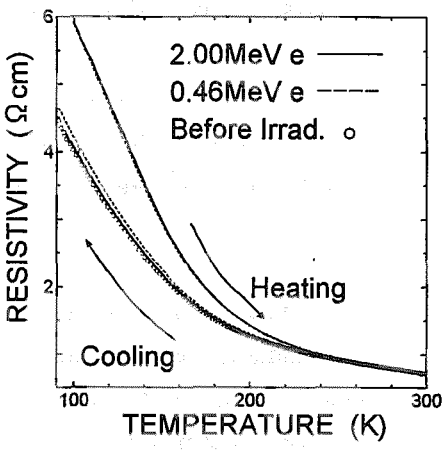

Fig.2 Annealing behavior for $EuBa_2Cu_3O_y$ (y=6) irradiated with 2MeV electrons. The annealing behavior for 0.46MeV electron irradiation is also shown for comparison.

electron fluence, Φ, for $EuBa_2Cu_3O_y$ (y=6) irradiated with 2MeV electrons, where $\Delta\rho/\rho_o$ is change in resistivity normalized by the resistivity before irradiation. Monotonic increase is observed, indicating that lattice defects are created by the irradiation. The initial slope is 2.6×10^{-16} cm^2, which is 4 orders of magnitude larger than that for $EuBa_2Cu_3O_y$ (y=7) irradiated with 2MeV electrons. Since the resistivity at 100K before irradiation for $EuBa_2Cu_3O_y$ (y=6) is about 4 orders of magnitude larger than that for $EuBa_2Cu_3O_y$ (y=7), there is an interesting correlation between resistivity value and the irradiation-induced resistivity change.

In order to study the electron energy dependence of defect accumulation behavior, irradiation effect for 2MeV electrons and that for 0.46MeV electrons are compared as shown in Fig.1. The defect accumulation for 0.46MeV electron irradiation is rather greater, but there is no significant difference between these two irradiations. In order to investigate the electron energy dependence of thermal stability of irradiation-induced defects, annealing behavior is also compared as shown in Fig.2. Although the electron energy is changed from 2MeV to 0.46MeV, thermal stability of the defects is exactly the same. This indicates that energy change from 2MeV to 0.46MeV does not affect the stability of defects. Therefore, the defects created by these irradiations are essentially the same, and only the defect concentration is different.

Reference

1)N. Ishikawa, Y. Chimi, A. Iwase, K. Tsuru and O. Michikami, J. Nucl. Mater. 258-263 (1998) 1924.

4.21 Interaction of Frenkel Pairs with Cu Atoms in Fe-Cu alloys

Y. Chimi*, A. Iwase*, N. Ishikawa*, S. Ishino**
Department of Materials Science, JAERI*
Department of Applied Science, Tokai University**

1. Introduction

Fe-Cu alloys are model alloys for studying the mechanism of irradiation embrittlement in pressure vessel steels of light water reactors. For this purpose, irradiation experiments are mainly performed at high-temperature (~300°C), at which the actual reactors are operated. Since thermal diffusion of irradiation-produced defects accompanied with movement of Cu atoms takes place during the high-temperature irradiation, one must study very complicated irradiation behavior. On the other hand, low-temperature irradiation (such as irradiation at ~20K) can freeze the thermal diffusion of defects and Cu atoms. Therefore, only defect accumulation behavior can be observed. Moreover, annealing experiment after irradiation for studying thermal stability of accumulated defects gives us information on the interaction of defects with Cu atoms in Fe-Cu alloys. Thus, the results obtained by the low-temperature irradiation can be very useful for understanding the complicated behavior of the high-temperature irradiation.

In the present report, we are focusing on the annealing experiment in order to study the interaction of Frenkel pairs with Cu atoms in Fe-Cu alloys irradiated at low-temperature with electrons, which can introduce Frenkel pairs effectively.

2. Experimental Procedure

Two kinds of Fe-Cu alloys with different Cu concentration (0.6 and 0.02wt.%) were used as specimens. The size of the specimen was 1mm×10mm×30μm. Fe-Cu alloy ribbons, which had the same Cu concentration as the specimens, were spot-welded to the specimens as lead wires for electrical resistivity measurement. The specimen was mounted on an aluminum substrate by using epoxy resin (Araldite) in order to insulate the specimen from the substrate. The specimen was irradiated below ~20K with 2.0MeV electrons from a 3MV single-ended accelerator in TIARA, JAERI-Takasaki. During irradiation, the change in electrical resistivity of the specimen, $\Delta\rho$, was measured *in situ* at ~12K as a function of electron fluence. After irradiation, isochronal recovery behavior of $\Delta\rho$ was observed. For precise comparison, the two kinds of Fe-Cu alloy specimens were placed adjacently, and the same irradiation and measurement were performed simultaneously.

3. Results and Discussion

Figure 1 shows the isochronal recovery behavior of change in electrical resistivity of the specimen, $\Delta\rho$. Since $\Delta\rho$ is proportional to the concentration of irradiation-produced defects, the behavior as shown in Fig. 1 corresponds to the defect recovery behavior. For the Fe-0.02wt.%Cu specimen, the defect recovery behavior has almost the same tendency as that for pure iron[1),2)]. For the Fe-0.6wt.%Cu specimen, on the other hand, the recovery behavior above 100K is much different from that for the Fe-0.02wt.%Cu specimen. As can be seen in Fig. 1(b), the recovery peak around 100K, which is attributed to a process of recombination of sole interstitial atom with a vacancy (stage-I_D), is smaller for the Fe-0.6wt.%Cu specimen than that for the Fe-0.02wt.%Cu specimen. On the contrary, for

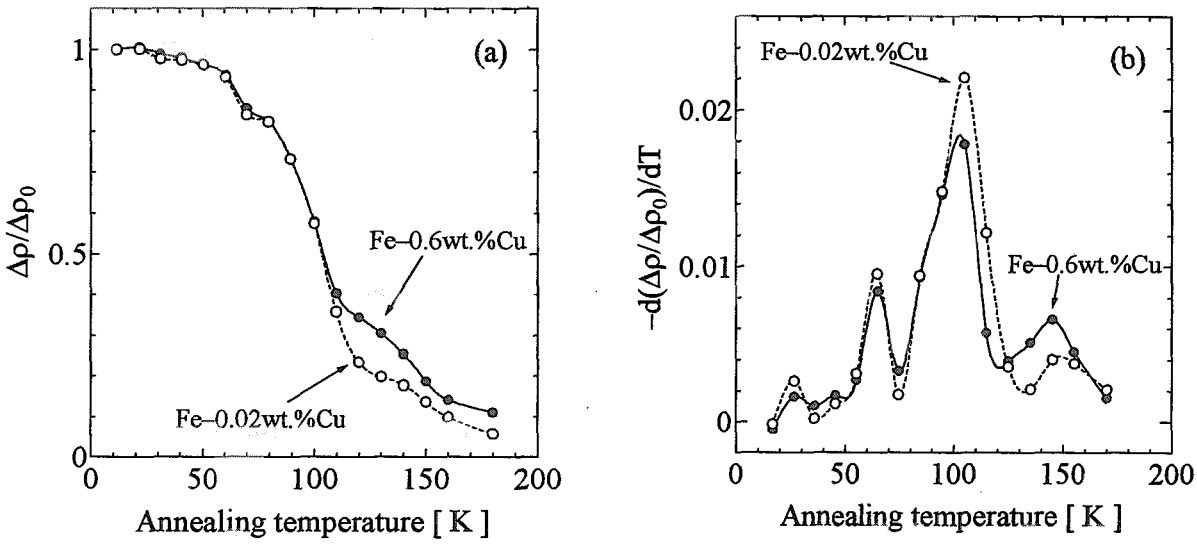

Fig. 1. Isochronal recovery curves of electrical resistivity change (a) and their temperature derivatives (b) for Fe-0.6wt.%Cu and Fe-0.02wt.%Cu specimens. $\Delta\rho_0$ represents $\Delta\rho$ before annealing.

the Fe-0.6wt.%Cu specimen, the recovery peak around 140K is larger than that for the Fe-0.02wt.%Cu specimen. This implies that an interstitial atom trapped by a Cu atom cannot move around 100K and can be dissolved from a Cu atom around 140K, *i.e.* that the movement of interstitial atoms is prevented by Cu atoms.

References

1) S. Takaki, J. Fuss, H. Kugler, U. Dedek, H. Schultz, Radiat. Eff. 79 (1983) 87.
2) P. Ehrhart, P. Jung, H. Schultz, H. Ullmaier, in *Atomic Defects in Metals, Landolt-Börnstein, Numerical Data and Functional Relationships in Science and Technology*, edited by H. Ullmaier (Springer-Verlag, Berlin, 1991), Group III, vol. 25.

4.22 Radiation Enhanced Copper Segregation Processes in Pressure Vessel Steel Model Alloys during Electron Irradiation

S. Ishino*, A. Iwase**, Y. Chimi**, N. Ishikawa**, Bagiyono**, ***,
M. Suzuki****, T. Tobita**** and K. Aizawa****
Department of Applied Science, Tokai University*
Department of Materials Science, JAERI**
Center for Education and Training, Batan, Indonesia***
Department of Reactor Safety Research, JAERI

1. Introduction

Mechanism of radiation embrittlement in pressure vessel steels is one of the most important subjects in recent years related to plant life extension of a light water reactor. Copper has been known to have a strong effect in the embrittlement phenomena and so-called copper-rich precipitates are responsible for embrittlement. However, the exact mechanism of the role of copper has not been fully understood yet. In the present experiment, the role of radiation-induced point defects in copper clustering in Fe-Cu model alloys has been studied by measuring electrical resistivity in-situ during electron irradiation. The results will be discussed in comparison with similar experiments using heavy ion irradiations.

2. Experimental Procedures

2.1. The Specimens

The specimens used for electrical resistivity measurements were prepared from two kinds of high purity Fe-Cu alloys with the copper concentration of 0.02 and 0.6 wt.%, respectively. The final state of heat treatment was 850℃ for 10 minutes followed by quenching by gas cooling. The thickness of the specimen was 30 microns. The specimens were mounted on a copper block side-by-side, electrodes were spot-welded and then copper lead wires were soldered. The two specimens were connected in series.

2.2. Irradiation and Measurements

The specimens were irradiated at 300K with 2MeV electrons from a single end accelerator at Takasaki Research Establishment, JAERI. The irradiation dose was calculated using the displacement energy of 24eV for iron[1,2]. The electrical resistivity was measured in-situ by a conventional four-probe method at 300K as a function of irradiation dose. The temperature of the specimens was measured with a platinum resistance thermometer simultaneously with the resistivity of the specimens.

3. Results

3.1. Dose dependence of resistivity change

Fig.1 shows the dose dependence of resistivity change for (a) Fe-0.6wt.%Cu and (b) Fe-0.02wt.%Cu alloys. Except for an anomalous transient behavior at the beginning of irradiation, the resistivity decreases steadily with dose. In Fig.1, results obtained under high-energy carbon ion irradiations with almost the same dose rate as that for electron irradiations are also plotted. The rate of change of resistivity is strongly dependent on copper concentration. The figure also shows that electron irradiation gives higher rate of change than heavy ions for the same dpa rate. This is probably due to the difference in the fraction of freely migrating defects.

There is a small transient in early stage of irradiation up to a few micro-dpa for electron irradiation, which is compared with ion irradiation case of about 10 micro-dpa. The transient behavior can be eliminated by a small amount of pre-irradiation. This is shown in Fig. 2, (a) for Fe-0.6wt.% Cu and (b) Fe-0.02wt.%Cu alloys.

3.2. Effect of dose rate

Fig.3 shows the effect of dose rate on the resistivity change for (a) Fe-0.6 wt.%Cu and (b) Fe-0.02 wt.%Cu alloys. There is a general tendency that for lower dose rate, the rate of change of resistivity is larger. Similar tendency is also observed in ion irradiation case[3]. This is also consistent with the generally accepted view that the formation process of copper rich precipitates in commercial pressure vessel steels also depends on dose rate.

4. Discussion

4.1. The Mechanism of resistivity decrease

In our earlier work, we have confirmed that in both alloys irradiated at cryogenic temperatures followed by annealing up to 300K, interaction of interstitials with copper atoms is not very strong and most of the defects (90%) are annihilated by annealing up to 300K. Vacancies in pure alloys may be mobile at around 250K. During irradiation at 300K, vacancies can move as well as copper atoms, which are supposed to be mobile via vacancy mechanism. The resistivity decrease may be due to removal of copper atoms from solid solution. The removed copper atoms may form copper clusters or copper precipitates. The initial transient may be due to the nucleation process of such clusters. The slope of the initial resistivity change in the transient regime is too steep to be explained by accumulation of some defects.

4.2. The role of point defects on copper clustering

At 300K, vacancies can be mobile because the vacancy migration stage (Stage III) appears around 250K[2]. The copper clustering process occurs during irradiation because after irradiation the resistivity values do not show any change with time, even after leaving the specimen overnight at 300K. Therefore, we conclude that the copper clustering occurs during annihilation of point defects mostly of vacancies. Interstitials may contribute to the transport of copper atoms because of the presence of weak interaction shown in isochronal annealing curves. The number of copper atoms removed from solid solution per Frenkel pair can be estimated using the resistivity contribution of an atomic percent of copper atoms of about 2.5 $\mu\ \Omega$ cm / at.% Cu. The slope of resistivity change in Fig.1 is about 0.02 $\mu\ \Omega$ cm per 50 μ dpa, implying about 10 copper atoms are removed from solid solution per dpa. This is a very efficient process indicating that copper atoms are transported to cluster sites many times by one vacancy interstitial pair. Recent computer simulation of copper diffusion by vacancy mechanism has also suggested such a possibility[4].

5. Conclusion

2MeV electron irradiation of Fe-Cu alloys at 300K causes copper clustering. The clustering efficiency and role of point defects have been discussed.

References

1) P. G. Lucasson and R. M. Walker, Phys. Rev. 127(1962) 485.
2) Y. Chimi et al., these proceedings.
3) S. Ishino et al., JAERI Tandem Annual Report 2001,(JAERI, 2002) to be published
4) N. Soneda, private communication.

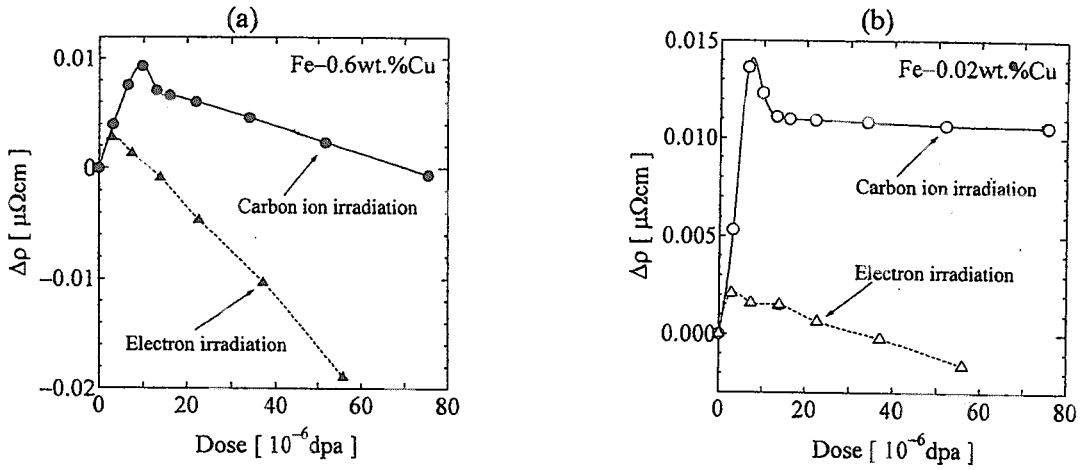

Fig.1 Dose dependence of electrical resistivity change for (a) Fe-0.6wt.%Cu and Fe-0.02wt.%Cu alloys. Comparison of 2MeV electron irradiation with 100MeV C ion irradiation is made.

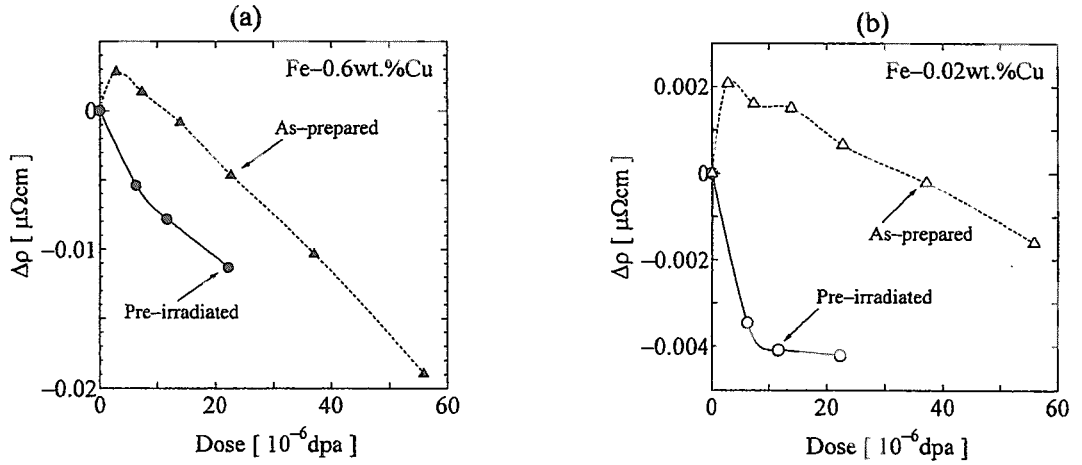

Fig.2 Effect of pre-irradiation on initial transient.

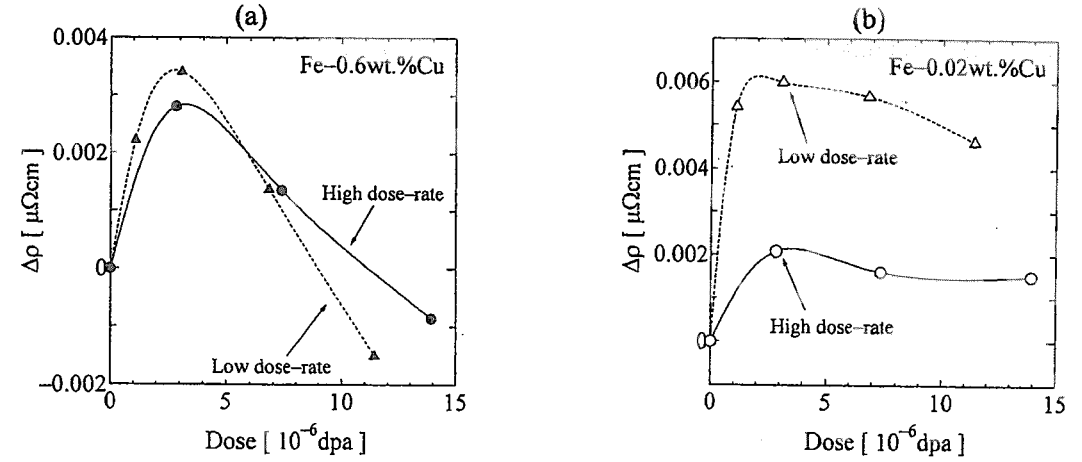

Fig.3 Effect of dose rate on resistivity change. High dose rate is about 10^{-8} dpa/s, whereas low dose rate is about 10^{-9} dpa/s.

4.23 Radiation Effects on Li-Vacancy Ordering in NaTl-type Li Compound

M.Yahagi*,T.Hashimoto*,H.Sugai**,A.Iwase***,Y.Chimi***,
N.Ishikawa***,H.Hamanaka**** and K.Kuriyama****
Faculty of Engineering, Aomori University*,
Department of Research Reactor, JAERI**,
Department of Materials Science, JAERI***,
College of Engineering and Research Center of Ion Beam Technology,
Hosei University****

1. Introduction

NaTl-type intermetallic compound β-LiAl is a good conductor with high electronic conductivity and high diffusivity of Li-ion, and is one of candidates for the useful anode materials in secondary batteries[1]. In β-LiAl (about 48-56 at.%Li), the defect struc- ture at room temperature consists of three types of defects[2] : vacancies in the Li sublattice (free V_{Li}), Li anti-structure atoms in the Al sub-lattice (free Li_{Al}), and complex defects (V_{Li}-Li_{Al}). The free Li-vacancy concentration has a maximum value (about 3.5%) at Li-deficient regions, and decreases with increasing Li content (C_{Li}), while the free Li_{Al} concentration varies from 0 to about 5.4% with increasing C_{Li}. The conduction mechanism for β-LiAl is considerably affected by these defect structures. Near the Li-deficient phase boundary, it is observed that an extraordinary behavior occurs at 95 K in several properties such as electrical resistivity[3] and heat-capacity[4]. This anomalous behavior is attributed to the order-disorder transition of Li vacancies. And the radiation effects in β-LiAl near the Li-deficient phase boundary also make it clear that the Li-vacancy ordering was not collapsed by the Li-ion irradiation, suggesting a relatively strong interaction between free Li vacancies[5]. In the process of Li-ion irradiation, two Frenkel-type defects which consist of a Li interstitial-V_{Li} pair and an Al interstitial-V_{Al} one are introduced in β-LiAl.

In this report, we describe the radiation effects in β-LiAl due to Li atom ejected by electron irradiation.

2. Experimental Procedure

Sample was prepared using 99.9% pure Li and 99.999% pure Al by the same method as reported previously[6]. C_{Li} of this sample was estimated to be about 48.2 at.%Li from the value of the resistivity. Electron irradiation was performed at about 22K with 2 MeV electron from a 3MV single-ended accelerator in TIARA, JAERI-Takasaki. The fluence dependence of electrical resistivity was measured at about 22K using the van der Pauw method after stopping electron irradiation for a time. The temperature of the specimen during electron irradiation was kept below about 22K.

3. Results and Discussion

Figure 1 shows the electron-fluence dependence of resistivity of β-LiAl. $\Delta\rho$ is the difference between the resistivity values before and after electron irradiation. The value of

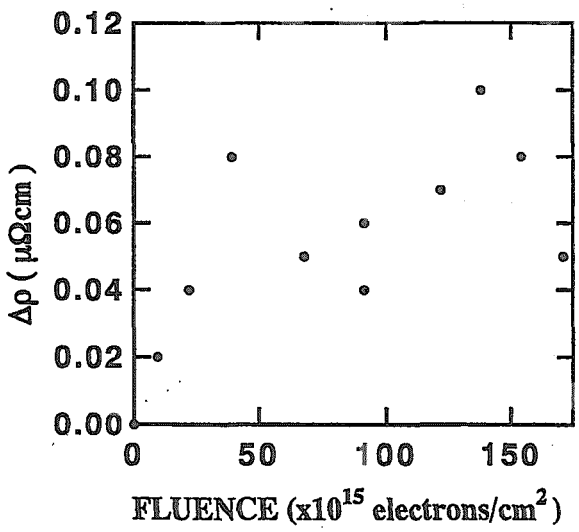

Fig.1 Electron-fluence dependence of resistivity for β–LiAl with C_{Li} = 48.2 at.%Li.

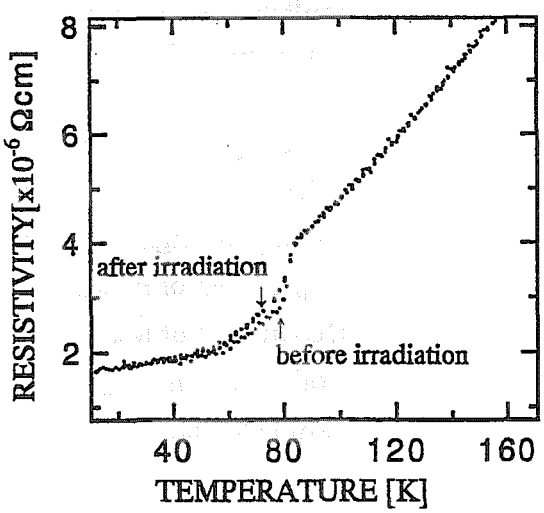

Fig.2 Temperature dependent electrical resistivity of β-LiAl before and after irradiation.

Δρ increases with the electron-fluence from 0 to $1.7x10^{17}$ electrons/cm^2, but seems to change repeatedly with the fluence interval of about $5x10^{16}$ electrons/cm^2. From this result, it is deduced that the former is due to Frenkel-type defects produced by the knock on of Li atoms which orderly arrange in Li sublattice sites, while the latter attributes to the annealing effects for electron irradiation. And the repeatedly change on an electron-fluence dependence of the resistivity also is an interesting pheomenon.

Figure 2 shows the temperature dependence of resistivity of β-LiAl before and after electron irradiation. The electron-fluence is about $1.7x10^{17}$ electrons/cm^2. The resistivity after electron irradiation coincides with that above the ordering temperature. This behavior is different from radiation effects by Li-ion irradiation on β-LiAl. This suggests that there are a few of Frenkel-type defects, consisting of Al interstitial and Al vacancy pair produced by electron irradiation.

The resistivity after annealing at room temperature increases slightly in the temperature range below the ordering temperature, and dose not return to values of the resistivity before irradiation. The result suggests the presence of a few of V_{Li}-Li_{Al} complex defects in β–LiAl.

References

1) C.H.Wen, B.A.Boukamp, R.A.Huggins, and W.Wepner, J.Electrochem.Soc. 126, (1979) 2258.
2) H.Sugai, M.Tanase, M.Yahagi, T.Ashida, H.Hamanaka, K.Kuriyama, and K.Iwamura, Phys. Rev. B52,(1995)4050.
3) K.Kuriyama, T.Kamijoh, and T.Nozaki, Phys. Rev. B22,(1980)470.
4) K.Kuriyama, S.Yanada, T.Nozaki, and T.Kamijoh, Phys. Rev. B24, (1981)6185.
5) K.Kuriyama, Takahashi Kato, Tomoharu Kato, H.Sugai, M.Maeta, and M.Yahagi, Phys. Rev. B52, (1995)3020.
6) M.Yahagi, J. Cryst. Growth. 49, (1980)396.

4.24 Elastic Property of Nanocrystalline Gold after Low-Temperature 2MeV Electron Irradiation

H. Tanimoto, Y. Koda, T. Yamada, S. Sakai, H. Mizubayashi,
N. Ishikawa*, Y. Chimi* and A. Iwase*
Institute of Materials Science, University of Tsukuba
*Department of Materials Science, JAERI

1. Introduction

When the ultrafine particles are mechanically consolidated, the highly disordered grain boundaries (GBs) can be formed to accommodate the neighboring ultrafine crystallites. Characteristic properties of the nanocrystalline (n-) metals prepared through such an athermal process may be associated with the disordered GBs as well as an increased volume fraction of the GB regions[1]. By the progress in technique, the n-metals with the density more than 98 % of the bulk density have been prepared. Surprisingly, the moduli measured for the pore- and contamination-free n-metals are found to be very close to those of the conventional polycrystalline (p-) metals, suggesting that the local density of the GB regions in the n-metals is not so different from the bulk density[2-4]. On the other hand, very recently, the interesting anelastic response is found for the high-density n-metals. For n-Au specimens prepared by the gas deposition method[4], the strong anelastic strain due to a certain GB process can be observed above 200 K[5]. In order to modify the GB state and its effect on the elastic property, anelasticity measurement was conducted for the high-density n-Au irradiated by electron at low-temperature.

2. Experimental Procedure

The high-density n-Au specimen was prepared by the gas-deposition method[4]. The mean grain size and the density of the specimen used were about 20 nm and more than 99 % of the p-Au, respectively. The 2MeV electron irradiation was carried out at 10 K by using the 3MeV single-ended electrostatic accelerator of TIARA, JAERI. The anelasticity measurement was performed by the flexural vibrating-reed method, where the resonant frequency, f, and internal friction, Q^{-1}, were measured by using the specially designed cryostat during and after irradiation.

3. Results and Discussion

Figure 1 shows the strain amplitude, ε, dependence (SAD) in the Young's modulus observed for n-Au before and after irradiation. It is noted that f^2 is proportional to Young's modulus, E. In the ε range in between 10^{-6} to 2 x 10^{-4} as shown in Fig.1, E of n-Au at 6 K shows a decrease by about 1 % with increasing ε. Not shown here but the internal friction, Q^{-1}, shows a slight increase for ε below ~ 1 x 10^{-3}. These SADs of E and Q^{-1} are characteristically observed for n-Au. After 2MeV electron irradiation, the unique SADs of n-Au remained unchanged.

In contrast, a large increase in f was found during the low-temperature irradiation. Figure 2 depicts the normalized change in f at 6 K observed during the irradiation, where the Frenkel-pair concentration was estimated from the electron dose. It is known that the frequency shows a slight decrease by the accumulation of the radiation defects (the bulk effect), and the changing rate per unit Frenkel-pair concentration is reported to be about -10 for the low-temperature electron irradiation of

refractory BCC metals[6]. The increase in f by the irradiation showed a recovery by about 50 % after warm-up to room temperature.

The large increase in f at 6K during irradiation indicates that the radiation defects are trapped at the GBs in n-Au and modify their state or structure. On the other hand, the SAD of the modulus appears to be independent of the radiation defects probably accumulated at the GBs. We surmised that several processes co-exist in the n-Au. The frequency increase by irradiation and the unique SAD may be come from different mechanisms, where the SAD of the n-Au might reflect the characteristic of the crystallites in the n-Au rather than the GBs. A further study is now in progress.

References

1) H. Gleiter, Prog. Mater. Sci. 33(1989) 223.

2) P. G. Sanders, J. A. Eastman and J. R. Weertman, Acta Mater. 45(1997)4019 : P. G. Sanders, C. J. Youngdahl and J. R. Weertman, Mater. Sci. Eng. A234-236(1997)77.

3) X. Y. Qin, X. R. Zhang, G. S. Cheng and L. D. Zhang, Nanostruct. Mater. 4(1998)661.

4) S. Sakai, H. Tanimoto and H. Mizubayashi, Acta Mater. 47(1999)211.

5) S. Sakai, H. Tanimoto and H. Mizubayashi, Scripta Mater., 45(2001) 1313.

6) H. Tanimoto, H. Mizubayashi, R. Masuda, S. Okuda, T. Iwata, H. Takeshita and H. Naramoto, phys. stat. sol. (a), 132(1992)353.

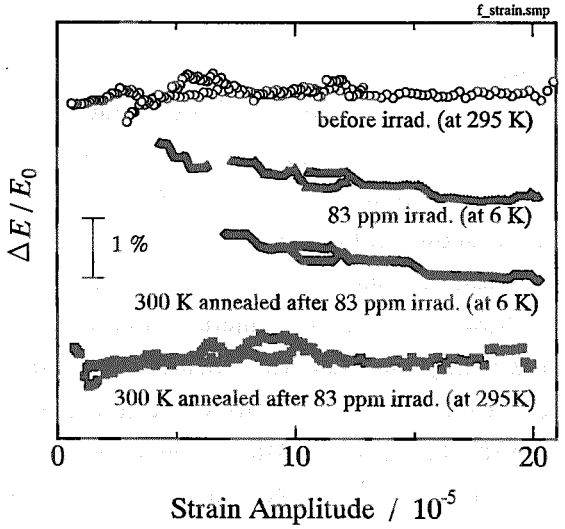

Figure 1. Strain amplitude dependence in the Young's modulus, E, observed for n-Au before and after electron irradiation. E_0 shows the E observed at the smallest strain.

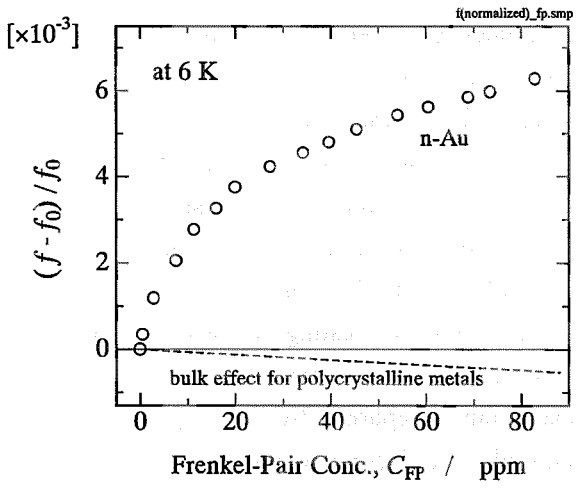

Figure 2. Change in the resonant frequency, f, observed during low-temperature 2MeV electron irradiation, where f^2 is proportional to E. For the comparison, the bulk effect observed for the polycrystalline metals is also shown.

4.25 ESR CHARACTERIZATION OF ACTIVATION OF IMPLANTED PHOSPHORUS IONS IN SILICON CARBIDE

J. Isoya*, N. Mizuochi*, T. Ohshima**, A. Ohi**, N. Morishita**, H. Itoh**
University of Library and Information Science*, Departmnt of Material Development, JAERI**

1. Introducttion

Silicon carbide (SiC) is a promising material for electronic devices of high-frequency, high-power, high-temperature applications and for those used in a harsh environment. One of key issues for realizing SiC devices is to establish the technology of the selective area doping. In SiC, due to the difficulty of doping by thermal diffusion, ion implantation is a potential method of introducing dopant atoms in the device fabrication. In the case of silicon, ion implantation is successfully used for doping in LSI technology, since the implants are easily driven to the required site and since the crystallinity is easily recovered by annealing. Ion implantation doping of SiC is much more complicated than that of silicon, since the amorphization of the implanted layer need to be prevented and since some of radiation damages and secondary defects produced by annealing including the implant-defect (vacancy, interstitial)-complexes might be stable up to rather high temperatures. Thus, selection of the implantation conditions and that of the post-implantation annealing conditions (annealing temperature, annealing time) are critically important to reduce the radiation damages and to drive the implant into the required lattice site.

In addition to nitrogen, which is unintentionally incorporated during the crystal growth, phosphorus acts as a shallow donor[1]. To improve the doping efficiency by varying the conditions of phosphorus ion implantation and those of post-implantation annealing, microscopic characterization of implanted phosphorus ions as well as those of implantation-induced defects is important. Electron spin resonance (ESR) is a powerful tool of characterizing impurities and defects of low concentrations by supplying detailed structural information of atomic level. We have applied ESR method to elucidate at microscopic level the thermal behaviour of implanted ions and radiation damages. Both megaelectronvolt (9-21 MeV) and kiloelectronvolt (340 keV) phosphorus ion implantations of 6H-SiC have been studied.

2. Experiments

Samples used were n-6H-SiC crystals (Nippon Steel Corp., N_A-N_D=~10^{17}cm^{-3}). For each of high-energy implantations (implantation temperature: 800°C and 1200°C), a rectangular plate (3 mm×10 mm×1.5 mm) was irradiated using a 3 MV tandem accelerator with phosphorus ions (5×10^{13} cm^{-2} at each of 9 stages of energy between 9 and 21 MeV). For the implantation of 340 keV phosphorus ions with the total dose of 2×10^{13}cm^{-2} at 800°C, rectangular plates (3 mm×10 mm×0.22 mm) were used. All implantations were carried out along the [0001] axis.

The ESR spectra were recorded on a Bruker ESP300 X-band spectrometer by using an Oxford Instrument ESR-900 to control the sample temperature. For ESR measurements of the thick samples, a single plate glued on a high-purity silica-glass rod was used. The ESR signal of Cr^{3+} in a single crystal of ruby comounted with the sample was used as the reference of the spin concentration. The signal intensity was estimated by double integration of the first derivative signal. For ESR measurements of the thin samples, 4 slices were stacked into a sample tube of high-purity silica glass.

3. Results and Discussion

To characterize the electric activation of phosphorus ions at microscopic level, it is critically important to observe the ESR signals from the phosphorus shallow donors in which the phosphorus atoms are driven into the required lattice site. In the ESR method, identification of phosphorus related centers, for both phosphorus in the shallow donor state and phosphorus involved in paramagnetic defects such as phosphorus-vacancy complexes, is based on the observation of hyperfine interaction of ^{31}P nucleus (I=1/2, natural abundance 100%).

The ESR spectrum of n-6H-SiC which was annealed at 1650°C (30 min.) after the implantation of the high energy phosphorus ions at 1200°C is shown in Fig.1. Each of two spectra labeled P_a and P_b consists of two-lines arising from ^{31}P hyperfine structure. The angular dependence of the line positions of P_a and P_b is shown in Fig.2. The ESR parameters obtained are listed in Table I. For both P_a and P_b, the anisotropy of the hyperfine splitting is small. The small isotropic part of the ^{31}P hyperfine interaction indicates that the wave function of the unpaired electron is weakly localized on the phosphorus atom (the spin density on the phosphorus: 0.015 and 0.014 for P_a and P_b, respectively). These features are expected for isolated phosphorus shallow donors. The P_a and P_b spectra were originally observed in 6H-SiC in which phosphorus had been introduced by neutron transmutation of ^{30}Si [2),3)]. In the crystal lattice of 6H-SiC, there are three inequivalent sites (a hexagonal site h and two cubic sites k_1 and k_2) for each of silicon and carbon. The P_a and P_b spectra were identified to be originating from the isolated shallow phosphorus donors on cubic silicon sites[4)]. ESR spectrum from the isolated shallow phosphorus donor on hexagonal silicon site, which is likely to be hidden underneath the strong signals of the nitrogen shallow donors, has not been reported.

The P_a and P_b spectra were not observed before the annealing at 1650°C. The amount of P_a and P_b were similar among three samples, sample A which was annealed at 1650°C (30 min.) after implantation at 1200°C, sample B which was annealed at 1650°C (3 min.) after implantation at 1200°C, and sample C which was annealed at 1650°C (30 min.) after implantation at 800°C. In samples B and C, the ESR signals of phosphorus-vacancy complexes [2),3)] were observed. The ratio of the isolated shallow phosphorus donors (the sum of P_a and P_b) relative to the amount of the implanted phosphorus ions is estimated to be ~0.01. It is likely that most of the phosphorus ions implanted are captured by defects which are not ESR-active.

The P_a and P_b spectra in our samples were

observed in a wide temperature range between 8 K and 80 K. After attaining the ESR measurement conditions to optimize the ESR signals of P_a and P_b by using the samples implanted with high energy phosphorus ions, ESR measurements were carried out for 6H-SiC sample implanted with 340 keV phosphorus ions. The total number of phosphorus ions implanted in the sample used for the ESR measurements (4 slices of 3 mm×10 mm plates) was 2.4×10^{13}. We could observe the P_a and P_b signals in this sample. Thus, ESR method is useful for characterizing the electric activation of phosphorus ions implanted into 6H-SiC in the implantation dose range in which phosphorus atoms activated are in isolated shallow donors.

References

[1] T. Troffer, C. Peppermüller, G. Pensl, K. Rottner and A. Schöner, J. Appl. Phys. 80, 3739 (1996)

[2] A. I. Veinger, A. G. Zabrodskii, G. A. Lomakina and E. N. Mokhov, Sov. Phys. Solid State 28, 917 (1986)

[3] S. Grelich-Weber, phys. stat. sol. (a) 162, 95 (1997)

[4] S. Greulich-Weber, M. Feege, J. –M. Spaeth, E. N. Kalabukhova, S. N. Lukin and E. N. Mokhov, Solid State Commun. 93, 393 (1995)

TABLE I. ESR parameters (30 K) of shallow phosphorus in *n*-6H-SiC irradiated with high-energy P-ions

	$g_{//}$	$g_{\perp}$	$A_{//}$ (mT)	$A_{\perp}$ (mT)
P_a	2.00426	2.00334	5.50	5.42
P_b	2.00440	2.00307	5.08	5.09

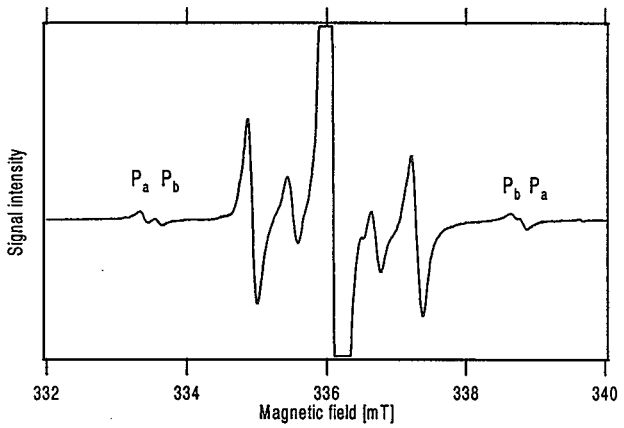

Fig. 1 ESR spectrum (B//[0001], 30K) of n-6H-SiC annealed at 1650°C (30 min.) after implantation of high energy (9-21 MeV, 5×10^{13}cm^{-2}×9 stages, 1200°C) phosphorus ions. The weak signals (P_a, P_b) with the hyperfine splitting of ~5 mT is arising from the phosphorus shallow donors. Strong signals are mostly arising from the nitrogen impurities.

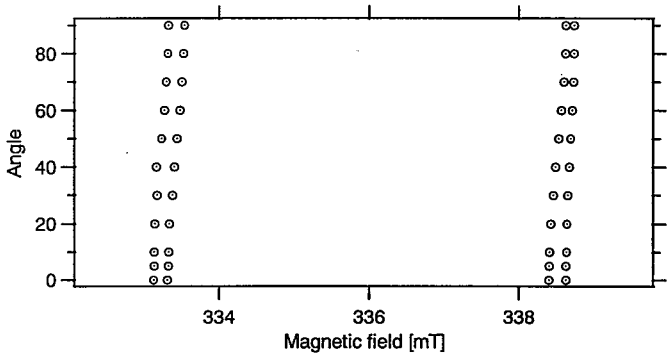

Fig. 2 Angular dependence of the line positions of P_a and P_b in n-6H-SiC (30 K).

This is a blank page.

5. Material Analysis

5.1 Fast Diffusion of Defect Clusters in Copper under Irradiation with 100-keV Carbon Ions

Hiroaki Abe and Naoto Sekimura*

Nuclear Engineering Research Laboratory, University of Tokyo, Shirakata Shirane 2-22, Tokai, Naka, Ibaraki 319-1188, Japan
Department of Quantum Engineering and Systems Science, University of Tokyo, Hongo 7-3-1, Bunkyo, Tokyo 113-8656, Japan *

1. Introduction

Irradiation with ions and neutrons produces bunches of atomic displacements in materials, so-called displacement cascades. Recent studies with molecular dynamics (MD) simulations predicted punching of tiny interstitial-type dislocation loops at the periphery of displacement cascade regions in iron and copper. Their activation energies of diffusion were estimated less than 0.1 eV. Transmission electron microscopic (TEM) observations were done after irradiations but no clear evidence has been derived yet, probably because they are active only under irradiation. Therefore, neither their lifetime nor impurity effect is clarified. The purpose of this study is to report first experimental evidence of such highly-mobile defect clusters by in-situ TEM observations under ion irradiation and to clarify the defect-impurity interactions.

2. Experimental Procedure

Well-annealed copper disks were electrochemically perforated to achieve electron-transparent thin foils. They were, then, irradiated with 100 keV carbon ions at temperatures from 570 to 1070 K in an electron microscope interfaced with an ion accelerator. Microstructural evolution was simultaneously observed and videotaped.

3. Results and Discussion

Tiny defect clusters (less than 10 nm in size) were formed by ion irradiation, whose accumulation rate correlated with irradiation time. Majority of them were vacancy- type clusters including stacking fault tetrahedra. Continuous irradiation annihilated them with lifetime ranging from 0.1 to 3 s. In addition to such clusters, we observed highly-mobile

clusters only during irradiation, which are, compared with MD simulations, presumably interstitial dislocation loops consisting of crowdions one-dimensionally diffusing along the crowdion direction. Interesting to note is that they moved back-and-forth because of surface mirror effect, well-known in dislocations close to surface. The clusters occasionally disappeared when they absorb enough vacancies.

TRIM calculations indicated roughly 20 % or less of irradiated ions remained in the samples. As increasing ion fluence, we observed decrease in evolution rate of defect clusters both vacancy- and interstitial-type, longer lifetime of the clusters, and lower mobility of the interstitial loops. Unless carbon is one of interstitial-type impurities in copper, it may substitute or strongly-bonded with vacancies resulting retardation of diffusion of vacancies and even mobile clusters.

5.2 *In-situ* Observation of Growth Processes of Transition Metal Nitride Thin Films by Nitrogen-Implantation

Y. Kasukabe, Y. Fujino, S. Saito*, Y. Yamada*, H. Abe**
International Student Center / Department of Electronic Engineering, Tohoku University, *Department of Quantum Science and Energy Engineering, Tohoku University, **Nuclear Engineering Research Laboratory, University of Tokyo.

1. Introduction

Titanium nitrides, carbides and oxides show metallic, covalent and also ionic properties, which make them interesting from both points of view of fundamental research and technical applications. Their fascinating physical properties are naturally related to the electronic structure. It is well known that in transition metals the valence d orbitals are more contracted than valence s and p orbitals, and split in energy by the bonding interaction with the ligand atoms such as carbon (C) and nitrogen (N) ones. The bonding interaction gives rise to transformations of the transition metal sublattice, and to covalent properties. Because of the covalent properties, the nitrides of titanium (Ti), one of the typical transition metals, are technologically important, for example, as corrosion-resistant coatings on cutting tools and diffusion barriers in silicon microcircuits.[1,2] It has also been revealed that properties of epitaxially-grown Ti nitride films are superior to those of polycrystalline ones. Thus, much interest has been focused on the epitaxial films. Recently, it was reported in the light of *ex-situ* experiments that NaCl-type TiN films were epitaxially grown by the N-implantation into evaporated Ti films.[3] However, the nitriding process of epitaxial Ti films, especially of the heated films, by N-implantation has not been sufficiently understood.

The purpose of this work is first to throw light on changes of the crystallographic structure of heated Ti films by N-implantation, using *in-situ* transmission electron microscopy (TEM), and then to discuss the epitaxial growth mechanism of Ti nitride films.

2. Experimental

Detailed descriptions of the preparation of evaporated-Ti films were presented in the earlier paper.[3] The 100-nm-thick Ti films were deposited by an electron-beam heating method in an ultra-high vacuum onto thermally cleaned NaCl substrates held at room temperature (RT). The ultimate pressure in the working chamber was less than 4×10^{-9} Torr. The Ti films separated from NaCl substrates were heated up to 600℃ at the heating rate of 2℃/min in the 400 kV analytical and high resolution TEM combined with ion accelerators at JAERI-Takasaki.[4] The implantations of nitrogen ions (N_2^+) with 62 keV into the deposited Ti films held at 600℃ were performed in the TEM. The pressure in the TEM specimen chamber was below $1\text{-}2\times10^{-7}$ Torr. According to the Monte Carlo simulation using the TRIM85 code, the projected range of N_2^+ with 62 keV was 55 nm, and thus most of the implanted ions are thought to be retained inside the Ti films. The N-concentrations in Ti films were able to be estimated from the implantation dose measured by a Faraday cage. The maximum dose in this experiment was 4.24×10^{17} ions/cm^2, which corresponded to the N/Ti ratio of 0.75 (the average atomic concentration of N in the Ti film).

3. Results and discussion

The typical result of the TEM observation of the unimplanted Ti film held at RT is shown in Fig. 1. An analysis of the electron diffraction (ED) pattern of Fig. 1 (a) indicates that hcp-Ti

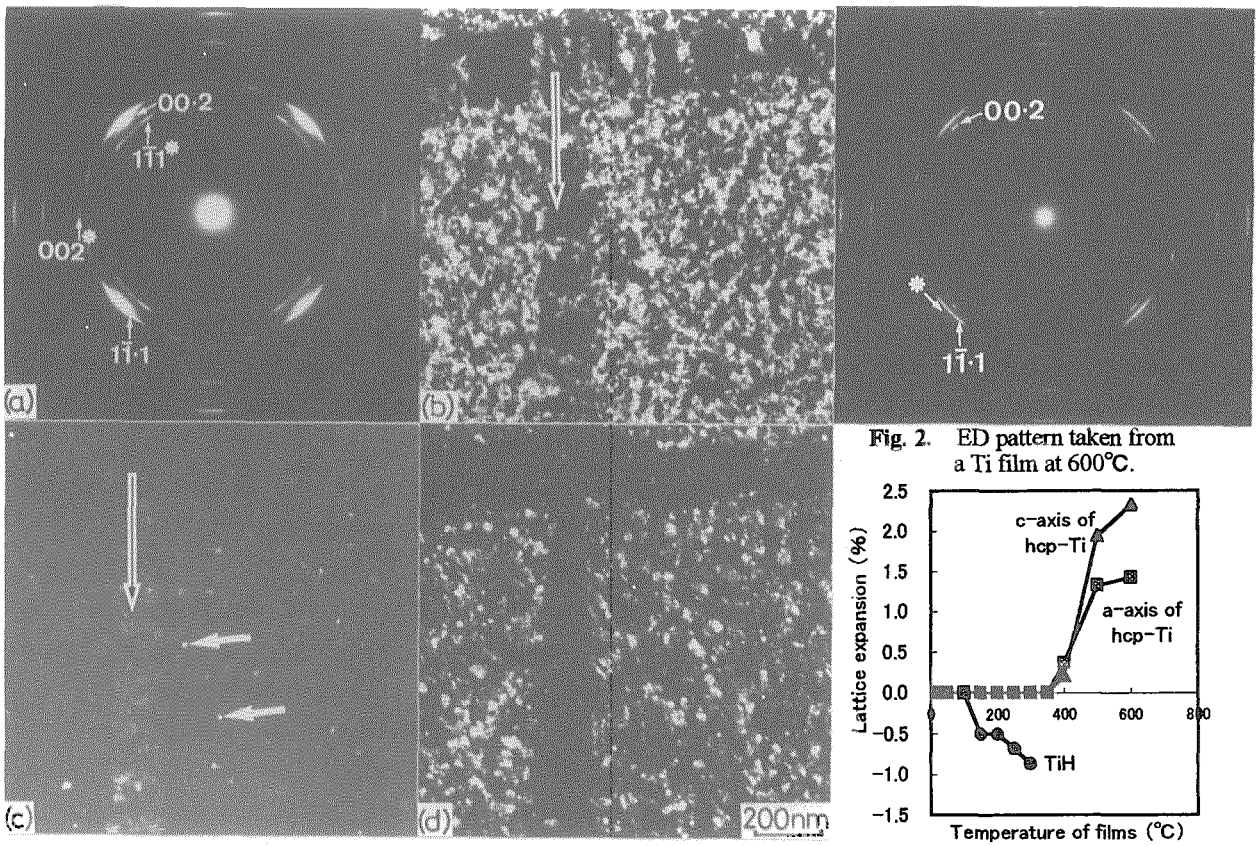

Fig. 1. ED pattern (a), and BF (b) and DF (c), (d) images taken from a 100-nm-thick Ti film. (c) and (d) were taken with the 002* reflection of TiH_x and the $1\bar{1}\cdot1$ reflection of hcp-Ti, respectively.

Fig. 2. ED pattern taken from a Ti film at 600°C.

Fig. 3. Variation of the lattice expansion

(lattice constants: a=0.296 nm, c=0.471 nm) and CaF_2-type TiH_x ($x \fallingdotseq 1.5$; lattice constant: a=0.441 nm) mainly exist in this film. The reflection indicated by the three-index system with an asterisk, *, is obtained from TiH_x, whereas those indicated by the four-index system are obtained from hcp-Ti. It was found in our previous paper[3] that Ti films deposited onto NaCl substrates spontaneously absorbed H from the interior of the NaCl, and then TiH_x grew partially in addition to hcp-Ti. The bright field (BF) image of Fig. 1(b) shows the band-like contrast indicated by an arrow, elongated in the <110> direction of TiH_x and NaCl. Figures 1(c) and 1(d) are, dark field (DF) images taken from reflections labeled 002* and $1\bar{1}\cdot1$, respectively. The orientation relationships between the hcp-Ti and the NaCl substrate are $(03\cdot5)Ti//(001)NaCl$ and $[2\bar{1}\cdot0]Ti // [\bar{1}10]$ NaCl: $(03\cdot5)$-oriented hcp-Ti, and $(\bar{2}1\cdot0)Ti//(001)NaCl$ and $[00\cdot1]Ti//[100]$ NaCl: $(\bar{2}1\cdot0)$-oriented hcp-Ti. The $(03\cdot5)$-oriented hcp-Ti gives rise to, for example, the $1\bar{1}\cdot1$ reflection, whereas the $00\cdot2$ reflection stems from $(\bar{2}1\cdot0)$-oriented hcp-Ti. Judging from the ED intensity of Fig. 1(a), the growth of the $(03\cdot5)$-oriented hcp-Ti is preferred to $(\bar{2}1\cdot0)$-oriented one. On the other hand, the orientation relationship between the TiH_x and NaCl is $(110)TiH_x//(001)NaCl$ and $[001]TiH_x// [110]NaCl$: (110)-oriented TiH_x. Figure 1(c) shows that (110)-oriented TiH_x grows in the band-like contrast region except small crystallites as indicated by arrows, whereas epitaxial hcp-Ti grows only outside the band-like contrast regions as seen in Fig. 1(d).

The depositted-Ti film, which showed such ED pattern as Fig. 1(a), was heated up to 600°C. The ED pattern of the Ti film at 600°C is shown in Fig. 2. An analysis of Fig. 2 indicates that hcp-Ti (lattice constants: a=0.299 nm, c=0.482 nm) mainly exists in this film and that no ED pattern of TiH_x can be seen. Judging from the

ED intensity of Fig. 2, the growth of the (03 · 5)-oriented hcp-Ti is preferred to ($\bar{2}$1 · 0)-oriented one. The weak and diffuse reflection indicated by an asterisk are seen just outside the 1 $\bar{1}$ · 1 reflection. This means that a small amount of TiC_z (lattice constant: a=0.432 nm) may coexist in this film. Figure 3 shows the variation of the lattice expansions of hcp-Ti, TiH_x, with the temperature of heated deposited-Ti films. The lattice expansion is defined as $100(a_T - a_0)/ a_0$, where a_0 is a lattice constant of a crystallite in unimplanted films held at RT, and a_T is that in heated films held at a temperature T. There is no noticeable change in ED patterns up to 100℃. The lattice constant of TiH_x decreases gradually with the rise of temperature from 100℃ to 300℃. Furthermore, the ED intensity of TiH_x also decreases with the rise of temperature and there is no ED from TiH_x at 350℃. These results mean that H atoms which constitute TiH_x escape from it with heating films, and are completely dissociated at 350℃. The H-dissociated unstable fcc-Ti sublattice is transformed into hcp-Ti. On the other hand, there is no noticeable change of lattice constants of hcp-Ti up to 350℃. The lattice constants increase gradually with the rise of temperature from 400℃ to 600℃. One of the reasons of the lattice expansion is thermal lattice vibration. However, taking into account the existence of a small amount of TiC_z in Fig. 2, the occupation of C atoms in octahedral sites of hcp-Ti might be one of the diving forces of the lattice expansion.

Nitrogen ions were implanted into the Ti films held at 600℃, which showed such ED patterns as Fig. 2. The ED pattern of the N-implanted Ti film (N/Ti=0.75) at 600℃ is shown in Fig. 4. An analysis of the ED pattern indicates that NaCl-type TiN_y (lattice constants: a=0.424 nm) and a small amount of both hcp-Ti (lattice constants: a=0.299 nm, c=0.487 nm) and TiC_z (lattice constant: a=0.432 nm) exist in this film. TiC_z can be considered to be formed during heating of the deposited Ti films. The orientation relationships between hcp-Ti and NaCl are the same as those in unimplanted Ti films. Crystallites of TiN_y are formed in the two orientations; (001)-oriented TiN_y: (001) TiN_y //(001)NaCl and [100] TiN_y //[100]NaCl, and (110)-oriented TiN_y: (110)TiN_y//(001)NaCl and [001]TiN_y//[110]NaCl. Most of crystallites in Figs. 2 and 4 are (03·5)-oriented hcp-Ti and (001)-oriented TiN_y, respectively. Therefore, it can be considered that (001)-oriented and (110)-oriented TiN_y are epitaxially formed by the transformation of (03·5)-oriented and ($\bar{2}$1 · 0)-oriented hcp-Ti, respectively.

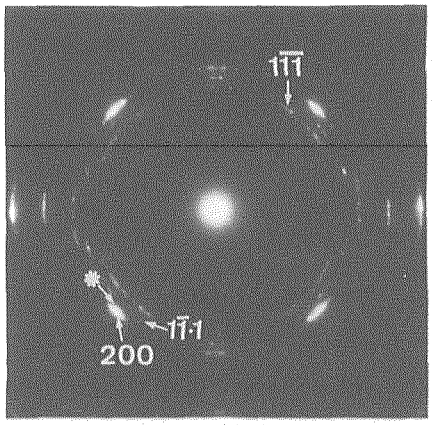

Fig. 4. ED pattern of the N-implanted Ti film (N/Ti=0.75) at 600℃. TiN_y, hcp-Ti and TiC_z give rise to the three-index reflection, four-index one and reflection indicated by an asterisk, respectively.

References

1) G. S. Chen, J. J. Guo, C. K. Lin, Chen-Sheng Hsu, L. C. Yang, and J. S. Fang, J. Vac. Sci. & Technol. A20 (2002) 479.
2) J. E. Sundgren, Thin Solid Films 128 (1895) 21.
3) Y. Kasukabe, N. Saito, M. Suzuki, Y. Yamada, Y. Fujino, S. Nagata, M. Kishimoto, and S. Yamaguchi, J. Vac. Sci. & Technol. A16 (1998) 482.
4) H. Abe, H. Naramoto, K. Hojou, and S. Furuno, The TEM-Accelerators Facility at JAERI-Takasaki and its Application to Materials Science, JAERI-Research

5.3 Preparation of Epitaxial Anatase TiO_2 Films by Pulsed Laser Deposition

S. Yamamoto, T. Sumita, T. Yamaki, A. Miyashita, H. Itoh, H. Naramoto*
Department of Material Development, JAERI
Advanced Science Research Center, JAERI*

1. Introduction

Titanium dioxide (TiO_2) photocatalyst has attracted much interest from the viewpoints of basic science and applications. Thus, the synthesis of high quality epitaxial TiO_2 has been required to understand the transportation process of photo-activated electrons and holes in the surface layer. In the present study, we performed the growth of TiO_2 films with anatase structure by pulsed laser deposition (PLD) with an ArF excimer laser under the controlled O_2 atmosphere. The effects of substrate and substrate temperature on film quality were discussed.

2. Experimental

By considering the crystal structure and the lattice misfit between TiO_2 and single crystal substrate, we used a $LaAlO_3$ (001), LSAT (001), $SrTiO_3$ (001) for anatase-TiO_2. The PLD was used the ArF excimer laser (wavelength: 193 nm, pulse duration: 15 ns, repetitionrate: 10 Hz) with an incident angle of 45°. The average laser energy density was 150 mJ/cm^2. The laser was focused onto a titanium (purity: 99.99%) target rotated continuously. Oxygen gas was flowed into the growth chamber through a mass flow meter to achieve the pressure about 6×10^{-3} Torr. The substrates temperature was changed from 349 to 608°C. The crystallographic relationships between TiO_2 films and substrates were determined by x-ray diffraction measurements using a high-resolution diffractometer (X'Pert-MRD, Philips). The RBS/channeling analysis using 3 MV single-stage-accelerator was employed to characterize the epitaxial films.

3. Results and Discussion

Fig. 1 shows the typical θ-2θ x-ray diffraction patterns from the TiO_2 film on the (a) $LaAlO_3$ (001), (b) LSAT (001), (c) $SrTiO_3$ (001) substrates, respectively. The films were grown at 566°C and the film thickness was about 200 nm. In Fig 1. (a) to (c), only the reflections from the anatase TiO_2 (004) and (008) are observed without any reflection from the substrate, which indicates that the only anatase TiO_2 (001) films were epitaxially grown on the (001) plane of $LaAlO_3$, LSAT, $SrTiO_3$ substrates. For the substrate with different orientations such as $SrTiO_3$ (110), $LaAlO_3$ (110) substrate, the epitaxial anatase TiO_2 films were not grown. These films were polycrystalline and were mixed with the anatase and rutile structures. The in-plane orientations of epitaxial films were examined through the pole figure measurement. Anatase TiO_2 (001) films on the $LaAlO_3$ (001), LSAT (001) and $SrTiO_3$ (001) have the fourfold symmetry and they match well along their $[100]_{anatase}$ and $[100]_{substrate}$ in-plane direction with small lattice misfit, 0.13 % for $LaAlO_3$, 2.14 % for LSAT and 3.06 %, for $SrTiO_3$, respectively.

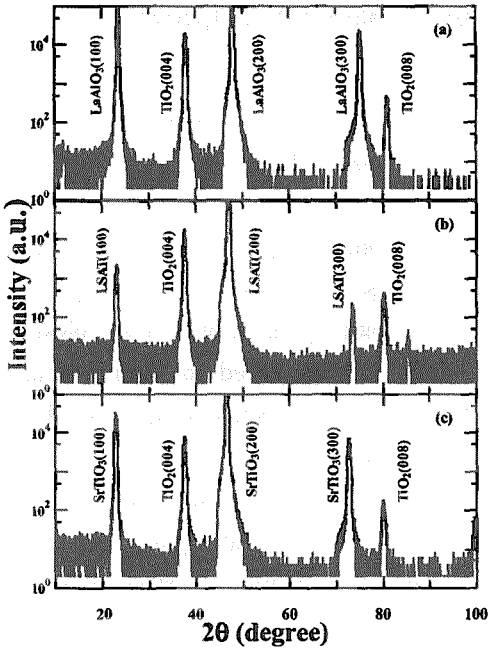

Fig. 1: The x-ray diffraction patterns from the epitaxial anatase TiO_2 films on the (a) $LaAlO_3$ (001), (b) LSAT (001), (c) $SrTiO_3$ (001), respectively. The films were deposited at 566°C.

Fig. 2 summarizes the crystal quality changes as a function of the substrate temperature by referring to the FWHM of anatase (004) rocking curve. It can be seem that high quality anatase TiO_2 (001) films were obtained on the $LaAlO_3$ (001) substrate at the temperature higher than 450°C. In this study, the best crystal quality of the anatase (001) film was obtained on the $LaAlO_3$ (001) at the substrate temperature of 608°C, and the FWHM of anatase (004) rocking curves was 0.054.

Fig. 3 illustrates two kinds of 1.5 MeV $^4He^+$ RBS spectra from the anatase film on the $LaAlO_3$ (100) taken under the random and the axial channeling condition. The aligned spectrum was taken with the beam directed along the <001> axis of the anatase film. In this measurement, thicker film was prepared to distinguish the contributions from the grown film and the substrate composed of heavy element in the RBS spectra. The step edges from Ti component (0.6 MeV ~ 1.1 MeV) in the TiO_2 grown film was partially overlapped with the contribution from La component of the $LaAlO_3$ substrate. The yield at 1.0 MeV regions is from the Ti component of the anatase TiO_2 film, and the huge reduction of this yield under the axial channeling condition suggests that the grown film has almost the same crystal quality inherited from the interface with TiO_2 <001> crystallographic axis parallel to the $LaAlO_3$ <100> axis.

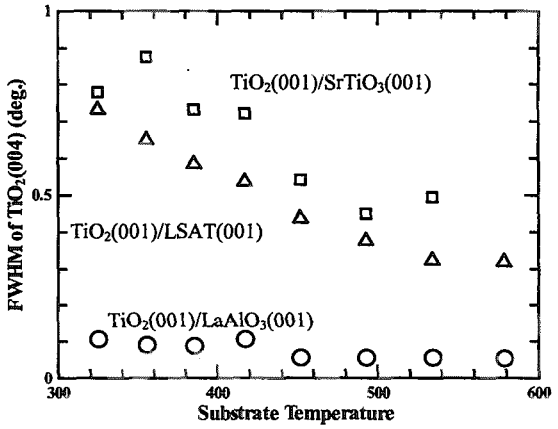

Fig. 2 FWHM of anatase (004) rocking curve as a function of the substrate temperature. (○)$LaAlO_3$(001), (△) LSAT(001), (□) $SrTiO_3$(001) substrates.

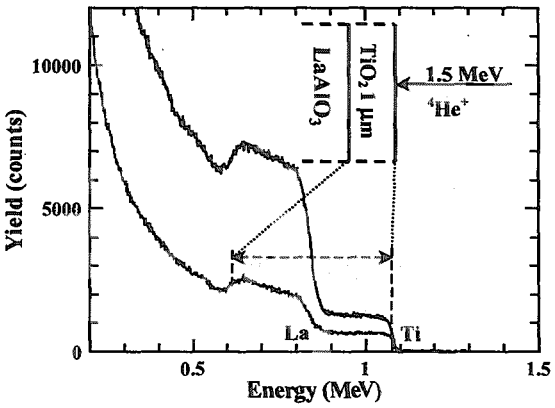

Fig. 3 1.5 MeV $^4He^+$ RBS/channeling spectra from the anatase TiO_2 film with the thickness about 1μm on $LaAlO_3$(100) substrate.

5.4 Fabrication of titanium dioxide nanoparticles on sapphire

Yeongsoo Choi, Shunya Yamamoto, Hiroaki Abe and Hisayoshi Itoh
Department of Materials Development, JAERI

Since the Fujishima-Honda effect was reported in 1972 [1], titanium dioxide (TiO_2) has been applied to a variety of environmental problems such as water and air purification. Many researchers have studied nanoscale technology on TiO_2 photocatalysis in recent years. There were a lot of reports for the preparation of TiO_2 thin films on semiconductor substrates such as silicon, as well as on oxide substrates. Various methods of deposition have been applied to grow TiO_2 films. Among these methods, pulsed laser deposition (PLD) is widely used because of the possibility of forming thin oxide films of high quality under reduced oxygen pressures. We have employed the PLD method to obtain TiO_2 thin films on α-Al_2O_3 substrates [2),3)].

Sapphire (α-Al_2O_3) has been used as insulating substrates with high stability and excellent crystal quality. An interesting point of sapphire is to form surface steps in atomic scale by annealing treatment[4]. Our interest is to examine interactions between TiO_2 thin film and the atomic surface steps of sapphire substrate. We expect new film growth phenomena which may relate to new technology on nanoscale titanium dioxide preparation necessary for excellent photocatalysis. In this report, we attempt to reveal variations of surface morphology by annealing and cooling treatments after depositing of TiO_2 thin film on the sapphire. TiO_2 particles of nanosize were arranged on the sapphire substrate with atomic steps, and a model for TiO_2 behaviors arranged on sapphire will be proposed in this report.

All of TiO_2 thin films were deposited on α-Al_2O_3 (0001) substrates by PLD method at 773 K under an oxygen pressure of ~5×10^{-3} Torr. Ti (99.99 %) was used as a target, rotated by a motor at 80 rpm to avoid degradation of target surfaceand to prepare flat films. ArF excimer laser (λ=193 nm) was incident 45° to the target surface. The laser energy was 200 mJ per pulse with repetition of 10 Hz. Thickness of TiO_2 films was measured by surface profiler (Dektak^{3}ST). Crystallographic structure of the films was confirmed by X-ray diffraction method (XRD). Surface observation was carried out using atomic force microscopy (AFM) at tapping mode with a silicon probe. In addition, surface morphology together with element analysis was performed by SEM/EDX (Jeol JSM-5600 and JSM-6700 F).

First of all, we prepared TiO_2 films whose thickness ranges from 5 nm to 30 nm. From the XRD measurement, rutile TiO_2(100) grown on α-Al_2O_3 (0001) was confirmed. This result is consistent with the previous work which claims the highest-quality rutile (100) films on sapphire synthesized by MOCVD and IBSD [5]. The film surfaces of 5-30 nm were observed by AFM. For TiO_2 thin film of 5 nm-thickness, the surface was smooth. In case of TiO_2 thin film of 30 nm-thickness the surface was roughened, and its morphology was not influenced by the atomic steps on substrates because the film was thick enough.

Next, we investigated TiO_2 morphology at elevated temperatures. TiO_2 films of ~5 nm in thickness were employed because drastic change in morphology both by substrate surface and by annealing temperature was expected. Samples were annealed at the temperature of 973~1123 K for 1 hr in air, and subsequently cooled at rate of about 0.1 K/sec. TiO_2 grains become ellipsoidal and their size increased with increasing annealing temperature. As shown in figure 1, when the TiO_2 film was annealed at 1123 K, the major and minor axes of TiO_2 particles were about 50 and 35 nm in width-average,

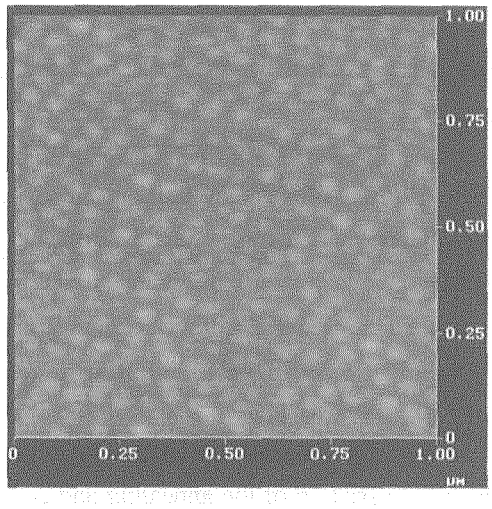

Fig. 1. AFM image of TiO_2 films on c-phase sapphire after annealing of 1123 K for 1 hr in air.

respectively, and their height was 3~8 nm. SEM/EDX characterization of the film shown in figure 1 indicates that the bright image features in AFM are TiO_2 particles. According to the TiO_2-Al_2O_3 phase diagram [6], there is no compounds between TiO_2 and Al_2O_3 below 1420 K. Only a possible compound in the system is Al_2TiO_5. However, the Al_2TiO_5 powder decomposes to Al_2O_3 and TiO_2 below 1453 K [7]. Therefore, any compounds were hardly formed in the rutile-sapphire interface. We also do not have clear evidence on the compound formation. Even in case that the very thin mixed layer is formed at the interface, it must be so unstable that it can be easily decomposed into TiO_2 and Al_2O_3 by annealing treatment.

The reasons why we obtained ellipsoidal or round TiO_2 particles are presumably related to the surface energy minimization, and wettability between TiO_2 and Al_2O_3. In addition, we have expected the other cause associated with morphology change by sapphire substrate surface. Therefore, annealing of only α-Al_2O_3 (0001) substrate without TiO_2 deposition were performed. Figure 2 show the AFM image observed after the annealing treatments at 1173 K for 1 hr in air. Many holes were observed by annealing treatment above 1073 K, probably due to sublimation of Al and O atoms. Narumi et al. reported similar results for the hole formed on sapphire surfaces [8]. Size of the round or ellipsoidal holes formed by annealing at 1173 K was measured from 10 nm to 50 nm in width and 0.2 ± 0.05 nm in depth. At the annealing temperature of ~1273 K, step density increased by a factor of 3-5 (roughly 10 steps/μm). This phenomenon can be interpreted as merging holes along the direction of steps and forming furrows. The holes and furrows on sapphire can work as a good trapping site of Ti or Ti-O during annealing in the TiO_2 deposited on sapphire. Therefore, at the temperature above 1073 K, we consider that TiO_2 particles get together into those holes, resulting in the surface morphology as shown in figure 1.

To investigate formation process of the TiO_2 grains, we carried out quenching of 5 nm in thickness sample after annealing at 1073 K. At the quenching rate of ~100 K/sec, the TiO_2 morphology changed into island structure and round particles. The height of islands (2-5 nm) was about the half of the round TiO_2 particles. At the lower quenching rates (~1.3 K/sec), ellipsoidal, round particles, and triangle-like feature with islands were observed. These results indicate the morphology of TiO_2 on sapphire is quite sensitive to heating treatments.

We propose a following model for the formation process of TiO_2 particles on substrate above 1073 K,

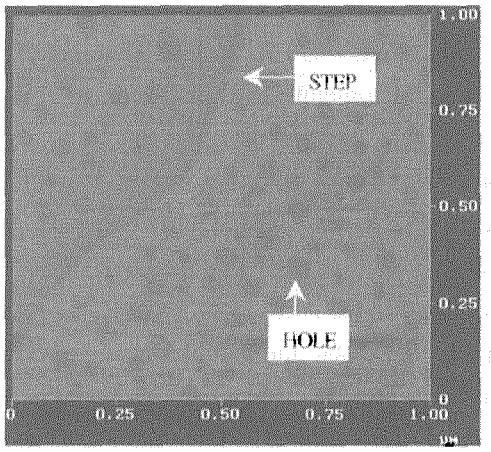

Fig. 2. AFM image of the c-phase sapphire surface after annealing of 1173 K for 1 hr in air.

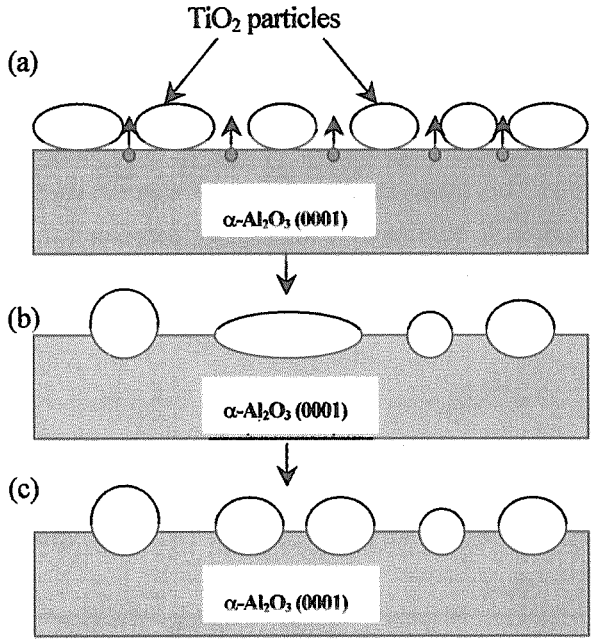

Fig. 3. A proposed model for behavior of TiO_2 particles on the sapphire substrate.

as shown in figure 3. The round TiO_2 particles in figure 1, seem to be formed via processes of figures 3(a)-(c). Since melting point of TiO_2 is lower than that of substrate, and titanium oxide is presumed to be out of stoichiometry consisting of many lattice defects, titanium atoms and Ti-O molecules are rather mobile than Al and Al-O molecules in the substrate. This speculation is possible when the film is very thin (~5nm). Note that in the thick sample (~30 nm), the feature did not appear even though the sample was carried out same treatments. At the temperature over 1073 K, surface Ti atoms or Ti-O molecules agglomerate as Ti-O clusters as shown in figure 3 (a), then sublimation of the substrate becomes significant, resulting in hole-formation on the substrate. Then, diffusing Ti atoms and Ti-O molecules are trapped by the holes, and are accumulated in the holes as TiO_2 particles as shown in figure 3(b). Then, the particles become round or ellipsoidal as shown in figure 3 (b). Some of large ellipsoidal TiO_2 grains decompose into smaller round features as shown in figure 3 (c). This model works at temperature regions where holes were formed on sapphire substrate and TiO_2 particles get together in the holes when the TiO_2 film was thin enough.

In summary, we examined variations of TiO_2 morphology by film-thickness, annealing and cooling treatments using XRD, AFM, and SEM/EDX. We obtained rutile TiO_2 (100) on c-plane sapphire when TiO_2 film thickness was ~30 nm. As film thickness increased, the smooth surface changed to rough structure. In 5-nm-thickness samples, the TiO_2 surface morphology changed drastically by variation of the annealing and cooling treatments. TiO_2 particles were arranged on sapphire at annealing of ~1123 K in the range of 30~50 nm . In addition, TiO_2 particles and island structure such as triangle and chain-like were obtained by cooling rate (~1.3 K/sec) after annealing at 1073 K. We expect that photocatalysts TiO_2 of nanoparticles arranged on sapphire substrates with atomic-height steps can be utilized for fabrications of nanosize structural materials.

References

1) A. Fujishima and K. Honda, Nature **238** (1972) 37.

2) S. Yamamoto, T. Sumita, Sugiharto, A. Miyashita and H. Naramoto, Thin Solid Films **401** (2001) 88.

3) Y. Choi, S. Yamamoto, H. Abe and H. Itoh, Surf. Sci. **499** (2002) 203.

4) M. Yoshimoto, T. Maeda, T. Ohnishi, H. Koinuma, O. Ishiyama, M. Shinohara, M. Kubo, R. Miura and A. Miyamoto, Appl. Phys. Lett. **67** (1995) 2615.

5) P. A. M. Hotsenpiller, G. A. Wilson, A. Roshko, J. B. Rothaman and G. S. Rohrer, J. Crystal Growth **166** (1996) 779.

6) E. M. Levin and H. F. McMurdie, Phase diagrams for ceramists, Vol.III (The American Ceramic Society, Inc. 1975, p135).

7) V. Buscaglia and P. Nanni, J. Am. Ceram. Soc., **81(10)** (1998) 2645.

8) K. Narumi, S. Yamamoto and H. Naramoto, Mat. Res. Soc. Symp. **587** (2000) O8.4.1

5.5 Development of High Performance Buffer Materials -Sorption Mechanism of Europium by Smectite -

Toshihiko OHNUKI*, Naofumi KOZAI**, Shunya YAMAMOTO***, Kazumasa NARUMI*, Hiroshi NARAMOTO*, and Hiroshi ISOBE ****
Avanced Science Research Center, JAERI*, Department of Environmental Science, JAERI**, Dept. of Material Development, JAERI***, Faculty of Science, Kumamoto University****

1. Introduction

Smectite is major mineral contained in bentonite[1], which is a candidate of buffer material of geological disposal[2]. The sorption behaviors of trivalent actinides and lanthanides on smectite have been debatable subjects because of their relevance to potential migration from radioactive wastes to biosphere. We propose the methodology using a thin film of powdered component to clarify the sorption behavior of Eu on smectite. Due to very low solid/solution ratio, use of the thin film has the following advantages: (i) The solution of low Eu concentration can be used in the sorption experiment, (ii) The solution pH is constant during the sorption experiment, and (iii) Decrease of the Eu concentration in the solution is very low. However, if Eu is only sorbed on the surface of the thin film, the sorption behavior of Eu on the thin film may be different from that of the powdered sample.

Rutherford backscattering spectroscopy (RBS) and cyclic voltammetry (CV) techniques are sensitive methods to detect elements[3,4]. The depth profiles of Eu is directly obtained by RBS analyses. Eu sorbed by smectite is detected as current in CV. In the present study, the thin films containing smectite are provided for the sorption experiments. The distribution and mobility of the sorbed Eu in smectite thin film were examined by RBS and CV.

2. Experimental

2.1 Thin films

Smectite ($Na_{0.33}(Si_{3.67}Al_{0.33})Al_2O_{10}(OH)_2$) was obtained from Kunimine Kogyo Co. Ltd., Japan, and originated from Tsukinuno, Japan. X-ray diffraction patterns of the smectite showed that they did not contain measurable impurities.

A 10, 20 or 30 μl solution of 1 g smectite·L^{-1} was placed on a glassy carbon plate. A thin film of smectite was made by drying the above sample for overnight at room temperature. The RBS analysis indicated that the thickness of the thin film was several μm.

2.1 Eu solution

All solutions were prepared with ultrapure deionized distilled water (DDI) water and reagent-grade chemicals. Eu solutions were prepared by diluting a $Eu(NO_3)_3$ stock solution in the DDI water to obtain Eu concentrations of $1.0x10^{-3}$ mol·L^{-1}. The Eu solutions were adjusted to be in pH 4.5 with a 1 M NaOH or 1 M HCl solution.

The thin film was immersed in the 20 ml Eu solution of $1.0x10^{-3}$ mol·L^{-1} for 2 days at 25 °C. After the thin film was separated from the solution, it was washed with the DDI solution, followed by drying for overnight at room temperature. The thin film was not changed after contacting the Eu solution.

2.2 Analysis by RBS

The depth profiles of Eu, Al, Si, Ca, P and O in the thin film were obtained by the 2.0 MeV ^4He RBS system developed in the TIARA facility of JAERI. The beam size of $^4He^+$ ions was approximately 5mm in diameter.

2.3 Cyclic voltammetry

Smectite attached glassy carbon plate was used as working electrode in voltammetry. A Hokuto Denko Co. model HB-101 linear potential scanner was used for the cyclic voltammetry.

After the smectite attached electrode was mounted on the electrolytic cell, 20 ml of electrolyte solution containing $1.0x10^{-3}$ mol·L^{-1} Eu in 0.025 M NaCl solution was taken into the cell. The solution was deaerated by pure argon gas for 15 minutes. The cyclic voltammetry of Eu(III) to Eu(II) was performed. The counter electrode was Pt plate and the reference electrode was a saturated calmel electrode (SCE).

10 and 30 μg smectite were attached to the glassy carbon electrode to examine the effects of thickness of smectite on peak current in cyclic voltammogram. The potential was scanned between –1.2 V and +0.8 V vs SCE at 40 mV/s. Scan rate in cyclic voltammetry was changed between 10 and 100 mV/s to examine the mobility of Eu in the attached smectite.

3. Results and discussion

3.1 RBS analysis of depth profile of Eu in film

Figure 1 shows RBS spectrum of 10 μg fresh smectite thin film. No peaks of heavier elements than Si were detected in RBS spectrum. This indicates that impurities in smectite are below the detection limit of RBS analysis. Figure 2 shows RBS spectra of the 10 and 20 μg smectite thin film contacted with the Eu solution of $1.0x10^{-3}$ mol·L^{-1}. A plateau of Al and Si (major elements in smectite) is observed in the RBS spectrum of the Eu sorbed thin film. The lower energy of the edge of the Al and Si plateau for 20 μg smectite thin film appeared at energy blower than that of 10 μg smectite thin film. This indicates that the larger amount of smectite thin film gave the larger uptake of Eu from the solution to the thin film.

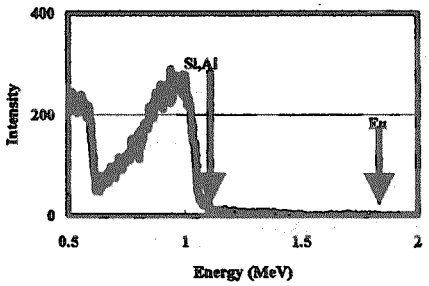

Fig. 1 RBS spectrum of a fresh smectite thin film.

After the RBS measurement the smectite thin film was submerged in the 1 M NaCl solution for overnight at room temperature. Then the RBS analysis was carried out. The RBS spectrum was the same as that of the fresh smectite thin film, indicating that the sorbed Eu by smectite was dissociated from smectite by a 1 M NaCl solution. Thus, Eu is reversibly sorbed by smectite.

3.2 Cyclic voltammetry of Eu

Cyclic voltammograms of Eu(III) at the 10 and 30 μg smectite attached glassy carbon electrode are shown in Fig. 3. Larger amount smectite attached electrode gave higher peak for Eu(III)/Eu(II) current. This indicates that larger amount of smectite sorbs larger amount

of Eu on the smectite thin film. This is in agreement with that obtained by RBS analysis.

3.3 Future plan

XAFS analysis will be carried out to elucidate the chemical species of the sorbed Eu by smectite. Then, the sorption mechanism of Eu by smectite will be clarified.

References

1] T. Ohnuki, N. Kozai, Radiochimica Acta, 68, (1995) 203.

2] R. Push, L. Borgesson, SKB report TR 85-12(1985).

3] T. Ohnuki, N. Kozai, H. Isobe, T. Murakami, S. Yamamoto, Y. Aoki, H. Naramoto., J. Nucl. Sci. Tech., 34, (1997) 58.

4] T. Ohnuki, N. Kozai, H. Isobe, T. Murakami, S. Yamamoto, K. Narumi, H. Naramoto., Radiachim acta., 86, (1999) 161.

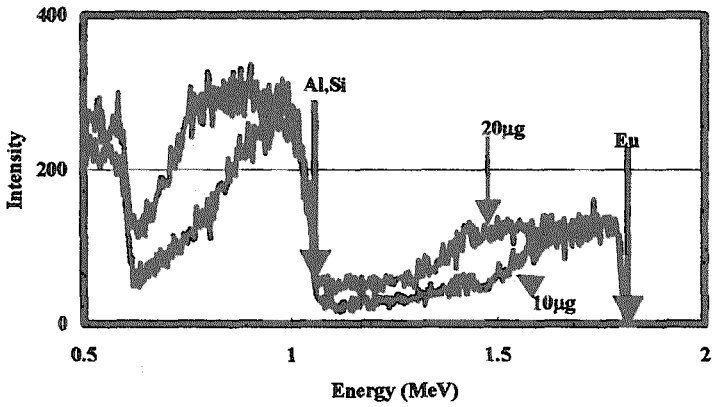

Fig. 2 RBS spectra of the Eu sorbed smectite of 10 and 20 μg thin film.

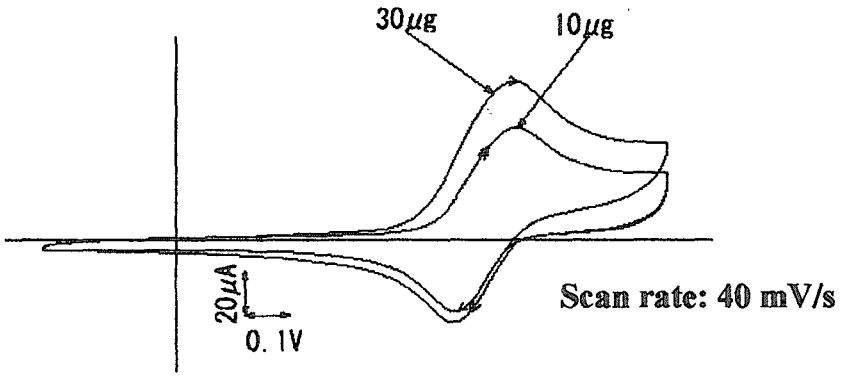

Fig. 3 Cyclic voltammograms of the Eu sorbed smectite attached electrode. The amounts of smectite were 10 and 30 μg.

5.6 Electron Emission from Solids by Fast Cluster Impact

H. Kudo*, W. Iwazaki*, T. Suguri*, Y. Saitoh**, S. Yamamoto***, K. Narumi****, and H. Naramoto****
Institute of Applied Physics, Univ. of Tsukuba*
Advanced Radiation Technology Center, JAERI**
Department of Material Development, JAERI***
Advanced Science Research Center, JAERI****

1. Introduction

Interaction of a fast cluster beam with solids includes correlated impacts (so-called vicinage effects), in other words, physical processes that are characteristic of the projectile with internal atomic structure. This causes radiation effects different from those induced by impact of a single ion or a small molecule. Actually, fast cluster ions in the MeV/atom velocity range give rise to nonlinear radiation effects on solid targets with respect to the number of cluster atoms n. [1-7]

Such nonlinearity has so far been observed for energy loss (stopping power), [1,2] sputtering, [3] lattice damage, [4,5] secondary ion emission, [6] and total electron emission yield (corresponding to the emission current). [7] It is notable that the total electron emission yield per atom depends less linearly on n. This is in contrast to the radiation effects accompanying atomic displacements, i.e., sputtering or lattice damage, for which n-dependence is stronger than linear.

The aim of the present study is to investigate the cluster effect in the ion-induced electron emission. Key information for the cluster-solid interactions will be included in the electron yield possibly at energies lower than ~50 eV, which should reflect soft interactions of the cluster as a whole, rather than of the constituent atoms, with target atoms. A better understanding of the cluster-induced electron emission would provide not only knowledge about the atomic and electronic processes of the cluster impact phenomena, but also an insight into the related effects resulting from energetic cluster-solid interactions. Such basic approach will also be of practical importance for future material processing by cluster impact. In this article, recent progress in the studies and preliminary results are reported.

2. Experiment

The experiments have been carried out using the cluster beam line at the TIARA tandem accelerator. [8] The electron energy spectra have been measured at a backward angle of 135° relative to the beam direction. The equal-velocity beams of C_1^+ and C_8^+, as well as of Au_1^+ and Au_8^+, were used in the experiments.

The beam current was not so stable that the energy analysis by a retarding potential method was unsuccessful. We have therefore modified the parallel-plate electron spectrometer of the double deflection type, previously used for ion-induced spectroscopy of keV electrons. For measurements of the low-energy electrons, the length of the electron orbit in the analyzing electrostatic field of the spectrometer has been reduced to ~20 mm so as to neglect the influence of an external magnetic field in the environments. To increase the electron counting

efficiency, the analyzed electrons were post-accelerated by an electrostatic potential of 600-700 V in front of the electron multiplier.

3. Results and discussion

Figure 1 shows energy spectra of electrons emitted from Ni bombarded by 0.5 MeV/atom C_1^+ and C_8^+. The electron yield was divided by n and was also normalized so that the high-energy sides of the spectra are the same. This is due to the requirement that the high-energy electron yield should result from close encounter of each constituent atom of the cluster with the target electrons. We see from Fig. 1 that the electron yield for C_8^+ at energies lower than 10 eV is suppressed by a factor of ~0.75, compared with that for C_1^+. These data obviously demonstrate the details of the nonlinear cluster effect, i.e., difference in the spectrum shape, which has never been deduced from the measurements of the total electron yield, so far reported.

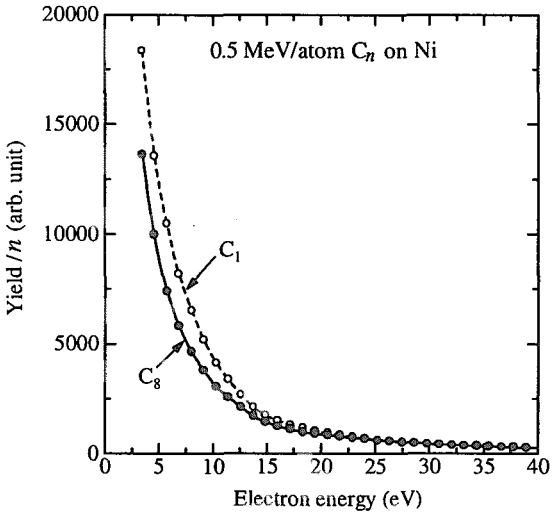

Fig. 1. Energy spectra of electrons emitted from Ni bombarded by 0.5 MeV/atom C_1^+ and C_8^+.

According to the published works.[1,2] the energy loss of a cluster ion is typically greater than n times that of the single ion of equal velocity. It may be anticipated from this fact that the cluster-induced electron emission from a solid target must be enhanced by a factor of greater than n, contrary to the observation which indicates suppression of the electron yield at all electron energies.

To resolve the above difficulty, we refer to the recently reported studies of charge states of cluster fractions.[9-11] Notably, Brunelle and coworkers[9] carried out carbon-foil transmission experiments of 1−4 MeV/atom C cluster ions (n =3−10) and measured the ratio of the average charges (in the equilibrium state) of fragmented clusters to that of a single C ion of equal velocity. They found that (i) for all the clusters the ratio is ~0.8 for thin foils (2.2 μg/cm^2) and approaches to 1 with increasing the foil thickness, and (ii) the ratio is lower for higher values of n of the fragmented cluster. These results indicate that the effective electronic bonds of the cluster still remain in a thin target, which bind the cluster electrons more tightly than when each constituent atom is isolated. Such an effective binding has been confirmed theoretically.[10,11]

These charge-state studies allow to infer possible mechanism of the suppressed electron emission for the cluster impact. Indeed, it is likely that the suppressed electron yield should originate from the released bound electrons of the cluster. There must be a contribution from the ionized target electrons, but the experimental results indicate that this process is less effective. It is worth to note that the suppressed C_8^+-induced yield by a factor of ~0.75 (Fig. 2) corresponds consistently to the reduction of the ratio of the average charges by a factor of ~0.8.

The loss-peak energy, which is the kinetic energy of an electron running at the same speed

as the C cluster, is 22.7 eV. This value can be regarded as the effective upper limit of the energy of the released electrons by the kinetic processes, which is consistent with the experimental results shown in Fig. 1.

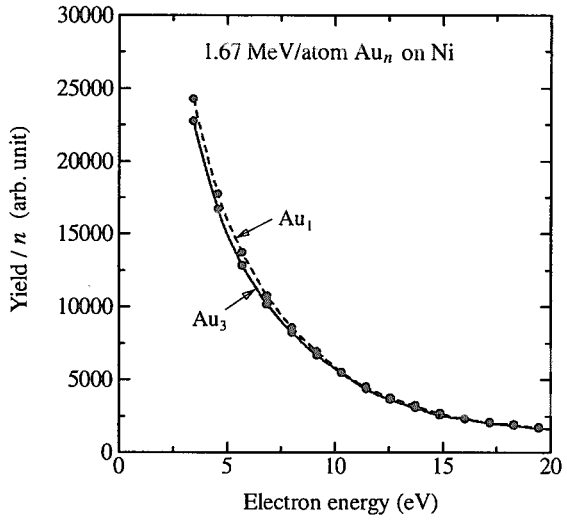

Fig. 2. Energy spectra of electrons emitted from Ni bombarded by 1.67 MeV/atom Au_1^+ and Au_3^+.

Similar experimental results for 1.67 MeV/atom Au_1^+ and Au_3^+ are shown in Fig. 2. In this case, also, the suppressed electron yield is recognized, although the difference in the yield is only slightly larger than the statistical uncertainty (±3%). It should be pointed out that for the Au impact the loss-peak energy is as small as 4.6 eV. This value is less meaningful for a multi-electron atom such as Au since in the present velocity range the attached electrons can possibly be released by the potential emission process.

4. Summary

The energy spectra of low-energy electrons induced by fast cluster ions have been measured. For the cluster impact the electron emission is suppressed compared with the single ion of equal velocity. It is inferred from the published charge state data that the suppressed yield should stem from the collision-induced release of the valence electrons carried by the cluster ion.

It is emphasized that the nonlinear effect in the electron emission seems to have essentially different origins from those associated with atomic displacements. The former results from the electron system of the cluster and, accordingly, must seldom be affected by the correlated atomic impacts such as thermal spikes, as is essential to explain the nonlinear atomic displacements. Further experiments are necessary to study the n-dependence of the suppressed electron yield in relation to the binding energies of the clusters.

References

1) W. Brandt, A. Ratkowski, and R. H. Ritchie, Phys. Rev. Lett. 33 (1974) 1325.
2) K. Baudin, A. Brunelle, M. Chabot, S. Della-Negra, J. Depauw, D. Gardes, P. Hakansson, Y. Le Beyec, A. Billebaud, M. Fallavier, J. Remillieux, J. C. Poizat, J. P. Thomas, Nucl. Instrum. and Methods B 94 (1994) 341.
3) H. H. Andersen, A. Brunelle, S. Della-Negra, J. Depauw, D. Jaquet, Y. Le Beyec, J. Chaumont, H. Bernas, Phys. Rev. Lett. 33 (1998) 5433.
4) M. Döbeli, R. M. Ender, U. S. Fischer, M. Suter, H. A. Synal, D. Vetterli, Nucl. Instrum. and Methods B 94 (1994) 388.
5) H. Shen, et al., Nucl. Instrum. and Methods B129 (1997) 203.
6) A. Brunelle, S. Della-Negra, J. Depauw, D. Jaquet, Y. Le Beyec, and M. Pautrat, K. Baudin, H. H. Andersen, Phys. Rev. A 63 (2001) 022902.
7) M. Fallavier, R. Kirsch, J. C. Poizat, J. Remillieux, J. P. Thomas, Nucl. Instrum. and Methods B 164-165 (2000) 920.
8) Y. Saitoh, K. Mizuhashi, S. Tajima, Nucl. Instrum. and Methods A 452 (2000) 61.
9) A. Brunelle, S. Della-Negra, J. Depauw, D. Jaquet, Y. Le Beyec, and M. Pautrat, Phys. Rev. A 59 (1999) 4456.
10) Z. L. Miskovic, S. G. Davison, F. O. Goodman, W.-K. Liu, Y.-N. Wang, Phys. Rev. A 61 (2000) 062901.
11) J. W. Hartman, T. A. Tombrello, S. Bouneau, S. Della Negra, D. Jaquet, Y. Le Beyec, and M. Pautrat, Phys. Rev. A 62 (2000) 043202.

5.7 Improvement in Surface Roughness of Nitrogen-Implanted Glassy Carbon by Hydrogen Doping II

K. Takahiro*, R. Ookawa*, K. Kawatsura, S. Nagata**, S. Yamamoto***, K. Narumi***, H. Naramoto****

*Department of Chemistry and Materials Technology, Kyoto Institute of Technology**, *Institute for Materials Research, Tohoku University***, *Department of Material Development, JAERI****, *Advanced Science Research Center, JAERI*****

1. Introduction

Ion-implanted glassy carbon (GC) exhibits various structural changes depending on damage accumulated in the implanted layer[1-3]. At damage levels up to 0.2 displacements per atom (dpa), the structure displays a reduction in the average graphitic crystalline size. At damage levels between 0.2 and 3 dpa, the implanted layer begins to transform into an amorphous state. During amorphization approximately 15 % of the graphitic bonds are converted into diamond-like bonds, increasing in density from 1.5 to 2.2 g/cm^3. Furthermore, in case of N-implanted GC, the density of the N-implanted layer is reduced and surface roughening occurs at higher damage levels[4]. Although the mechanism of surface roughening is not well understood, it is indicated that chemical processes are responsible for it. It is of great importance to study irradiation-enhanced surface roughness of GC because it is necessary to have knowledge of wear properties, and adhesion to biological cell/tissue for medical applications such as heart valves and other prosthetic devices.

In the course of the study on surface roughening of N-implanted GC, we have found that the surface roughness depends on a vacuum during implantation. The N implantation in the better vacuum produces the rougher surface. Characterization of the N-implanted GC reveals that a significant amount of hydrogen atoms exists in the implanted layer when implanted in the poor vacuum. Therefore, the hydrogen incorporation may play an important role to prevent surface roughening. In the present work, we study the effect of hydrogen incorporation on surface roughening induced by N implantation. For this purpose, hydrogen atoms are doped by ion implantation prior to N implantation.

2. Experimental procedures

The glassy carbon (GC-30 grade) plates used were supplied from Tokai Carbon. They were cut into 1×0.5×0.1 cm^3 and were polished to mirror surface using 1 μm diamond slurry on a cloth lap. The GC samples were implanted with 10 keV D_2^+ ions to a dose of 6×10^{17} D$^+$/cm^2, corresponding to the D concentration of approximately 30 at. %. The un-doped and the D-doped GC were simultaneously implanted with 100 keV N_2^+ up to a dose of 12×10^{17} N$^+$/cm^2 at temperatures below 100 °C. A vacuum during N implantation was better than 2×10^{-5} Pa. The projected ranges of 10 keV D_2^+ and 100 keV N_2^+ were calculated by the TRIM code[5] to be ~90 nm and ~120 nm, respectively, assuming the density of GC to be 2.0 g/cm^3. Surface morphology of the ion-implanted GC was observed by means of scanning electron microscopy (SEM). Depth distributions of D and H atoms were measured by elastic recoil detection (ERD) analysis using a 2.8 MeV $^4He^{2+}$ beam. Depth distributions of N atoms were measured by the ion backscattering spectrometry (BS) using a 3.5 MeV $^4He^{2+}$ beam. X-ray photoelectron spectroscopy (XPS) by Mg $K\alpha$ excitation ($h\nu$=1253.6 eV) was used to analyze chemical bonding of the ion-implanted layer. Raman spectroscopy using an argon-ion laser with excitation wavelength of 514.5 nm was also applied to the samples to characterize the ion-implanted layers.

3. Results and discussion

Figure 1 (a) shows the SEM micrograph taken from the as-polished GC. Collapsed micro-pores of ~3 μm size and many polishing scratches can be seen. Figure 1 (b) is the photograph taken from the un-doped GC after implantation with 100 keV N_2^+ to a dose of 4×10^{17} N$^+$/cm^2. This dose is ~20 times as high as the dose at which the N-implanted layer is amorphized. The amorphization will be confirmed later by Raman spectroscopy. Remarkable surface roughening, which originates in polishing scratches, occurs after N implantation to 4×10^{17} N$^+$/cm^2. The polished surface may be strained, especially along polishing scratches. It is considered that this strain roughens the surface after N implantation. Above this dose, however, enhancement in roughness was not observed. For the D-doped GC samples, surface roughening due to N implantation was not recognized at 4×10^{17} N$^+$/cm^2 as shown in Fig. 1 (c). The smooth surface

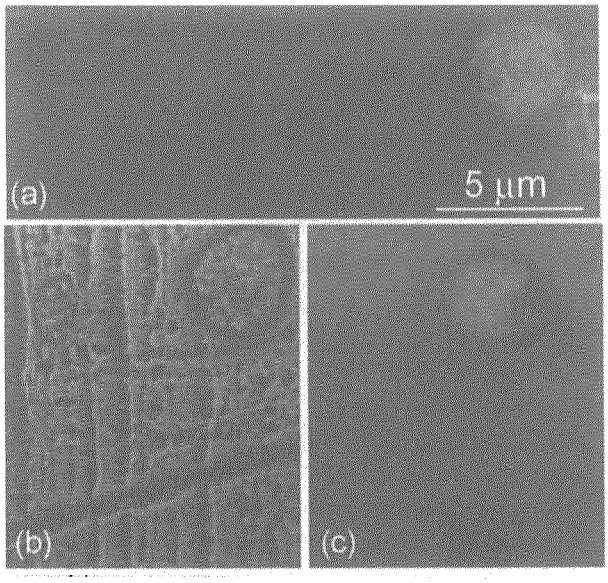

FIG. 1. SEM micrographs of GC surfaces before (a) and after 100 keV N_2^+ implantation to a dose of 4×10^{17} N^+/cm^2 for un-doped GC (b) and D-doped GC (c).

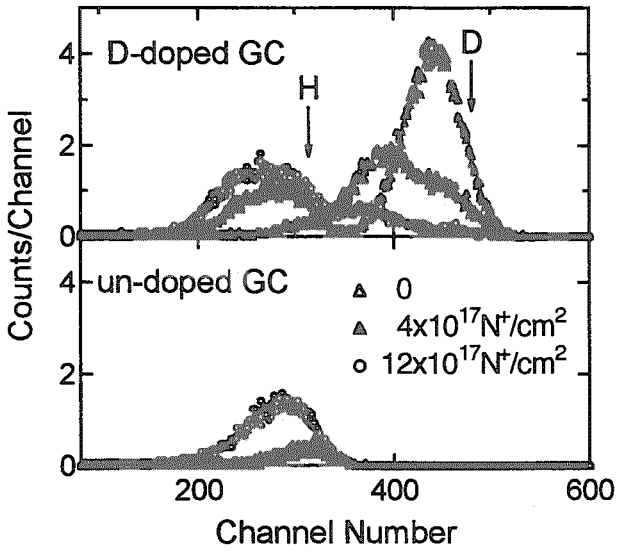

FIG. 2. ERD spectra of the un-doped GC and D-doped GC implanted with 100 keV N_2^+.

was obtained up to 12×10^{17} N^+/cm^2 for the D-doped GC, indicating that D doping successfully suppresses surface roughening.

For the N profiles in BS spectra (not shown here) for the un-doped and the D-doped GC with N implantation, the flat-topped appearance indicates that a saturation of N concentration takes place in the nitride layer. The saturated N concentration for the D-doped GC is 25 at. % similar to that for the un-doped GC. The shape of the N profile for the un-doped GC is somewhat roundish because the surface of the un-doped GC is roughened after N implantation. Figure 2 shows ERD spectra of the D-doped GC implanted with 100 keV N_2 ions at various doses. Before N implantation, the maximum D concentration was approximately 30 at. %, corresponding to saturated concentration of hydrogen in graphitic materials. A part of the implanted D atoms was released by N implantation, but hydrogen atoms, probably coming from atmosphere in the implantation chamber, were absorbed instead. As a result, total concentration of hydrogen including D and H atoms in the N-implanted layer exceeds 20 at. % at any doses. As described above, the surface morphology of the D-doped GC is unchanged even after high-dose N implantation. We conclude, therefore, that the hydrogen atoms in the N-implanted layer improve the surface roughness.

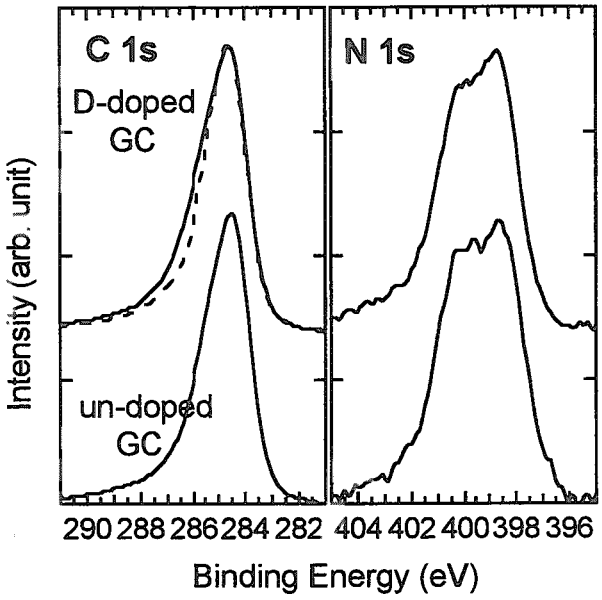

FIG. 3. XPS spectra of C 1s and N 1s lines for the D-doped GC (upper part) and the un-doped GC (lower part) after N implantation to 4×10^{17} N^+/cm^2. XPS spectrum of a C 1s line for the D-doped GC before N implantation (broken line) is also shown for comparison.

Next we examine chemical bonding in the N-implanted layer for the un-doped GC and the D-doped GC after N implantation to a dose of 4×10^{17} N^+/cm^2. Figure 3 shows XPS spectra from the N-implanted GC for C 1s and N 1s states. The C 1s binding energy and the line width for the D-doped GC before N implantation are 284.6 eV and 2.0 eV, respectively, very close to those for an amorphous hydrogenated carbon. The C 1s binding energy for the D-doped GC is unchanged after N implantation, and nearly the same as that for the un-doped GC with N implantation (284.5 eV). The C 1s spectrum for the D-doped GC becomes broader at ~287 eV after N implantation. Such a broadening could arise from the formation of C-N bonds in the D-doped GC. Furthermore, the width

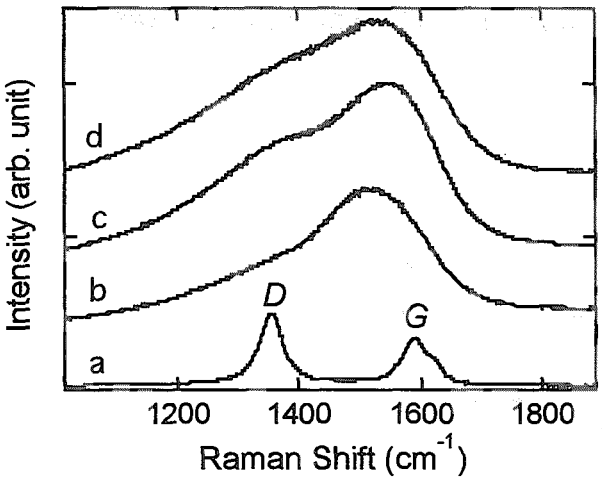

FIG. 4. Raman spectra for the as-polished GC (a), the D-doped GC (b), the D-doped GC after N implantation (c) and the un-doped GC after N implantation (d). N mplantation dose is 4×10^{17} N^+/cm^2.

of the C 1s line for the D-doped GC with N implantation is slightly (~10 %) larger than that for the un-doped GC, suggesting that the N-implanted layer in the D-doped GC contains C-D and/or C-H and C-N bonds. In Fig. 3, the shape of N 1s line for the D-doped GC is very similar to that for the un-doped GC. This means the similarity of the atomic configuration around N atoms. Therefore, N atoms implanted in the D-doped GC are most likely to favor the formation of C-N bonds. Thus XPS analysis reveals that chemical bonding in the N-implanted layer for the D-doped GC is quite similar to that for the un-doped GC. In both GC samples, the N atoms implanted may be substituted into aromatic rings[6].

Figure 4 shows Raman spectra obtained from the as-polished GC and the ion-implanted GC. N implantation dose is 4×10^{17} N^+/cm^2. The spectrum of the as-polished GC consists of an intrinsic graphite *G* peak at 1588 cm^{-1} and a disorder-induced *D* peak at 1352 cm^{-1}. For the ion-implanted GC, the spectrum exhibits a broad peak, which is a typical spectrum for an amorphous carbon, although its shape depends on the ion implanted. We investigated the change in the shape by decomposing the spectrum into two Gaussians. The *G* position for two kinds of the N-implanted GC (with and without D-doping) is approximately 1560 cm^{-1}, significantly lower than the intrinsic graphite *G* peak, indication of bond-angle disorder in the materials. The I_D/I_G peak height ratio is a measure of the size of graphitic layer L_a in an amorphized carbon with L_a less than 2 nm[7]. The larger I_D/I_G ratio, the larger size L_a. In the present results, the size of the graphitic layers, that is the number of aromatic rings, in the D-doped GC is found to be smaller than that in the un-doped GC after N implantation.

In XPS and Raman analysis, a clear difference in the structure of the N-implanted layer between the un-doped and the D-doped GC is the size of the graphitic layers. For the D-doped GC, the aromatic rings are terminated by D or H atoms, which may result in smaller size of graphitic domain. We consider that the graphitic layers partly (~1/3) substituted by N atoms should be stressed because of a difference in a bond length between C-C and C-N in the aromatic rings[6]. As seen in the SEM micrograph for the un-doped GC after N implantation (Fig. 1 (b)), the surface roughening occurs at polishing scratches, where a strain is likely to be introduced. We speculate, therefore, that the stressed graphitic layers containing N atoms at the polished scratches could burst up the surface. While for the D-doped GC, the smaller size of graphitic layers containing N atoms could relax the stress, and no significant surface roughening occurs.

4. Summary

It has been demonstrated that the hydrogen doping (~30 at. %) is an effective method to obtain a smooth surface of N-implanted GC. A part of the doped hydrogen atoms is released by N implantation, but hydrogen incorporation occurs simultaneously. Consequently, concentration of hydrogen in the N-implanted layer exceeds 20 at. % at any N implantation doses. XPS and Raman analyses reveal that chemical bonding in the N-implanted layer for the D-doped GC is quite similar to that for the un-doped GC, but the size of graphitic layers containing N atoms is different. The smaller size of the graphitic layers could relax the strain introduced at polishing scratches, which keeps the surface smooth.

References

1) D. McCulloch, S. Prawer, A. Hoffman and D. K. Sood, Nucl. Instr. Meth. B **80/81**, 1480 (1993).
2) D. McCulloch, A. Hoffman, S. Prawer, J. Appl. Phys. **74**, 135 (1993).
3) D. McCulloch, S. Prawer, A. Hoffman, Phys. Rev. B **50**, 5905 (1994).
4) S. P. Withrow, J. M. Williams, S. Prawer and D. Barbara, J. Appl. Phys. **78**, 3060 (1994).
5) J. F. Ziegler, J. P. Biersack and U. Littmark, "The Stopping and Ranges of Ions in Solids" Vol. 1 (pergamon Press, New York, 1985).
6) A. R. Merchant, D. G. McCulloch, D.R. McKenzie, Y. Yin, L. Hall and E.G. Gerstner, J. Appl. Phys. **79**, 6914 (1996).
7) A. C. Ferrari and J. Robertson, Phys. Rev. B **61**, 14095 (2000).

5.8 In-situ Analysis on Adsorption and Desorption of Atoms at Liquid-Solid Interface by Use of Rutherford Backscattering Spectroscopy

J. Yuhara*, H. Suzuki*, K. Soda*, K. Morita*,
S. Yamamoto**, K. Narumi***, H. Naramoto***, and K. Saito****
Graduate School of Engineering, Nagoya University*,
Department of Material Development, JAERI**,
Advanced Science Research Center, JAERI***
AIST Chube****

1. Introduction

It is important to understand the fundamental processes of the adsorption and desorption of atoms at the interface between the liquid and the solid for the technology of the geologic radioactive waste disposal. In order to *in situ* analyze the concentration of the adsorbates at the liquid-solid interface, we have developed a method with use of Rutherford backscattering spectroscopy (RBS)[1,2], and successfully measured, as an example, the dissolution rates of Pb atoms, deposited on the SiO_2 surface, into solutions with different pH values[3]. On the other hand, the formation of Cu, Ag or Pb "islands" on Si due to beam-solution interactions was suggested by Forster *et al.*[4]

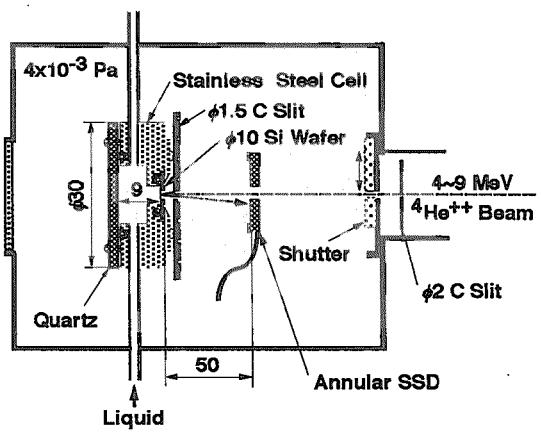

Fig.1 Experimental apparatus for *in-situ* RBS analysis of adsorbates at liquid-solid interface.

In this report, we will briefly describe the experimental results on the adsorption of some metals from their solutions and the key issue for improving the detection efficiency.

2. Experimental procedure

The experimental apparatus is schematically shown in Fig.1. In the present study the analyzing cell was filled with 0.1 M solutions of $AgNO_3$, $Nd(NO_3)_3$, or $Pb(NO_3)_2$. The amount of the metals adsorbed at the naturally oxidized surface of a Si(100) substrate was measured through a 3 ~ 5 μm thick window of the substrate by RBS with a 9 MeV $^4He^{2+}$ ion beam.

3. Results and Discussion

Typical RBS spectra are summarized in Fig.2, where each spectrum is enlarged in the region of the channel number higher than 550 by an indicated magnification factor.

Figure 2(a) shows the RBS spectrum recorded after the cell was filled with water. Spectral feature between the channel numbers 400 and 520 is due to the Si thin window on the substrate. It shows fine structures caused by nuclear reaction. Elements observed on the front side of the window, from which the probing ion beam was incident, are indicated by symbols with the subscript f.

Figures 2 (b), (c) and (d) show the spectra recorded 3-4 hours later from the injection of 0.1 M solutions of $Nd(NO_3)_3$, $Pb(NO_3)_2$ and $AgNO_3$, respectively. The growth of a peak due to Ag adsorbates was observed around the channel number 670, as seen in the spectrum (d). On the other hand, no remarkable feature is recognized for $Nd(NO_3)_3$ and $Pb(NO_3)_2$, although the signals slightly increase for the channel number larger than 600, compared with the spectrum (a). Thus we have shown the applicability of the *in situ* RBS analysis to the precipitation process. However, we could not confirm the suggested Pb "islands" formation. This may be partly because the Nd and Pb features are smeared out by the poor resolution in the present study.

The amount of the Ag adsorbates is estimated from the peak area to be 4.1 x 10^{16} atoms cm^{-2} for the spectrum (d). This is about 100 times as large as the detection limit of ~10^{14} atoms cm^{-2} we have intended. The reduction in the background and the increase of the energy resolution will improve the detection limit and efficiency.

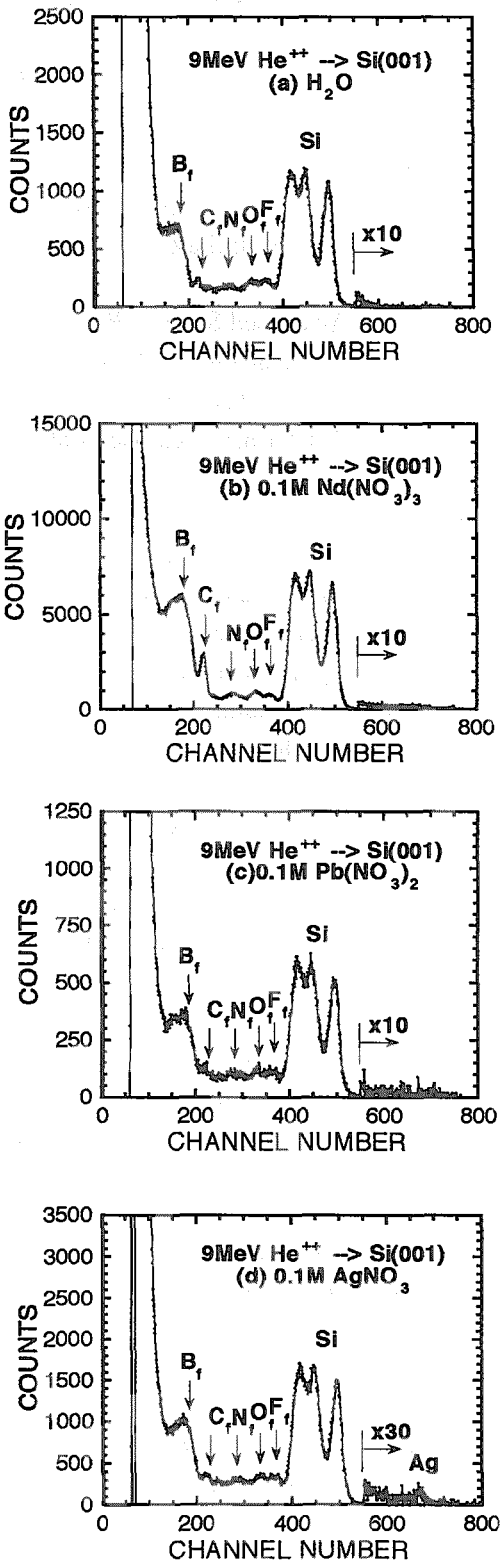

Fig.2 Typical RBS spectra recorded 3-4 hours later from the injection of 0.1 M $Nd(NO_3)_3$ (b), $Pb(NO_3)_2$ (c), and $AgNO_3$ solutions (d) in comparison with the case of H_2O injection (a).

References

1) K. Morita, J. Yuhara, R. Ishigami, B. Tsuchiya, K. Soda, K. Saitoh, S. Yamamoto, P. Goppelt-Langer, Y. Aoki, H. Takeshita, & H. Naramoto, Rad. Phys. and Chem. 49 (1997) 603-608.

2) J. Yuhara, N. Kishi, H. Suzuki, K. Soda, K. Morita, T. Ohnuki, S. Yamamoto, K. Narumi, H. Naramoto, & K. Saito, JAERI-Review 2001-039 (2001) 210-211.

3) K. Morita, J. Yuhara, R. Ishigami, B. Tsuchiya, K. Soda, K. Saitoh, T. Ohnuki, S. Yamamoto, Y. Aoki, K. Narumi, & H. Naramoto, *to be published.*

4) J.S. Forster, D. Phillips, J. Gulens, D.A. Harrington, & R.L. Tapping, Nucl. Instrum. Meth. **B28** (1987) 385-390.

5.9 Percolation of Liquid Indium through Porous Media Composing of Ni and C_{60}

Hiroshi Naramoto, Jiri Vacik*, Kazumasa Narumi, Kiyoshi Miyashita+, and Yoshikazu Honma◆

Advanced Science Research Center, Japan Atomic Energy Research Institute
Nuclear Physics Institute, Rez near Prague, Czech Republic*
Gunma Prefecture Industrial Technology Research Laboratory+
NTT Basic Research Laboratory◆

1. Introduction

The mixtures between immiscible elements and the super-saturated substances are susceptible for energetic disturbances, and the spontaneous structure evolution can be realized reflecting on the nature of the applied influences. Especially, the highly organized structures formed through the competition between the agglomeration and the chemical reactions in the mixture of transition metal elements (Ni, Co) and C_{60} have attracted much interest as nano-functional materials[1-3]. The structures obtained cannot be controlled easily, and it is important to explore the limited condition through the *in-situ* observations. In the present study, the percolation of liquid indium in meso-porous medium, the mixture of Ni and C_{60} are reported based on the *in-situ* observations at high temperatures with scanning electron microscope (SEM) and optical microscope (OM).

2. Experimentals

The mixed and/or layered films between Ni and C_{60} were prepared on MgO(100) at room temperature under 10^{-8} Torr by operating two different evaporation sources independently. The deposition rate of C_{60} was controled by changing the temperature of Knudsen cell but the rate for nickel was not controlled because nickel was evaporated by electron bombardment. The source materials for C_{60} and Ni are relatively high quality with 99.99 % purity. The chemical state of the prepared films was characterized by micro-Raman spectrometer equipped with an AFM stage (Nano-finder) and X-ray diffractometer. In the *in-situ* observations with scanning electron microscope (SEM) and optical microscope, a comparison was made on the percolation behaviors of liquid indium in between pristine and ion-irradiated areas. Especially for the SEM observation at high temperatures, a specially designed UHV-SEM was used which was developed in NTT Basic Research Laboratory.

3. Results and Discussion

The co-deposited films at room temperature are granular and meso-porous with the basic structure of Ni fine particles coated by carbon allotropes. The meso-porous structure can be realized more easily with the increasing fraction of C_{60} molecules, and it is interesting to control the interface properties of meso-pores through the conversion of carbon allotropes by the energetic ion bombardments.

A small chip of solid indium with 99.9999% purity was placed on the pristine area of the meso-porous films and the *in-situ* observation of surface was performed with the low heating rate (~5K/min). Even if after melting at 431K, liquid indium kept the round shape up to around 670K with only slight expansion. But after approaching to 670K, the drastic change was observed. The liquid indium started to

expand at the high speed in a discontinuous manner, which resulted in the concentric pattern. A scanning electron micrograph in Figure 1 was taken at 670K under UHV condition, which contrasts the percolation behaviors of liquid indium in between the pristine region and the irradiated region with 7MeV $^{12}C^{2+}$ ions up to 5×10^{17} cm^{-2}. In the pristine region, one can see the trace of discontinuous flow of liquid indium, and once the liquid indium encounters the impeding barrier for the percolation (irradiated area with non-porous nature) the liquid indium changed into solid even if the temperature was kept to be the same. It can be explained by the phase transition of super-cooled liquid alloy between indium and nickel that was formed during the percolation in the pristine area. In the following the rather detailed description will be given on the spontaneous structure formation both in the pristine and irradiated region.

Figure 2 depicts typical different two modes of the percolation found in the pristine region. The radial stripes are formed during the waiting time for collapsing of small indium droplets into big ones for further progress. Figure 2(a) shows an example of simple percolation expanding into the outer region from the center, and one can observe the "coral-structure" formed through attack by the reactive indium liquid. The radial stripes are formed during the waiting time for collapsing of small droplets into big ones for further progress. The cellular structure in Figure 2(b) is realized when successively percolating indium droplets from an indium reservoir can solidify along the same tangential line and they form series of cells, which could become important and general process for the self-organized structure with the stratified nature by employing the percolation behavior of liquid.

As described already, the liquid indium solidified immediately after receiving the colliding shock. Figure 3 illustrates the typical topological features at the front end of flooded indium. One can find the appearance of micron-sized wires just like "mushrooms" stemmed from the flooded ground. This appearance was completed within about 10 seconds during the *in-situ* observation, which can be explained by highly supercooled indium liquid by introducing the nickel atoms as alloying element when the percolation. The Auger electron spectrometric analysis shows the following distribution features: nickel impurities are concentrated at the top of "mushroom". The carbon precipitates with a few 10's nm are in the outer peripheral layer.

The observed phenomena here were observed only in the films with nickel atoms as a mixture element or as a base. But the liquid indium on nickel films did not induce any discontinuous percolation behavior. So, it can be said that the percolation observed here is related to two-dimensional nature of liquid indium on the nickel base. It is suggestive to utilize the percolation process of reactive liquid for designing materials with the intended structure under the suitable combination of percolation mechanisms. The percolation includes the redistribution of incorporated impurities with the structure evolution. The ion bombardments could take an important role in this study for preparing the regular arrangement of percolation barriers to control the distribution of micron wires, for example.

References:

[1] J. Vacik, H. Naramoto, K. Narumi, S. Yamamoto and K. Miyashita, J. Chemical Physics 114 (2001) 9115-9119.

[2] H. Naramoto, X. D. Zhu, J. Vacik, Y. H. Xu, K. Narumi, S. Yamamoto and K. Miyashita, Phys. of the Solid State 44 (2002) 668-673.

[3] V. I. Lavrentiev, H. Abe, S. Yamamoto, H. Naramoto and K. Narumi, Physica B: Condensed Matter (2002), in print.

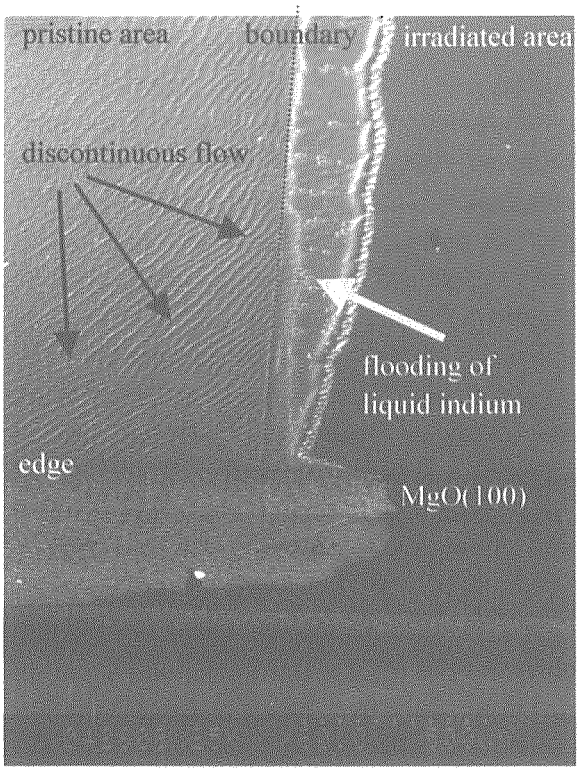

Fig. 1: *In-situ* observation of percolating liquid indium with UHV-SEM. The small dot of indium metals was placed on the pristine area on the left, and then heated up at the rate of ~5°C under ultra high vacuum or He gas.

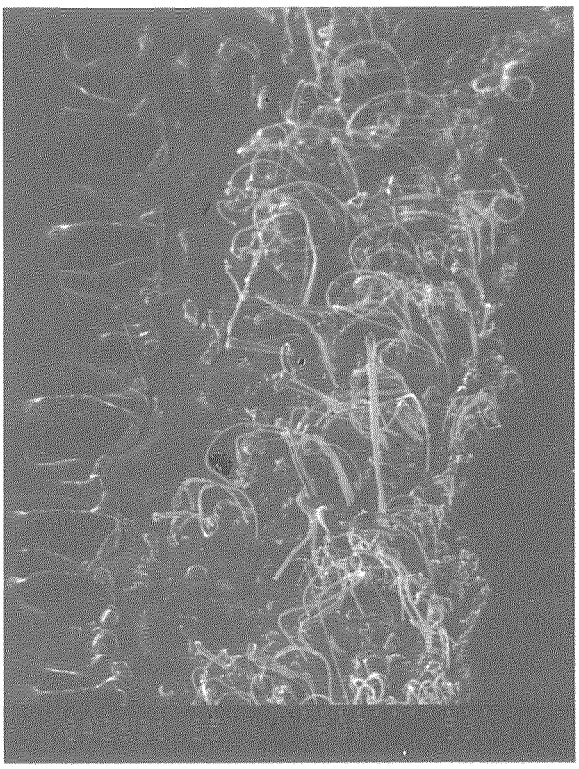

Fig. 3: Enlarged photograph of Fig. 1 from the flooded front in the ion-irradiated region with 7MeV $^{12}C^{2+}$ ions up to 5×10 $^{16}/cm^2$. The wire-like "mushrooms" appeared immediately after colliding with the irradiated, non-porous area.

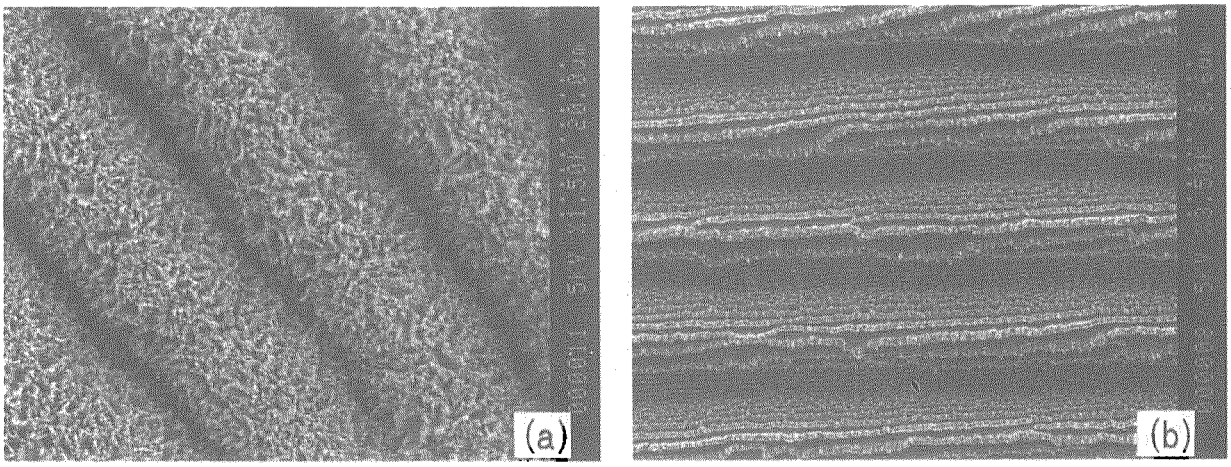

Fig. 2: SEM micrographs of traces of percolated liquid indium. (a) for the simple percolation expanding from the center to the outer area without indium reservoir. (b) for the complicated percolation along the tangential line of concentric circle with indium reservoir. Indium droplets percolate successively on the circumference and solidify in order leaving the regular cell structure behind.

5.10 AFM Observation of Nano-sized SiC Dots Prepared by Ion Beam Deposition Method

Y. Xu*, K. Narumi*, K. Miyashita**, and H. Naramoto*
Advanced Science Research Center, JAERI*,
Gunma Prefecture Industrial Technology Research Laboratory**

1. Introduction

Silicon carbide (SiC) is an attractive semiconductor material due to its excellent thermal stability and electrical properties[1, 2]. SiC light-emitting diodes (LEDs) are also great interesting optoelectronic devices due to its wide band-gap nature[3, 4]. However, because of the intrinsic indirect band gap character, the quantum efficiency of the SiC LEDs reported so far is still as low as about 10^{-4}.[5] It is well known that indirect-gap semiconductor materials also can show the character of direct optical transition when the particle size decreases to the nano-scale attributed to quantum confinement effect. In fact, it has been reported that such effect might exist in porous SiC or nano-crystalline SiC[6, 7]. In the present study, mass-selected ion beam deposition (MSIBD) method is employed to prepare nano-sized SiC dots in a controllable way, and the features of particle assembling are discussed based on the AFM characterization.

2. Experiments

In the low energy MSIBD system used in this research, first, ions were generated through CO_2 plasma in ion source, then extracted from the ion source with a bias and accelerated to 7 keV. Only $^{12}C^+$ was selected to pass through the mass selected magnet. Just before reaching Si substrate, $^{12}C^+$ ions were decelerated down to 100 eV. That is, the deposition energy is 100 eV. Sb-doped Si(111) wafers with low resistance (approximately 1.0×10^{-2} Ω·cm) were used as substrates. The wafer surface was misoriented to [1 1 2] by about 4°. Before the deposition, the substrates were ultrasonically cleaned with acetone and ethanol, and then careful heat treatment was performed under UHV condition (base pressure 2×10^{-9} Torr). Substrates were out-gassed at about 650°C for more than 10 hours at first, and then cleaned by flashing at 1250°C. From RHEED observation, 7×7 reconstructed structure was confirmed. The deposition temperature was set at rather high temperatures in the range of 800 to 950°C using the direct current heating method. The sample temperatures were monitored with an infrared pyrometer.

The deposited films were characterized by Raman spectroscope and XPS spectrometer. The surface and size characters were analyzed by an atomic force microscope (AFM).

3. Results and Discussion

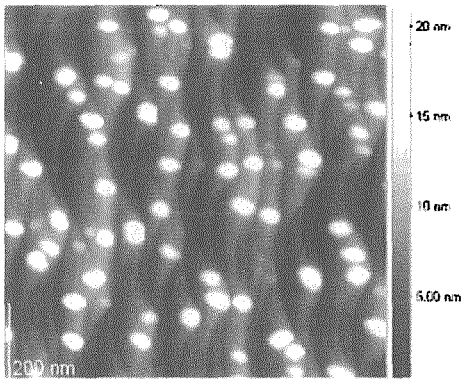

Figure 1 AFM image of an IBD sample prepared at 850°C on the high temperature flashing treated Si(111).

Figure 1 is an AFM image of an IBD sample deposited at 850°C. It shows that each step, which is clearly observed on the misoriented Si(111) substrates after 1250°C flashing treatment, becomes quite meandering. The wavy shape is considered to be relevant to the deposited carbon atoms and the high temperature, because this shape is observed only after the carbon-ion-deposition at high temperature. In addition, nano-sized dots are found at the top of wavy steps.

To identify the chemical condition of carbon atoms deposited by IBD at high temperature, we measured XPS spectra in the sample prepared at 850°C. The size of the probing beam is around 60 μmϕ. As shown in Fig. 2, a peak of silicon (2p) binding energy at 100.8 eV appears. This indicates that Si-C bond is formed in the IBD sample. This result is consistent with the result reported by Zhang[8], that is, SiC can be formed in C-implanted Si substrates by post-annealing treatment at temperatures above 400°C. At the same time, Si-Si bond and Si-O bond, corresponding to peaks of 99.2 eV and 103.3 eV at XPS, respectively, are also observed. This result means that the surface is not covered by SiC entirely. Therefore, it is reasonable to consider that the nano-sized dots are SiC.

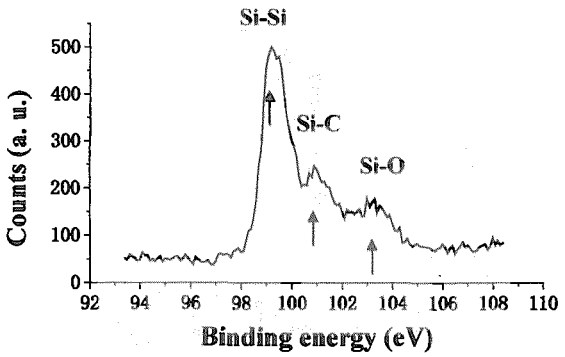

Figure 2 XPS spectrum of an IBD sample prepared at 850°C.

IBD samples were also prepared at different temperatures on Si(111) treated by high temperature flashes. As shown in Fig. 3, at the deposition temperature of 800°C, the dots were formed on the step-edge, and self-assembled on the lines along the steps; while, at higher deposition temperatures, the step shape of substrates changed to meanderine and rough, and the linear arrangement disappeared.

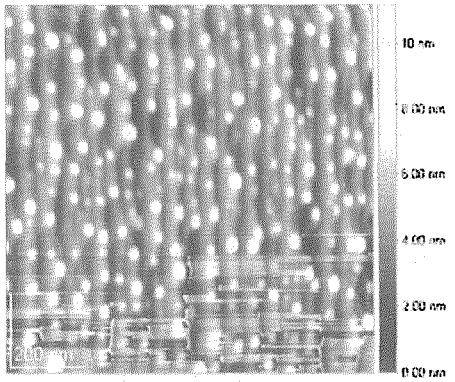

(a) 800°C

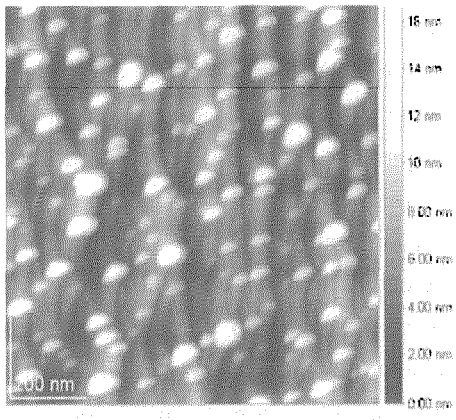

(b) 900°C

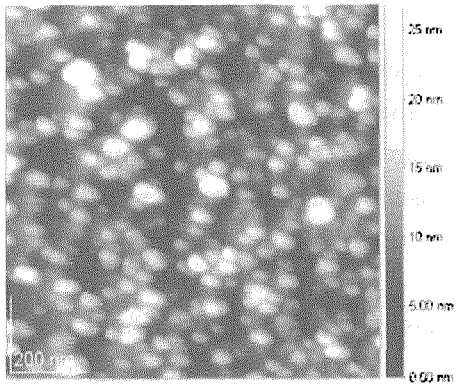

(c) 950°C

Figure 3 AFM images of IBD samples prepared at (a) 800°C, (b) 900°C, (c) 950°C, on Si(111) substrates treated by high temperature flashes.

For the convenience of discussion, the size distributions of SiC dots of samples discussed in Fig. 3 are summarized in Fig. 4. It is shown that the dot-sizes in samples deposited at 800 and 850°C are about 10 to 40 nm and 40 to 60 nm, respectively. However, at 900 and 950°C, a lot of dots smaller than 20 nm were formed, while some dots are larger than the step width, which is about 50 nm. Hence, the size distribution becomes very broad.

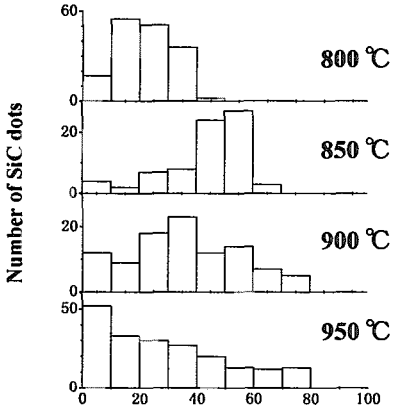

Figure 4 Size-distribution of SiC dots prepared by IBD at high temperatures.

In conclusion, in this research, nano-sized silicon carbide (SiC) dots were grown by low energy mass-selected ion beam deposition (MSIBD) on 4°-off Si(111) substrates at temperatures from 800 to 950 °C, and were analyzed by an atomic force microscope (AFM). We find that the size distribution and the geometrical arrangement of SiC dots strongly depend on the substrate temperatures. That is, highly uniform SiC dots are formed at 800°C and 850°C; especially, SiC dots are arranged on step edge lines when the deposition temperature is as low as 800°C. These results indicate that self-assembled SiC dots can be prepared on misoriented substrates at low deposition temperatures.

Reference:

1) Properties of Silicon Carbide, ed. by G. L. Harris (INSPEC, London, 1995).
2) L. S. Rea, Mat. Res. Soc. Symp. Proc. 423 (1996) 3.
3) X. L. Wu, G. G. Siu, M. J. Stokes, D. L. Fan, Y. Gu and X. M. Bao, Appl. Phys. Lett. 77 (2000) 1292.
4) J. S. Shor, L. Bemis, A. D. Kurtz, I. Grimberg, B. Z. Weiss, M. F. Macmillian and W. J. Choyke, J. Appl. Phys. 76 (1994) 4045.
5) L. Hoffman, G. Ziegler, D. Theis and C. Weyrich, J.Appl. Phys. 53 (1982) 6962.
6) S. J. Xu, M. B. Y. Rusli, S. F. Yoon and C. M. Che, Appl. Phy. Lett., 76 (2000) 2550.
7) A. O. Konstantinov, A. Henry, C. I. Harris and E. Janzen, Appl. Phys. Lett. 66 (1995) 2250.
8) Z. Zhang, H. Naramoto, A. Miyashita, B. Stritzker and J. K. Lindner. Phys. Rev. B 58 (1998) 12652.

5.11 Encapsulated Structure in Co-C_{60} System

V. Lavrentiev*, H. Naramoto*, K. Narumi*, S. Yamamoto**,
H. Abe*** and K. Miyashita****
Advanced Science Research Center, JAERI*,
Department of Materials Development, JAERI**,
Nuclear Eng. Research Laboratory, The University of Tokyo***,
Gunma Pref. Industrial Tech. Research Laboratory****

1. Introduction

The assemblies of small ferromagnetic particles separated by non-magnetic material attract a great interest because of unique opportunity to get a system with extraordinary magnetic properties [1]. During several last years this idea has been successfully developed in Co-C system under the desire to create promising material for application in high-density recording media. Thus, a formation of Co-C compositions by arc-discharge and sputtering techniques based on immiscibility of the mixed components yields an encapsulated structure as Co nano-particles covered by graphitic layers [2-8]. Here we report a realization of encapsulation in Co-C_{60} system during deposition of thin films with mixed composition. Good quality (smoothness, adhesion) and reproducibility of the realized films imply promising method available for practice.

2. Experimental Procedures

2.1 Thin film preparation

Mixed Co+C_{60} films were grown up to 200 nm in thickness on (0001) α-Al_2O_3 as a result of simultaneous deposition (co-deposition) of the components under 10^{-5} Pa. Co-deposition was executed using two different crucibles in the same vacuum chamber by electron bombardment onto cobalt (99.9 mass. % Co) and thermal sublimation of C_{60} (99.9 mass. % C_{60}). The temperature of (0001) α-Al_2O_3 substrate was varied in the range from 25°C (room temperature) to 400°C. To study the mixture films by transmission electron microscopy (TEM) co-deposition has been also performed on (001) NaCl at room temperature. For TEM experiments film thickness was varied from 10 to 100 nm. The deposition parameters were chosen so as to achieve a Co:C atomic composition of 2:1 in the mixture. As referred samples the pure Co and C_{60} films were additionally prepared under the same experimental conditions.

2.2 Experimental Techniques

The surface morphology of deposited films was studied by atomic force microscopy (AFM) using JSPM-4200 scanning probe microscope. The phase and structure analysis were made by electron

diffraction and high-resolution electron microscopy (HREM) in JEM-4000FX device at operating voltage from 200 to 400 kV. The TEM instrument was calibrated with a pure gold standard sample. To control the electron diffraction results the powder X-ray diffraction (XRD) also was used. The Raman spectra were obtained in the region of 200 to 2000 cm^{-1} at 514 nm Ar^{+} laser wavelength and 3 mW incident laser power, using micro-Raman Renishaw 2000 microscope that was calibrated by 521 cm^{-1} mode from the silicon standard sample.

3. Results and Discussion

AFM study of as-deposited Co+C_{60} film revealed the nano-granule structure as precursor of expected Co encapsulation. Inner structure of the granules was specified using HRTEM characterization of the film. Figure 1 shows the HRTEM image of 20 nm thick Co+C_{60} film deposited at room temperature on (001) NaCl. This image clearly represents phase separation in the mixture showing individual Co nano-particles (dark contrast) with carbon-based material between those (bright contrast). Observation of the crystal lattice (black arrow) with spacing of about 0.2 nm identifies a crystalline origin of Co nano-particles. The results of XRD and electron diffraction permitted to identify face-centered cubic (fcc) crystal structure of Co nano-particles which is unstable at room temperature. Stable hexagonal close-packed (hcp) phase of cobalt has not been detected being correlated with other reports [4,7,8]. On the other hand, graphitic layers around Co nano-particles, that was typical for referred studies, in presented films is not observed (see Fig.1).

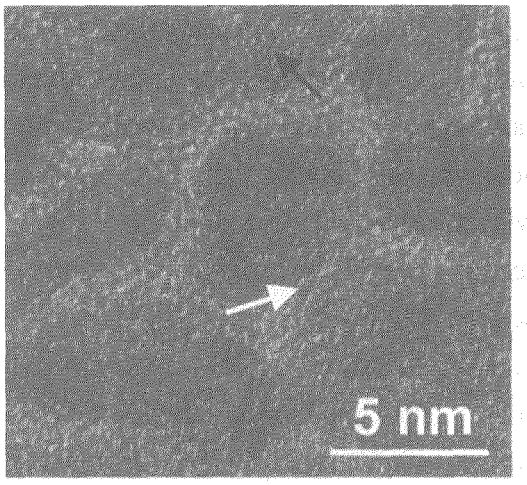

Fig. 1 HRTEM image of Co+C_{60} film deposited at room temperature.

Ripple-type contract within carbon-based material with suitable periodicity suggests an existence of C_{60} molecules as the main units of the substance surrounding the Co nano-particles [9]. As it could be distinguished some crystal lattice (which is different from graphitic one) projects beyond the Co particle (see Fig.1, white arrow), which suggests the formation of crystal layer on the facets of fcc-Co. Using electron diffraction method the crystal layer on the surface of Co-particles has been identified as diamond. Probably, the similarity of lattice constant in fcc-Co and diamond induced typical Moiré pattern usually observed during HRTEM

experiments. Negligible effect in Raman spectrum (small peak at 1328 cm^{-1}) reflects the limited formation of diamond on the facets of fcc-Co crystals, which could occur as the epitaxial nucleation of diamond under sufficient concentration of carbon sp^3 sites and suitable value of local stresses [10,11]. Remarkably, after annealing even at 300°C strong Raman peak arises at 1320 cm^{-1} suggesting the nucleation of diamond on uncovered Co crystals facets. According to Raman spectrum the carbon-based material between Co crystals includes mostly C_{60} molecules distorted by the interaction with cobalt. The interaction destroys some amount of C_{60} molecules resulting in growth of carbon nano-structures by sp^3 and sp^2 sites [11,12]. Intensity of Raman component corresponding to the destroyed C_{60} drastically increases with the deposition temperature. This dependence reflects the important role of thermal activation for efficiency of chemical interaction between Co atoms and C_{60} molecules. Analysis of C_{60} Raman modes shows that depending on the deposition temperature the chemical interaction can form Co-C_{60} complexes with the different structures. Since these complexes build the carbon-based material between Co nano-crystals suitable thermal conditions during Co+C_{60} mixture film preparation promises a set of potential materials with different electronic properties.

References

1. Ch. Kittel, *Phys. Rev.* **70** (1946) 965-971.
2. V. P. Dravid, J. J. Host, M. H. Teng, B. Elliott, J. Hwang, D. L. Johnson, T. O. Mason, J. R. Weertman, *Nature* **374** (1995) 602.
3. T. Hayashi, S. Hirono, M. Tomita, S. Umemura, *Nature* **381** (1996) 772-774.
4. J. Jiao, S. Seraphin, X. Wang, J. C. Withers, *J. Appl. Phys.* **80** (1996) 103-108.
5. J. J. Delaunay, T. Nayashi, M. Tomita, S. Hirono, *J. Appl. Phys.* **82** (1997) 2200-2208.
6. J. Jiao, S. Seraphin, *J. Appl. Phys.* **83**, (1998) 2442-2448.
7. J. M. Bonard, S. Seraphin, J. E. Wegrowe, J. Jiao, A. Chatelain, *Chem. Phys. Lett.* **343** (2001) 251-257.
8. J. J. Host, J. A. Block, K. Parvin, V. P. Dravid, J. L. Alpers, T. Sezen, R. LaDuca, *J. Appl. Phys.* **83** (1998) 793-801.
9. D. Kogura, S. Hameroff, J. Withers, R. Loutfy, M. Sundareshan. *Fullerene C_{60}.* Elsevier, Amsterdam, 1993.
10. V. Lavrentiev, H. Abe, S. Yamamoto, H. Naramoto, K. Narumi, *Molecular crystals and liquid crystals* (in press).
11. V. Lavrentiev, H. Abe, S. Yamamoto, H. Naramoto, and K. Narumi, *Surface and Interface Analysis* (in press).
12. V. Lavrentiev, H. Abe, S. Yamamoto, H. Naramoto, and K. Narumi, *Physica B: Condensed Matter* (in press).

5.12 Structure and optical properties of Ge implanted with carbon ions

P. Wei*, Y. Xu*, S. Nagata**, K. Narumi*, H. Naramoto*
Advanced Science Research Center, JAERI*,
Institute for Materials Research, Tohoku University**

1. Introduction

During the past few years, Ge-C system was attracted a lot of attention due to its potential application in optoelectronic devices. Because Ge and C are immiscible (the equilibrium solubility of C in Ge is limited to $10^8 cm^{-3}$), many efforts had been carried out on the study of pseudomorphic $Ge_{1-y}C_y$ alloy films prepared by non-thermal equilibrium process such as MBE and CVD etc. [1]. Few investigations were carried out on Ge-C system using ion implantation [2], especially with high dose of C implantation.

In this work, the structure and optical properties of as-implanted and post-annealed carbon implanted Ge were characterized by RBS/Channeling, Nuclear Reaction Analysis(NRA) [3], Raman spectrometry and AFM techniques.

2. Experiment

n-type Ge(110) single crystal with one surface mechanically polished was implanted with 125keV $^{12}C^+$ tilted 50° at room temperature at Tohoku University. The implanted dose was $1\times10^{17} C/cm^2$ which was quantified later by NRA. The experiment was performed under a background pressure of 2×10^{-7}torr. The C^+ beam was scanned across the sample to ensure a homogeneous lateral distribution of implants and the beam current density was ~0.2μA/cm^2. After being characterized by different techniques, the sample was annealed in a ceramic tube at 500°C under the flowing 3%H_2+Ar mixing gas for 1 hour.

Ion beam analysis (such as RBS, RBS/Channeling and NRA) was performed using a 3MV single voltage accelerator in JAERI, Takasaki. The target chamber was evacuated down to 2×10^{-7}torr before the analysis was taken. The secondary electron emission was suppressed by applying a –350V voltage on the chamber. The samples were mounted on a computer controlled 3 axes goniometer with the angular resolution of 0.01°. RBS and RBS/Channeling were carried out using 2MeV He^+ beam while NRA was performed using 1.25MeV D^+ beam with the reaction $^{12}C(D, p)^{13}C$.

Raman measurement was performed with the 514nm line of an Ar^+ laser in the backscattering configuration with an instrumental resolution of about $1cm^{-1}$.

AFM observations were made in air at room temperature using a commercial scanning probe microscope JEOL JSPM-4200 operating in the AC mode. The $1\times1\mu m^2$ images of the sample surface were obtained with silicon cantilever.

3. Results

Fig.1 shows the aligned and random spectra of as-implanted and 500°C annealed

samples collected by using 1.25MeV D^+ where RBS and NRA signals can be simultaneously collected in one spectrum. RBS/Channeling spectra with better depth resolution can be further obtained using 2MeV He^+ beam (not shown here). The content of implanted C can be extracted from NRA by integrating the peak area located in the range from channel 885~898 with subtracting the contribution due to the C contamination in virgin Ge. The calculated amount approaches to $1.3\times10^{17}C/cm^2$. After annealing at 500°C, the defects induced by implantation disappeared, which is evidenced by RBS/Channeling spectrum in Fig.1. In the NRA spectra, C atoms have a tendency to diffuse out and accumulate at the surface. The angular scanning around the major crystallographic axes for virgin and annealed Ge demonstrates that no strain exist (figure is not shown for the simplicity).

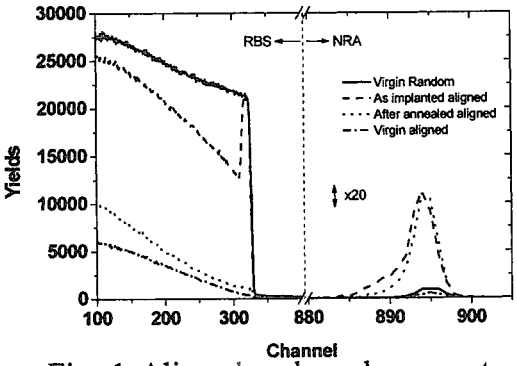

Fig. 1 Aligned and random spectra collected using 1.25MeV D^+

Fig. 2 shows the Raman spectra for both as implanted and 500°C annealed samples. Carbon is in amorphous state for as-implanted sample while it was partly graphitized after annealing at 500°C.

Fig. 3 shows the AFM images of as-implanted and annealed samples as well as the virgin Ge before implantation. After implantation, the surface became amorphous. The implanted sample was recrystallized after annealing at 500°C and C atoms precipitated at the surface (depicted with arrow in Fig. 3(c)).

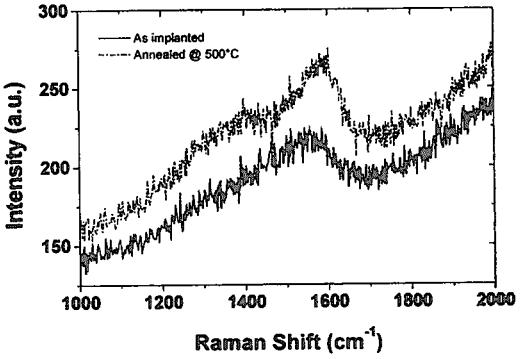

Fig. 2 Raman spectra for both as implanted and annealed samples

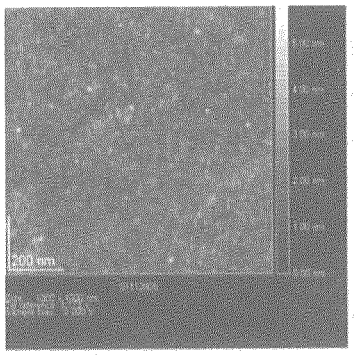

(a) Virgin

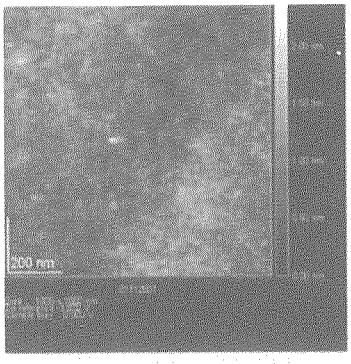

(b) As-implanted

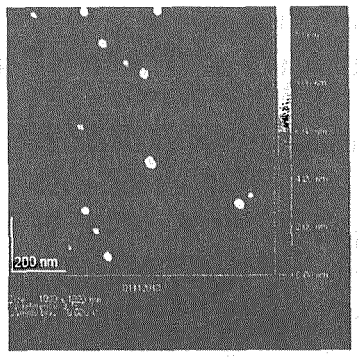

(c) Annealed at 500°C

Fig. 3 AFM

Reference

[1] J. Kolodzey, et al., Appl. Phys. Lett. 67(1995)1865.

[2] L. Hoffmann, et al., Phys. Rev. B 55(1997)11167.

[3] J. R. Tesmer, Michael Nastasi edit, Handbook of Modern Ion Beam Materials Analysis, Materials Research Society, 1995.

5.13 Study of Improvement of Ion Irradiation Pd Using a Slow Positron Beam

H. Abe*, H. Uchida**, Y. Azuma**, A. Uedono***, Z. Q. Chen*** and H. Itoh*

Department of Material Development, JAERI*

Faculty of Engineering, Tokai University**

Institute of Applied Physics, University of Tsukuba***

1. Introduction

Palladium (Pd) is used for the purification of H_2 gas to manufacture pure H_2 and as a catalyst for the dissociation of H_2 molecules. In fact, recent studies on the hydrogen storage properties of rare earth base $LaNi_5$ alloy and AB_5 (A: rare earth element, B: transition element) alloys, which are based on results of in this study. They has made a significant impact on the battery, largely due to their high hydrogen solubility and capacity of hydrogen absorption and desorption at room temperature. Therefore it is indispensable to improve the hydrogen absorptivity in the material. Regarding the hydrogen storage in metals, it was reported that the hydrogen reaction rate depend strongly on the surface state of metals[1]. For surface modification of materials, since low energy ion irradiation, i.e., ion implantation is known to be a quite useful method. These facts give the possibility that the hydrogen absorptivity in Pd is improved by surface modification due to ion irradiation[2]. In order to examine the effects of ion irradiation on the hydrogen absorption process in Pd, we have performed proton (H^+) and helium ion (He^+) irradiation into the materials. Defects introduced in Pd by ion irradiation were investigated using positron annihilation spectroscopy[3]. Hydrogen absorption in ion irradiated Pd was also evaluated. Based on the obtained results, we discuss the correlation between ion irradiation and hydrogen absorption in Pd.

2. Experimental

The samples used in this study were Pd sheets (99.99 % purity) with a size of 15 x 15 x 0.1 mm^3. Prior to irradiation, all Pd samples were annealed at 1173 K in a flowing pure N_2 gas (99.9998 % purity). Ion irradiation was made with H^+ and He^+ in an acceleration energy range from 30 to 350 keV, dose of 1 x 10^{16} /cm^2.

Positron annihilation measurements were performed for the samples before and after irradiation. Doppler-broadening profiles of annihilation γ-rays for the unirradiated and irradiated samples were obtained at room temperature by using monoenegetic positron beams with energies (E) up to 30 keV[4]. The obtained spectrum of annihilation γ-rays was characterized by the S-parameter, which is defined as the

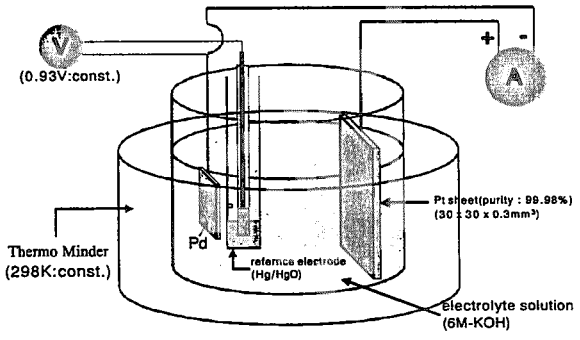

Fig. 1. An electrolytic cell with palladium cathode apparatus

ratio of the counts in an energy range of 511 ± 0.75 keV to the total counts (5 x 10^5 photons). For the analysis of the *S-E* relation, a computer code VEPFIT[5] was used. In the analysis, we assumed a square depth distribution of defects in the irradiated Pd samples.

Hydrogen absorption measurements were also performed for the irradiated and unirradiated samples. An electrolytic cell with palladium cathode apparatus, which is shown in Fig.1, was used to characterize hydrogen storage of the samples[6, 7]. The Pd surface was prepared by electrolysis using a size of 15 x 15 x 0.1 mm^3 of Pd sheet as a cathode, the opposite electrode of Pt sheet as an anode which size of 30 x 30 x 0.3 mm^3, 99.98 % purity. Hg/HgO electrode was used as the reference electrode in an open cell. The electrolyte of 6M-KOH was used for all rate measurements. From the measured current in charging at a constant potential 0.93 V, the H concentration absorbed by the negative electrode was calculated. In all reactions measured, no bubbles were observed during the hydriding.

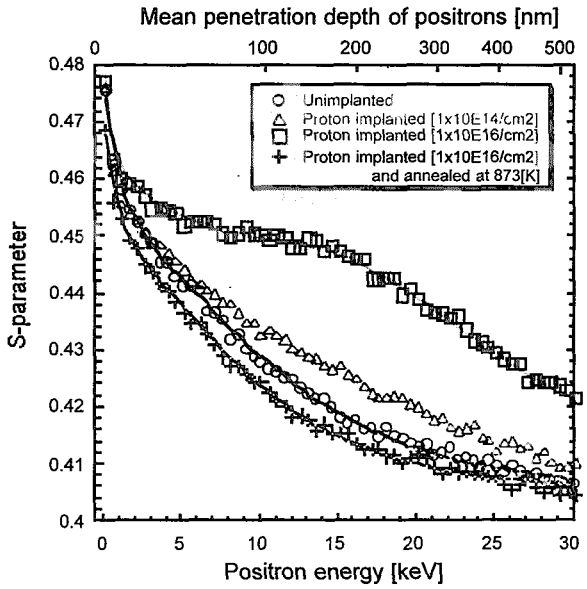

Fig. 2. *S*-parameter as a function of incident positron energy for the unirradiated and irradiated Pd samples. The fluences of protons were 1 x 10^{14} and 1 x 10^{16} /cm^2. Data for the sample irradiated at 1 x 10^{16} /cm^2 and subsequently annealed at 873 K is also plotted.

3. Results and Discussion

Figure 2 shows the *S*-parameter as a function of *E* for the proton irradiated and unirradiated Pd samples. In the unirradiated sample, the *S*-parameter increased with decreasing *E*. This result is attributed to out diffusion of positrons and their annihilation at the surface. As a result of fitting using VEPFIT, the positron diffusion length in the unirradiated sample was obtained to be 162 ± 1 nm.

In the proton irradiated samples, large values of the *S*-parameter were obtained in comparison with those of the unirradiated sample. The *S* value increased with irradiation fluence of protons. These results indicate that vacancy type defects are produced by irradiation and that their size and concentration increase with proton fluence. In the sample irradiated at 1 x 10^{16}/cm^2, it was derived from the fitting that vacancy type defects were formed to a depth of 400 ± 10 nm, which is in good agreement with the calculated range of defect production using TRIM[8]. The characteristic *S*-parameter and positron diffusion length in a defective region were also estimated to be 0.4509 ± 0.0001 and 37 ± 2 nm, respectively. After annealing of the sample at 873 K, the *S* values decreased to a level similar to those of the unirradiated sample. This result suggests that almost all vacancy type defects are removed by the annealing.

Figure 3 shows the results of hydrogen reaction rate in the unirraidated, proton irradiated and helium ion irradiated samples. Typical electrochemical hydriding curves,

unirradiation, 30keV-H^+, 100keV-H^+, 100keV-He^+ and 350keV-He^+ measured at 298 K as the increase of the H concentration [H]/[Pd] as a function of time for the Pd with and without KOH pretreatments for the initial stage at reaction time from 0 to 300

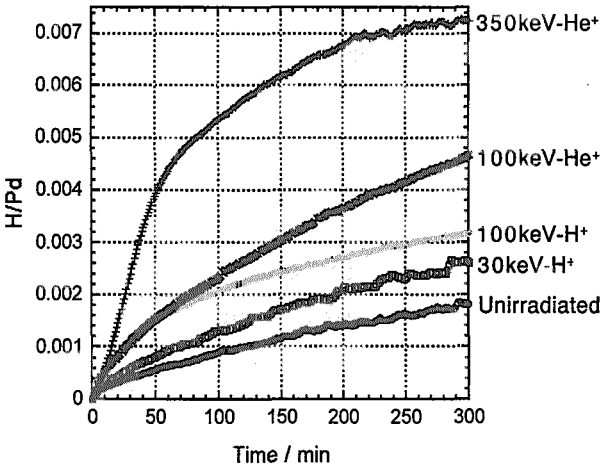

Fig.3. Change in the ratio of absorbed hydrogen atoms to Pd atoms ([H]/[Pd]) for the unirradiated and irradiated samples.

minutes. The hydrogen reaction rate can be determined from a temporal change in the [H]/[Pd] value. The value of unirradiated, 30keV-H^+, 100keV-H^+, 100keV-He^+ and 350keV-He^+ samples were estimated to be [H]/[Pd] = 0.0018, 0.0026, 0.0032, 0.0046 and 0.0072 respectively. The hydrogen reaction rate of the ion irraidated sample was higher (max. 4 times) than that of the unirradiated one.

As a result, ion irradiated Pd sample was found to induce a higher absorption rate than that of the unirradiated one. The initial hydrogen absorption rate was also found to increase with increasing irradiation energy. These results suggest that defects introduced in Pd by ion irradiation facilitate the rate of nucleation and growth of hydride.

References

1) H. Uchida, Int. J. Hydrogen Energy 24 (1999) p.861.
2) H. Abe, A. Uedono, H. Uchida, A. Komatsu, S. Okada and H. Itoh, Material Science Forum 363-365 (2001), p.156.
3) P. Asoka-Kumar and K. G. Lynn, Applied Physics Letters 57 (1990) p.1634.
4) A. Uedono, S. Tanigawa, T. Ohshima, H. Itoh, M. Yoshikawa, I. Nashiyama, T. Frank, G. Pensl, R. Suzuki, T. Ohdaira and T. Mikado, Journal of Applied Physics 87 (2000) p. 4119.
5) A. van Veen, H. Schut, J. de Vries, R. A. Hakvoort and M. R. Ijpma: AIP Conference Proceedings 218 (1990) p.171.
6) H. Uchida, M. Sato, W. Cui, T. Tabata, M. Kumagai, H. Takano and T. Kondo, Journal of Alloys Compounds 293-295 (1999) p. 30.
7) H. Uchida, K. Yamashita, T. Tabata, H. H. Uchida, M. Iwase and Y. Katoh, Journal of Alloys Compounds 293-295 (1999) p.751.
8) J. F. Ziegler, *Handbook of Ion Implantation Technology* (Elsevier, Amsterdam 1992), p.1.